JOURNAL OF GEOPHYSICAL RESEARCH, VOL. 114, B03202, doi:10.1029/2008JB005906, 2009

Lithospheric mantle duplex beneath the central Mojave Desert revealed by xenoliths from Dish Hill, California

Peter Luffi,[1,2] Jason B. Saleeby,[1] Cin-Ty A. Lee,[3] and Mihai N. Ducea[4]

Received 30 June 2008; revised 30 November 2008; accepted 12 December 2008; published 5 March 2009.

[1] Low-angle subduction of oceanic lithosphere may be an important process in modifying continental lithosphere. A classic example is the underthrusting of the Farallon plate beneath North America during the Laramide orogeny. To assess the relevance of this process to the evolution and composition of continental lithosphere, the mantle stratigraphy beneath the Mojave Desert was constrained using ultramafic xenoliths hosted in Plio-Pleistocene cinder cones. Whole-rock chemistry, clinopyroxene trace element and Nd isotope data, in combination with geothermometry and surface heat flow, indicate kilometer-scale compositional layering. The shallow parts are depleted in radiogenic Nd ($\varepsilon_{Nd} = -13$ to -6.4) and are interpreted to be ancient continental mantle that escaped tectonic erosion by low-angle subduction. The deeper samples are enriched in radiogenic Nd ($\varepsilon_{Nd} = +5.7$ to $+16.1$) and reveal two superposed mantle slices of recent origin. Within each slice, compositions range from fertile lherzolites at the top to harzburgites at the bottom: the latter formed by 25–28% low-pressure melt depletion and the former formed by refertilization of harzburgites by mid-ocean-ridge-basalt-like liquids. The superposition and internal compositional zonation of the slices preclude recent fertilization by Cenozoic extension-related magmas. The above observations imply that the lower Mojavian lithosphere represents tectonically subcreted and imbricated lithosphere having an oceanic protolith. If so, the lherzolitic domains may be related to melting and refertilization beneath mid-ocean ridges. The present Mojavian lithosphere is thus a composite of a shallow section of the original North American lithosphere underlain by Farallon oceanic lithosphere accreted during low-angle subduction.

Citation: Luffi, P., J. B. Saleeby, C.-T. A. Lee, and M. N. Ducea (2009), Lithospheric mantle duplex beneath the central Mojave Desert revealed by xenoliths from Dish Hill, California, *J. Geophys. Res.*, *114*, B03202, doi:10.1029/2008JB005906.

1. Introduction

[2] Mantle xenolith studies have great potential in refining our understanding of one of the most important questions in the earth sciences: the origin and evolution of continental lithospheric mantle. In particular, correlating mantle xenolith petrogenetic studies with petrologic and tectonic studies of the overlying crust have great potential in constraining whole lithosphere-scale processes. For example, mantle xenoliths that were entrained in Neogene volcanic necks and flows from the central Sierra Nevada batholith record the preservation of the mantle wedge source regime for the overlying batholith for ~70 Ma following the cessation of subduction driven magmatism in the region [*Ducea and Saleeby*, 1996, 1998c; *Ducea*, 2001; *Saleeby et al.*, 2003; *Ducea et al.*, 2005]. These and parallel mantle xenolith studies [*Ducea and Saleeby*, 1998b, 1998a], along with seismic studies [*Jones and Phinney*, 1998; *Ruppert et al.*, 1998; *Zandt et al.*, 2004] further reveal the geologically rapid removal of this mantle wedge remnant and its replacement by asthenospheric mantle in Plio-Pleistocene time. These deep-seated and seemingly remote events in turn may be clearly related to rapidly evolving surficial structures and landforms [*Saleeby and Foster*, 2004; *Stock et al.*, 2004; *Clark et al.*, 2005].

[3] The evolution of the mantle lithosphere beneath the Mojave Desert region in southeastern California, USA, stands as an important regional and global problem in the context of deciphering the potential complexities that upper mantle regimes may experience in the transition zones between stable cratonic interiors and their more mobile margins. The Mojave Desert region constitutes a critical segment in the Cretaceous North American Cordilleran batholithic belt, but it is unique in terms of its paleogeographic position along the belt. The unique paleogeographic setting arises from the fact that the Mesozoic active margin, which culminated with Cretaceous batholithic magmatism, was established along a major transform system that cut obliquely into cratonic North American lithosphere, thereby

[1]Division of Geological and Planetary Sciences, California Institute of Technology, Pasadena, California, USA.
[2]Now at Department of Earth Science, Rice University, Houston, Texas, USA.
[3]Department of Earth Science, Rice University, Houston, Texas, USA.
[4]Department of Geosciences, University of Arizona, Tucson, Arizona, USA.

0148-0227/09/2008JB005906$09.00

localizing the ensuing batholithic belt immediately adjacent to cratonic lithosphere in the region of the Mojave Desert [*Davis et al.*, 1978; *Walker*, 1988; *Saleeby*, 1992; *Dickinson and Lawton*, 2001]. Elsewhere along the North American Cordillera, the batholithic belt formed entirely within accretionary complexes (encompassing passive margin, marginal basin and fringing island arc belts) rather than intruding cratonic basement [*Burchfiel et al.*, 1992; *Gabrielse et al.*, 1992]. The structurally disrupted state presently seen in the Mojave segment of the batholithic belt arises from a pronounced phase of shallow flat subduction that developed in the region from the segmentation of the Farallon plate as it subducted beneath the region in the Late Cretaceous [*Barth and Schneiderman*, 1996; *Saleeby*, 2003]. This shallow slab segment regime has been interpreted as the plate edge expression of the Laramide orogeny, a latest Cretaceous-Paleogene deformation event known to have widely affected the southwest Cordilleran craton margin. The paleogeographic setting of the Mojave segment of the batholithic belt strongly suggests that cratonic mantle lithosphere was immediately proximal to the subarc mantle wedge environment during Cretaceous to Cenozoic subduction. The shallow flat slab segment subduction cycle has been hypothesized to have removed some of the North American lithospheric mantle by tectonic erosion [*Bird*, 1988]. However, seismic studies indicate that under this same region, the present-day lithospheric mantle is >60 km thick [*Yang and Forsyth*, 2006; *Li et al.*, 2007], suggesting that the North American lithospheric mantle beneath the Mojave might have been rethickened or reconstructed.

[4] In this study, we use mantle xenoliths from Plio-Pleistocene cinder cones in the Mojave Desert to constrain the stratigraphy of the Mojavian lithospheric mantle. We show that the present-day Mojavian lithospheric mantle is stratified in major and trace element compositions as well as isotopically. We discuss the possibility that the Mojavian lithosphere represents the juxtaposition of two different lithosphere types, a shallower North American lithosphere underlain by Farallon oceanic lithosphere attached during low-angle subduction. We discuss our geochemical and petrological observations in the context of the tectonic evolution of the region, and address broader implications of our results.

2. Geologic Setting

[5] The Mojave Desert region constitutes a ~400 km long segment along the Cretaceous North American Cordilleran batholithic belt. Its westward extension, across the restored San Andreas Fault, consists of batholithic basement rocks of the Salinia terrane [*Huffman*, 1972; *Saleeby*, 2003; *Barbeau et al.*, 2005]. Collectively, the Salinian, Mojave, and the immediately adjacent southern Colorado River Desert basement complexes are termed the southern California batholith (SCB). In contrast to the Sierra Nevada batholith (SNB) to the north and the Peninsular Ranges batholith (PRB) to the south, much of the SCB is rootless, lying tectonically above underplated subduction accretion assemblages that were transported inland by flat shallow subduction from the Franciscan trench [*Jacobson et al.*, 1988; *Hall*, 1991; *Grove et al.*, 2003; *Kidder and Ducea*, 2006]. The underplated rocks are termed the Rand and Portal Ridge schists in the Mojave region, the schist of Sierra de Salinas in Salinia, and the Orocopia and Pelona schists in the southern Colorado River Desert and once contiguous Transverse Ranges. The schists are widely known for their principal exposure in a series of structural windows through deep crustal level batholithic upper plate autochthons (Figure 1).

[6] The tectonic position of the underplated schist is critical in the analysis of upper mantle evolution for the region. Below we focus primarily on the Rand, Portal Ridge and Orocopia schists, those schist bodies that have not been translated with their respective upper batholithic plates along the San Andreas Fault. The Rand schist occurs as a series of windows dispersed along the northwest Mojave and southernmost Sierra Nevada region. The bounding structure is the Rand fault, a structurally modified subduction megathrust flat that the schist protolith assemblage was originally subducted along. Metamorphic equilibration pressures in the Rand schist are ~9 kb [*Pickett and Saleeby*, 1993; *Jacobson*, 1995]. Equilibration pressures in proximal upper plate rocks range from 7 to 11 kb. The Portal Ridge schist lies along the San Andreas Fault in the western Mojave. It is juxtaposed against its upper plate by a late-stage high-angle fault. The Rand and Portal Ridge schists can be linked by structure contours (Figure 1) constructed from surface relations and a series of seismic studies [*Cheadle et al.*, 1986; *Li et al.*, 1992; *Malin et al.*, 1995; *Yan et al.*, 2005]. The contour pattern indicates that the Rand fault and underlying schist lie beneath the entire western Mojave in a broad synform structure. Resolution of this structural system is prohibited east of ~117.5°W by a lack of subsurface data, but by simple structural projection it is assumed that the schist deepens eastward into the lower crust over some tens of kilometers, suggesting that it constitutes the lower crust of the central Mojave as far east as 116°W.

[7] The presence of the schist in the midcrust to lower crust of the western and central Mojave is further suggested by geophysical and geochemical data. *Sass et al.* [1994] identified a ~N-S trending heat flow boundary at ~116°W, wherein values of <80 mW/m^2 occur to the west and values of >100 mW/m^2 occur to the east. Interestingly, *Miller et al.* [2000] identified an isotopic geochemical boundary at ~116° W in Miocene mafic volcanic rocks: those occurring to the east contain continental lithosphere components, but those to the west lack such components. *Miller et al.* [1996] further showed that the latest-stage batholithic plutons of the western Mojave contain a source component consistent with underplated schist materials. Collectively, these studies corroborate the structure contour pattern of Figure 1: a major compositional boundary lies within the midcrust to deep crust of the central Mojave, demarcating a western domain containing abundant schist as basement rocks and an eastern domain lacking significant schist and containing significant remnants of old continental lithosphere.

[8] The lack of continental lithosphere components in Miocene volcanic rocks of the western Mojave reported by *Miller et al.* [2000] contrasts with what is known about source components for much of the SCB. Continental lithosphere components, which could represent ancient upper mantle or crustal reservoirs, are widespread in the Cretaceous granitoids and occur even as far west as the Salinia exposures of the SCB [*Kistler and Peterman*, 1978;

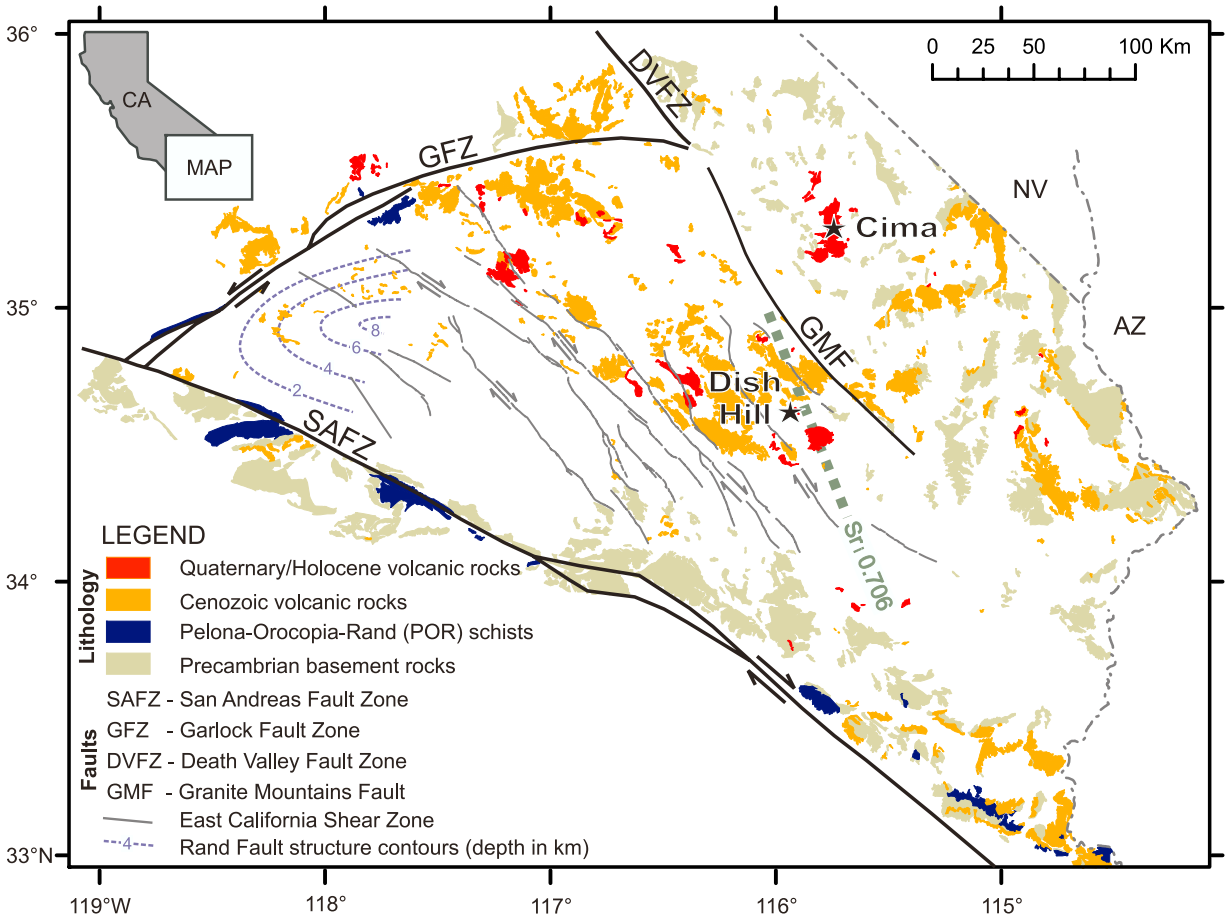

Figure 1. Map showing the locations of mantle xenoliths studied in this paper (Dish Hill and the Cima volcanic field) in the context of relevant geological features of the Mojave Desert. Lithology and faults are based on the work of *Ludington et al.* [2005], *Dokka* [1983], and *Malin et al.* [1995]. Rand Fault structure contours are based on the work of *Cheadle et al.* [1986], *Li et al.* [1992], *Malin et al.* [1995], and *Yan et al.* [2005]. Young (<5 Ma) mafic volcanic rocks throughout the Mojave Desert, including the basalts from Dish Hill and Cima, have isotopic compositions indicative of an asthenospheric source [*Livaccari and Perry*, 1993]. Isotopic compositions of older Cenozoic mafic volcanic rocks suggest significant differences in their source [*Miller et al.*, 2000]: In the eastern part, where Precambrian basement rocks are abundant and rocks of oceanic origin are absent, Cenozoic basalts have ancient, isotopically enriched mantle source. In the western part where Precambrian rocks are rare and formations of oceanic origin occur, Cenozoic mafic rocks derived from younger, depleted mantle source. The Sr_i 0.706 line represents the boundary between these domains, according to *Miller et al.* [2000].

Kistler and Champion, 2001]. The distribution of Precambrian basement rocks in the Mojave region is also shown in Figure 1. These appear to be restricted to the eastern margin of the batholithic exposures, although the paleogeographic affinity of a number of metasedimentary pendants of the western Mojave and Salinia to the Cordilleran passive margin sequence [*Martin and Walker*, 1995; *Barbeau et al.*, 2005] suggest that at least thinned continental mantle lithosphere once extended beneath these regions. These relations further suggest profound changes in mantle lithosphere structure in the time interval between the cessation of batholithic magmatism and the onset of Neogene volcanism. We interpret this change to have resulted from the flat slab-related tectonic erosion of the SCB mantle wedge.

[9] The above discussed regional geologic relations and the constraints on gross crustal structure and depth of the lithosphere posed by the geophysical and geochemical data suggest that the middle to lower crust and mantle lithosphere in the western Mojave region may have been reconstructed between ~70 Ma and ~20 Ma. There are a number of well-known mantle xenolith locations within the central to eastern Mojave that are strategically situated for studying how the deep lithosphere was modified [*Wilshire et al.*, 1988]. One of the most notable locations is Dish Hill. Linearly interpolating between the Rand Mountain schist window in the northernmost Mojave to the string of Orocopia schist windows in the southeastern Mojave–southern Colorado River Desert region (Figure 1) suggests that Dish Hill lies above a mantle domain that underwent extensive tectonic erosion and subsequent underplating. In contrast, the well-known Cima volcanic field lies to the NNE above a region expected to be underlain by substantial

Table 1a. Petrography and Representative Mineral Compositions of Xenoliths From Dish Hill

	Petrography		Olivine										
Sample	Rock[a]	Texture[b]	Analysis	SiO_2	TiO_2	Al_2O_3	Cr_2O_3	FeO	MnO	MgO	NiO	CaO	Total	Mg #[c]
DHE01	hzb	a–g	2/3	41.42	0.00	0.00	0.04	8.34	0.14	50.47	0.37	0.07	100.85	0.915
DHE03	lhz	a–g	2/59	40.27	0.00	0.03	0.02	11.06	0.14	47.41	0.37	0.10	99.40	0.884
DHE04	lhz	pc	48/3	40.92	0.00	0.01	0.05	9.64	0.13	49.53	0.39	0.05	100.72	0.902
DHE10	lhz	a–g	17/113	40.74	0.02	0.04	0.02	10.00	0.13	48.84	0.35	0.11	100.25	0.897
DHE11	hzb	a–g	52/4	41.10	0.02	0.04	0.03	9.02	0.08	49.87	0.38	0.08	100.62	0.908
DHE12	hzb	a–g	25/5	41.27	0.00	0.02	0.06	8.05	0.13	50.77	0.41	0.07	100.78	0.918
DHE13	hzb	a–g/pc	38/3	41.39	0.01	0.03	0.03	9.34	0.17	49.01	0.37	0.09	100.44	0.903
DHN01	hzb	a–g	99/408	40.40	0.00	0.01	0.02	9.14	0.12	49.19	0.39	0.10	99.37	0.906
DHN05	hzb	a–g/pc	27/202	41.38	0.00	0.02	0.03	8.95	0.15	49.65	0.44	0.11	100.73	0.908
DHN07	lhz (a)	pc	27/37	40.35	0.04	0.00	0.01	9.50	0.12	48.69	0.43	0.06	99.20	0.901
DHN08	lhz	pc + pm	2/57	40.35	0.01	0.04	0.06	9.92	0.18	48.73	0.38	0.07	99.74	0.897
DHN09	lhz	a–g	56/96	40.53	0.02	0.01	0.02	9.72	0.13	48.71	0.38	0.06	99.58	0.899
DHN11	wbt (a)	ig/e–m	8/147	39.92	0.00	0.00	0.00	18.36	0.23	42.26	0.20	0.06	101.03	0.804
DHN12	hzb	a–g	71/227	41.06	0.00	0.00	0.01	8.45	0.11	50.00	0.38	0.05	100.06	0.913
DHN16	lhz (a)	pc	49/74	40.10	0.02	0.02	0.02	9.23	0.15	48.45	0.38	0.06	98.43	0.903
DHS02	lhz	a–g/pc	40/295	40.94	0.00	0.03	0.02	9.09	0.14	49.49	0.37	0.10	100.18	0.907
DHS03	lhz	pc	40/16	40.08	0.00	0.03	0.03	9.02	0.14	49.37	0.33	0.07	99.07	0.907
DHS04	lhz	a–g/pc	62/131	39.62	0.00	0.02	0.01	10.18	0.14	49.03	0.37	0.08	99.45	0.896
DHS05	lhz	a–g	22/12	40.92	0.00	0.02	0.00	9.56	0.16	49.37	0.38	0.07	100.48	0.902
DHS06	lhz	pc[d]	4/3	40.79	0.00	0.01	0.05	9.14	0.16	49.46	0.32	0.06	99.99	0.906
DHS07	lhz	a–g	53A/176	40.32	0.02	0.02	0.00	9.70	0.12	48.83	0.36	0.07	99.44	0.900
DHS08	lhz	a–g	45/35	40.11	0.00	0.00	0.01	9.48	0.12	48.99	0.38	0.08	99.17	0.902
DHS11	lhz	a–g[e]	90/358	40.71	0.03	0.02	0.01	9.31	0.20	49.23	0.36	0.07	99.94	0.904
DHS13	lhz	a–g	80/271	39.34	0.02	0.02	0.00	14.98	0.27	43.79	0.29	0.09	98.80	0.839
DHS14	lhz	pc[e]	93/384	40.65	0.00	0.02	0.00	9.83	0.14	48.98	0.35	0.07	100.04	0.899
DHS15	lhz	a–g	76/256	40.49	0.00	0.02	0.04	9.37	0.14	48.65	0.40	0.07	99.18	0.902
DHS16	lhz	p–c[e]	108/452	40.67	0.00	0.03	0.01	9.49	0.12	49.14	0.37	0.07	99.90	0.902
DHS17	lhz	a–g/pc	104/52	40.14	0.00	0.02	0.00	9.51	0.14	49.39	0.40	0.06	99.66	0.902
DHS18	lhz (a)	pc[e]	76/164	40.21	0.01	0.01	0.01	9.58	0.12	48.98	0.41	0.07	99.40	0.901
DHS20	lhz	pc	37/279	40.63	0.00	0.02	0.00	9.89	0.10	48.90	0.36	0.07	99.97	0.898
DHS21	lhz (a)	a–g/pc	70/90	40.53	0.00	0.00	0.02	9.04	0.14	49.38	0.39	0.07	99.57	0.907
DHS25	lhz	a–g/pc	33/231	40.92	0.00	0.01	0.00	10.08	0.15	48.85	0.39	0.08	100.48	0.896
DHX02hzb	hzb	e–m/ig	15/3	41.06	0.00	0.01	0.04	8.10	0.15	50.09	0.40	0.04	99.89	0.917
DHX02wbt	wbt (a)	e–m	22/5	40.63	0.01	0.00	0.00	8.38	0.14	50.46	0.43	0.06	100.11	0.915
DHX03	lhz (a)	pc[e]	36/137	40.56	0.00	0.00	0.00	9.94	0.17	48.61	0.37	0.06	99.71	0.897

[a]Rock abbreviations are hzb, harzburgite; lhz, lherzolite; wbt, websterite; (a), amphibole present.
[b]Texture abbreviations are a–g, allotriomorphic granular; e–m, equigranular mosaic; f, foliated; ig, igneous; pc, porphyroclastic; pm, pyrometamorphic.
[c]Using $Fe^{2+} = Fe_{total}$.
[d]Outstanding foliation.
[e]Some foliation.

remnants of ancient mantle lithosphere of the North American autochthon. The focus of this study is Dish Hill. We present a large set of new xenolith data and discuss the data in the context of previous Dish Hill xenolith studies as well as xenolith studies from Cima. In the following we first briefly review the most relevant results of the research that has been done to date on these locations, and then we present and integrate our new data into the regional relations discussed above.

[10] Petrographic and geochemical data published on xenoliths from Dish Hill and Cima suggest notable heterogeneities in the lithospheric mantle underlying the Mojave Desert. The xenolith population in the ~2.1 Ma Dish Hill basanites [*Wilshire and Trask*, 1971] are dominated by spinel peridotites and relatively rare pyroxenites and hornblendites [*Wilshire et al.*, 1988]. The Pliocene and late Pleistocene hawaiites and alkali basalts from Cima [*Turrin et al.*, 1984] contain a wealth of gabbro and pyroxenite xenoliths as well as abundant spinel peridotites [*Wilshire et al.*, 1991]. Strongly metasomatized mantle samples, such as plagioclase infiltrated peridotites, are common at Cima [*Wilshire et al.*, 1991], but rare at Dish Hill [*Wilshire and Trask*, 1971]. Even more striking are the isotopic contrasts between Dish Hill and Cima peridotites: variably metasomatized peridotite xenoliths from Dish Hill show highly radiogenic Nd and nonradiogenic Sr isotopic systematics similar to mid-ocean ridge basalt (MORB) source [*Menzies et al.*, 1985; *Nielson et al.*, 1993], while peridotites with no sign of modal metasomatism from Cima display nonradiogenic Nd and radiogenic Sr and Pb systematics [*Mukasa and Wilshire*, 1997]. Peridotites from Cima also yield Re-Os model ages of 1.8–3.4 Ga [*Lee et al.*, 2001], confirming the Archean to early Proterozoic crust formation predicted from Sm-Nd model ages of the overlying crust [*Bennett and DePaolo*, 1987; *Wooden and Miller*, 1990; *Rämö and Calzia*, 1998]. However, no reliable model ages for xenoliths from Dish Hill are available to date, and direct information about the origin of the above outlined regional-scale compositional heterogeneity of the sub-Mojavian lithospheric mantle is absent.

3. Methods

[11] Major element compositions of minerals were analyzed in polished thin sections of 250 μm thickness. We used three electron-probe microanalyzers: a five-spectrometer JEOL JXA-8200 and a three-spectrometer JEOL 733 at 15 kV and 25 nA at California Institute of Technology, and a

four-spectrometer Cameca SX50 (15 kV and 20 nA) at the University of Arizona; the instruments were calibrated with natural and synthetic standards; matrix corrections were made using the CITZAF [*Armstrong*, 1988] and PaP [*Pouchou and Pichoir*, 1984] algorithms. Representative mineral compositions are tabulated in Tables 1a–1d.

[12] Trace element concentrations in clinopyroxene were analyzed by laser ablation inductively coupled plasma mass spectrometry (LA-ICP-MS) on the thin sections used for electron probing. A New Wave 213 nm laser ablation system coupled to a ThermoFinnigan Element 2 ICP-MS was employed at Rice University. Laser was set to 55 μm spot size, energy density of 15 J/cm^2, and pulse of 10 Hz. Analyses were carried out in low-mass-resolution mode (m/Δm = 300), and typically consisted of 15–20 measurements on gas background and 40–50 measurements during ablation of the sample. Background corrected signals were integrated and normalized to Ca as internal standard (previously analyzed by electron probe). USGS glass standards BHVO2g, BCR2g, and NIST 612 [*Gao et al.*, 2002] were used as external standards for all elements. No significant variations of trace element concentrations in clinopyroxenes have been observed at grain and sample scales; analyses reported in Table 2a are averages of 3–6 individual measurements on a minimum of three grains. The external reproducibility of LA-ICP-MS measurements has been assessed using an in-house standard (San Carlos clinopyroxene SC99–2 cpx) of which trace element concentrations are close to those in the unknown clinopyroxenes (mean values and standard deviations are shown in Table 2b).

[13] Clinopyroxenes from selected samples were analyzed for neodymium isotopes at the University of Arizona and California Institute of Technology. 150–300 μm grains free of visible inclusions and alteration were handpicked under a binocular microscope from previously crushed samples, and then mildly acid-leached in warm 1 M HCl for 30 min. The samples were spiked with mixed ^{147}Sm-^{150}Nd tracers previously described by *Wasserburg et al.* [1981]. Dissolution of the spiked samples for isotopic analyses was performed in screw-cap Teflon beakers using HF-HNO_3 (on hot plates) and HF-$HClO_3$ mixtures (in open beakers at room temperature). Separation of the bulk of the REE was achieved via HCl elution in cation columns. Separation of Sm and Nd was carried out using an LNSpec® resin [*Ducea et al.*, 2003]. The second stage column step was performed twice in order to reduce the chance of Pr interference. The highest procedural blanks measured during the course of this study were 5 pg Sm and 18 pg Nd. Sm and Nd were loaded in HCl onto single Re filaments. Mass spectrometric analyses for Sm were carried out using a static routine on a 54 VG Sector multicollector instrument. Neodymium was measured as an oxide [*Ducea et al.*, 2003] on a 354 VG Sector instrument fitted with a purified oxygen tube and a bleed valve delivering oxygen into the source. Pr and Ce interference was monitored, and no interference from these elements was observed. The runs consisted of 105 isotopic ratios for Nd and 60 ratios for Sm. The mean results of five analyses of the standard nSmß performed during the course of this study are ^{148}Sm/^{147}Sm = 0.74880 ± 21 and ^{148}Sm/^{152}Sm = 0.42110 ± 6. Nine measurements of the La Jolla Nd standard measured as oxide were performed during the course of this study which coincided with the installation of the bleed valve attachment, and yielded results within the accepted range of La Jolla ^{143}Nd/^{144}Nd (mean ^{143}Nd/^{144}Nd = 0.511849 ± 23). The Nd isotopic ratios were normalized to ^{146}Nd/^{144}Nd = 0.7219. Estimated analytical ±2σ uncertainties are ^{147}Sm/^{144}Nd = 0.8% and ^{143}Nd/^{144}Nd = 0.001%. External reproducibility, based on the range of multiple runs of standard La Jolla Nd, is estimated to be ±0.00001. The grand means of isotopic ratios were corrected by an off-line manipulation program, which adjusts for the spike contributions to both the fractionation correction and each ratio, and performs isotope dilution calculations. Results are presented in Table 3.

[14] Whole-rock compositions of the largest and freshest xenoliths were measured by X-Ray fluorescence (XRF) on a ThermoARL Advant'XP+ spectrometer at Washington State University following the methods of *Johnson et al.* [1999]; spectral overlap of Mg and Na has been corrected. Slabs cut from the central portions of the samples were used in order to avoid contamination. The modal mineralogy of these xenoliths was calculated by a least squares method using whole-rock and constituent mineral compositions; resulting sums of the squared residuals are less than 0.1 for most of the samples, and none exceeds 0.3, which indicates negligible intergranular major element contamination. Whole-rock major element compositions of a series of xenoliths not suited for XRF analyses were reconstructed from mineral compositions and modes obtained by point counting (typically 1500–2000 counts per thin section); mineral modes were converted from volume to weight percents using their densities representative for an average spinel facies peridotite. Results are presented in Tables 4a–4d.

[15] Whole-rock rare earth element (REE) contents were estimated using their concentrations in clinopyroxenes and mineral modes, and temperature-dependent partition coefficients for these elements between clinopyroxene and orthopyroxene [*Witt-Eickschen and O'Neill*, 2005] (Table 5). For simplicity we ignored olivine in our calculations because, in the temperature range of interest, REEs are about 2–3 orders of magnitude less compatible than in clinopyroxene [*Witt-Eickschen and O'Neill*, 2005]. Whereas equilibrium partitioning of heavy rare earth elements (HREEs) between pyroxenes can be safely assumed [e.g., *Agranier and Lee*, 2007], such an assumption would be hazardous in the case of middle and light rare earth elements (MREEs and LREEs). Thus, only whole-rock HREE concentrations recalculated by this method are realistic; these will be further used in discussion.

4. Results

4.1. Xenolith Petrography

[16] We collected over 60 xenoliths from the Dish Hill basanitic cinder cone. Most of these are 5–10 cm in diameter and few exceed 15–20 cm. Detailed petrographic observations were carried out on 40 representative samples. The suite is dominated by type I [*Frey and Prinz*, 1978] spinel lherzolites (~70%), spinel harzburgites (~25%), and spinel websterites (~5%). With the exception of harzburgite xenolith DHX02hzb, which is crosscut by a ~2 cm thick amphibole-bearing spinel websterite vein (DHX02wbt), all type I samples are petrographically homogeneous. Amphibole-spinel websterite xenolith DHN11 is also a vein,

Table 1b. Petrography and Representative Mineral Compositions of Xenoliths From Dish Hill

			Orthopyroxene												
Sample	Analysis	Location	SiO_2	TiO_2	Al_2O_3	Cr_2O_3	FeO	MnO	MgO	NiO	CaO	Na_2O	Total	Mg #[a]	Cr #
DHE01	3/3	core	57.04	0.04	2.44	0.63	5.53	0.15	34.47	0.09	0.89	0.08	101.36	0.917	0.148
DHE01	5/1	rim	57.20	0.06	2.40	0.59	5.52	0.13	34.25	0.10	0.86	0.08	101.19	0.917	0.142
DHE03	1/67	core	54.18	0.08	5.06	0.53	6.56	0.13	31.54	–	1.07	0.13	99.28	0.895	0.066
DHE03	1/71	rim	55.12	0.11	5.08	0.51	6.60	0.13	31.47	–	1.04	0.13	100.19	0.895	0.063
DHE04	44/7	core	54.89	0.16	4.92	0.41	6.30	0.14	33.00	0.09	0.78	0.17	100.86	0.903	0.053
DHE04	44/11	rim	54.75	0.14	4.92	0.39	6.34	0.19	32.82	0.06	0.84	0.18	100.63	0.902	0.050
DHE10	19/124	core	54.79	0.13	5.06	0.43	6.51	0.16	32.20	0.10	1.08	0.12	100.58	0.898	0.054
DHE10	21/133	rim	54.75	0.13	5.19	0.49	6.50	0.14	32.19	0.10	1.08	0.12	100.69	0.898	0.060
DHE11	51/5	core	55.04	0.05	4.06	0.59	5.74	0.10	32.90	0.10	1.08	0.11	99.77	0.911	0.089
DHE11	53/5	rim	55.07	0.14	4.09	0.69	5.90	0.12	32.91	0.17	1.17	0.17	100.43	0.909	0.102
DHE12	31/4	core	57.22	0.02	1.97	0.48	5.05	0.12	34.68	0.04	1.00	0.21	100.79	0.924	0.140
DHE12	29/1	rim	57.16	0.02	2.00	0.56	4.99	0.11	34.47	0.10	0.98	0.10	100.49	0.925	0.158
DHE13	37/5	core	55.12	0.09	4.57	0.69	6.07	0.13	32.28	0.11	1.10	0.20	100.36	0.905	0.092
DHE13	40/6	rim	55.22	0.09	4.43	0.61	6.58	0.18	32.15	0.08	1.11	0.27	100.72	0.897	0.085
DHN01	98/403	core	54.15	0.10	4.80	0.60	5.95	0.11	32.56	0.09	1.09	0.10	99.55	0.907	0.077
DHN01	98/402	rim	54.09	0.10	4.67	0.55	5.85	0.14	32.30	0.07	1.07	0.11	98.95	0.908	0.073
DHN05	23/182	core	55.95	0.04	3.67	0.71	5.90	0.14	33.10	0.13	1.20	0.07	100.91	0.909	0.115
DHN05	23/180	rim	55.90	0.04	3.71	0.71	5.75	0.13	33.00	0.12	1.21	0.06	100.63	0.911	0.114
DHN07	22/37	core	53.47	0.14	4.98	0.36	6.28	0.17	32.33	0.15	0.83	0.17	98.88	0.902	0.046
DHN07	26/64	rim	54.34	0.14	4.81	0.35	6.20	0.14	32.58	0.09	0.78	0.11	99.54	0.904	0.047
DHN08	3/20	core	54.17	0.17	5.48	0.33	6.72	0.18	32.24	0.06	0.91	0.10	100.36	0.895	0.039
DHN08	8/8	rim	54.15	0.12	4.97	0.32	6.47	0.16	32.34	0.09	0.86	0.14	99.62	0.899	0.041
DHN09	55/91	core	54.55	0.11	4.42	0.40	6.16	0.14	32.65	0.10	0.77	0.11	99.41	0.904	0.057
DHN09	57/100	rim	55.22	0.09	4.05	0.40	6.17	0.13	32.64	0.11	0.73	0.06	99.60	0.904	0.062
DHN11	10/150	core	54.42	0.20	3.31	0.26	11.64	0.24	29.73	0.06	0.64	0.02	100.52	0.820	0.050
DHN11	10/152	rim	55.00	0.16	2.96	0.21	11.48	0.25	30.08	0.02	0.67	0.01	100.84	0.824	0.045
DHN12	73/237	core	56.56	0.04	2.19	0.47	5.45	0.14	34.36	0.10	0.71	0.03	100.05	0.918	0.126
DHN12	73/239	rim	56.44	0.07	2.01	0.50	5.34	0.12	34.17	0.08	0.67	0.03	99.43	0.919	0.143
DHN16	47/60	core	54.26	0.13	4.69	0.42	6.11	0.10	32.60	0.07	0.83	0.16	99.37	0.905	0.057
DHN16	47/64	rim	55.26	0.07	4.28	0.32	6.20	0.16	32.71	0.07	0.78	0.19	100.04	0.904	0.048
DHS02	38/288	core	55.18	0.09	4.74	0.64	5.85	0.15	32.38	0.00	1.08	0.11	100.22	0.908	0.083
DHS02	38/286	rim	55.23	0.13	4.75	0.59	5.86	0.12	32.37	0.00	1.12	0.08	100.25	0.908	0.077
DHS03	43/34	core	54.62	0.13	4.93	0.46	6.06	0.15	32.45	0.15	0.90	0.13	99.98	0.905	0.059
DHS03	43/37	rim	55.38	0.08	4.69	0.37	6.25	0.16	32.39	0.08	0.80	0.07	100.27	0.902	0.050
DHS04	63/136	core	54.18	0.16	4.81	0.38	6.66	0.12	32.07	0.12	0.87	0.08	99.45	0.896	0.050
DHS04	63/140	rim	54.45	0.11	4.74	0.35	6.59	0.12	32.14	0.09	0.87	0.12	99.58	0.897	0.047
DHS05	29/43	core	53.64	0.15	4.91	0.37	6.06	0.17	32.80	0.11	0.82	0.10	99.13	0.906	0.048
DHS05	23/6	rim	55.01	0.08	4.57	0.36	6.17	0.15	33.05	0.08	0.80	0.10	100.37	0.905	0.050
DHS06	9/4	core	54.95	0.05	4.12	0.54	5.97	0.15	33.16	0.14	0.81	0.14	100.03	0.908	0.081
DHS06	3/1	rim	55.62	0.04	3.77	0.50	5.92	0.18	33.29	0.13	0.80	0.10	100.35	0.909	0.082
DHS07	50A/160	core	54.92	0.10	4.84	0.35	6.45	0.13	32.39	0.05	0.87	0.10	100.20	0.899	0.046
DHS07	50A/161	rim	54.59	0.13	4.78	0.34	6.40	0.11	32.41	0.08	0.88	0.09	99.81	0.900	0.046
DHS08	t22	core	54.86	0.07	4.36	0.40	6.20	0.15	32.65	0.07	0.80	0.06	99.62	0.904	0.058
DHS08	46/46	rim	54.05	0.07	4.24	0.37	6.21	0.18	32.48	0.10	0.78	0.06	98.54	0.903	0.055
DHS11	86/337	core	55.01	0.09	4.46	0.37	6.06	0.14	32.91	0.07	0.82	0.08	100.01	0.906	0.053
DHS11	88/346	rim	54.85	0.12	4.48	0.42	6.05	0.11	32.91	0.10	0.80	0.11	99.95	0.906	0.059
DHS13	81/280	core	53.50	0.13	4.33	0.52	10.59	0.34	29.17	0.09	0.92	0.09	99.68	0.831	0.075
DHS13	81/276	rim	53.75	0.12	3.76	0.45	10.22	0.27	29.79	0.06	1.02	0.10	99.54	0.839	0.074
DHS14	95/392	core	54.67	0.10	4.37	0.31	6.43	0.12	32.38	0.09	0.76	0.10	99.33	0.900	0.045
DHS14	92/378	rim	55.09	0.05	4.08	0.27	6.25	0.17	32.91	0.07	0.79	0.09	99.77	0.904	0.043
DHS15	75/248	core	54.67	0.10	4.42	0.46	6.08	0.16	32.44	0.06	0.82	0.09	99.30	0.905	0.065
DHS15	75/246	rim	54.73	0.10	4.20	0.42	6.09	0.12	32.54	0.06	0.81	0.08	99.15	0.905	0.063
DHS16	106/442	core	54.34	0.08	4.70	0.37	6.07	0.11	32.60	0.11	0.84	0.10	99.32	0.905	0.050
DHS16	111/463	rim	54.79	0.06	4.60	0.36	6.19	0.14	32.42	0.11	0.82	0.09	99.58	0.903	0.050
DHS17	108/48	core	54.23	0.10	4.85	0.48	6.25	0.13	32.64	–	0.86	0.12	99.66	0.903	0.062
DHS17	108/45	rim	54.93	0.10	4.38	0.41	6.18	0.14	32.63	–	0.81	0.11	99.69	0.904	0.059
DHS18	73/128	core	53.63	0.16	5.22	0.45	6.32	0.16	32.52	0.17	0.90	0.13	99.66	0.902	0.055
DHS18	73/120	rim	54.18	0.12	4.78	0.37	6.29	0.15	32.47	0.12	0.83	0.10	99.41	0.902	0.049
DHS20	35/268	core	54.56	0.12	4.70	0.42	6.45	0.14	32.43	0.10	0.86	0.10	99.88	0.900	0.057
DHS20	35/270	rim	54.74	0.10	4.58	0.40	6.22	0.12	32.57	0.15	0.85	0.13	99.86	0.903	0.055
DHS21	60/8	core	54.03	0.03	4.73	0.61	6.09	0.14	32.47	0.04	0.97	0.10	99.21	0.905	0.080
DHS21	64/82	rim	55.14	0.08	4.05	0.37	5.86	0.17	33.03	0.09	0.81	0.12	99.72	0.909	0.058
DHS25	31/221	core	54.77	0.17	4.98	0.37	6.39	0.17	32.20	0.08	0.87	0.12	100.12	0.900	0.047
DHS25	31/223	rim	54.98	0.15	4.82	0.39	6.49	0.16	32.48	0.12	0.84	0.11	100.54	0.899	0.051
DHX02hzb	17/3	core	56.74	0.04	2.25	0.39	5.44	0.17	34.54	0.09	0.56	0.22	100.44	0.919	0.104
DHX02hzb	17/1	rim	56.29	0.07	2.17	0.38	5.60	0.12	34.69	0.15	0.59	0.13	100.19	0.917	0.105
DHX02wbt	21B/4	core	56.10	0.06	2.78	0.41	5.43	0.15	34.35	0.09	0.57	0.10	100.04	0.919	0.090
DHX02wbt	21B/1	rim	56.11	0.04	2.67	0.35	5.50	0.16	34.53	0.04	0.57	0.15	100.12	0.918	0.081
DHX03	29/91	core	53.56	0.13	5.25	0.45	5.95	0.14	32.49	0.11	0.87	0.14	99.09	0.907	0.054
DHX03	35/132	rim	54.80	0.08	4.34	0.34	6.59	0.17	32.24	0.09	0.88	0.14	99.67	0.897	0.050

[a]Using $Fe^{2+} = Fe_{total}$.

Table 1c. Petrography and Representative Mineral Compositions of Xenoliths From Dish Hill

			Clinopyroxene												
Sample	Analysis	Location	SiO_2	TiO_2	Al_2O_3	Cr_2O_3	FeO	MnO	MgO	NiO	CaO	Na_2O	Total	Mg #[a]	Cr #
DHE01	1/3	core	53.81	0.12	3.62	1.72	2.65	0.09	16.54	0.07	21.02	1.28	100.92	0.918	0.242
DHE01	6/2	rim	54.01	0.12	3.57	1.58	2.59	0.08	16.67	0.08	20.98	1.25	100.93	0.920	0.229
DHE03	2/75	core	50.72	0.39	6.41	1.01	4.05	0.11	15.49	–	19.57	1.33	99.08	0.872	0.096
DHE03	4/86	rim	51.25	0.37	6.61	0.96	3.68	0.11	15.56	–	19.67	1.36	99.57	0.883	0.089
DHE04	49/3	core	51.92	0.56	7.21	0.87	2.82	0.09	15.18	0.07	20.32	1.81	100.85	0.906	0.075
DHE04	47/8	rim	51.56	0.48	6.61	0.72	3.04	0.10	15.43	0.07	20.30	1.65	99.96	0.900	0.068
DHE10	20/128	core	52.15	0.44	7.08	0.84	3.55	0.09	15.79	0.06	19.74	1.44	101.18	0.888	0.074
DHE10	20/126	rim	51.94	0.45	6.91	0.76	3.61	0.09	15.74	0.05	20.08	1.34	100.97	0.886	0.069
DHE11	54/3	core	52.06	0.26	5.25	1.34	3.02	0.12	16.56	0.03	19.79	1.27	99.70	0.907	0.146
DHE11	54/1	rim	51.74	0.47	5.59	1.15	3.21	0.13	16.48	0.02	19.68	1.41	99.88	0.901	0.121
DHE12	28/4	core	53.47	0.01	2.44	1.02	2.28	0.05	17.79	0.06	21.85	0.69	99.66	0.933	0.219
DHE12	30/1	rim	53.92	0.03	2.47	1.18	2.39	0.09	17.88	0.01	21.86	0.71	100.54	0.930	0.243
DHE13	41/3	core	51.60	0.29	5.91	1.36	3.54	0.11	15.66	0.00	19.50	1.52	99.49	0.887	0.134
DHE13	41/1	rim	51.56	0.27	5.88	1.11	3.51	0.09	15.88	0.06	19.47	1.45	99.28	0.890	0.113
DHN01	97/399	core	51.39	0.32	6.25	1.17	3.18	0.11	15.86	0.05	19.91	1.35	99.59	0.899	0.112
DHN01	97/401	rim	51.37	0.33	6.26	1.16	3.20	0.08	16.07	0.05	20.11	1.30	99.93	0.900	0.111
DHN05	22/177	core	53.01	0.08	4.54	1.35	2.99	0.10	17.08	0.02	21.04	0.83	101.04	0.911	0.166
DHN05	22/179	rim	53.12	0.07	4.52	1.19	3.03	0.08	16.93	0.05	20.83	0.75	100.57	0.909	0.150
DHN07	25/57	core	51.44	0.61	7.33	0.70	2.84	0.10	14.81	0.02	19.87	1.84	99.56	0.903	0.060
DHN07	25/54	rim	51.39	0.58	7.06	0.66	2.83	0.10	15.11	0.08	19.88	1.80	99.49	0.905	0.059
DHN08	9/43	core	50.83	0.63	7.48	0.67	3.38	0.12	15.04	0.05	19.64	1.62	99.46	0.888	0.057
DHN08	9/39	rim	51.20	0.49	7.15	0.58	3.49	0.09	15.36	0.03	19.98	1.50	99.87	0.887	0.052
DHN09	59/114	core	51.57	0.46	7.09	0.88	2.61	0.11	14.98	0.04	20.00	1.82	99.56	0.911	0.077
DHN09	59/111	rim	52.19	0.46	6.38	0.76	2.77	0.07	15.20	0.03	20.56	1.63	100.05	0.907	0.074
DHN11	9/140	core	51.17	0.72	4.85	0.51	4.97	0.15	15.32	0.01	22.76	0.53	100.99	0.846	0.066
DHN11	9/142	rim	51.92	0.67	4.22	0.48	4.69	0.14	15.42	0.01	23.22	0.42	101.19	0.854	0.071
DHN12	72/232	core	53.61	0.13	2.74	1.18	2.10	0.07	16.83	0.06	22.82	0.79	100.33	0.935	0.224
DHN12	72/230	rim	53.96	0.12	2.65	1.07	2.12	0.06	16.91	0.04	22.83	0.74	100.50	0.934	0.213
DHN16	48/69	core	50.96	0.45	6.89	0.74	2.99	0.06	15.13	0.01	20.64	1.45	99.32	0.900	0.067
DHN16	48/66	rim	51.49	0.32	6.01	0.68	3.01	0.11	15.49	0.03	20.66	1.48	99.28	0.902	0.071
DHS02	39/283	core	51.98	0.37	6.20	1.23	3.21	0.10	16.17	0.04	20.17	1.25	100.72	0.900	0.117
DHS02	39/285	rim	52.02	0.32	6.22	1.12	3.29	0.08	16.22	0.04	20.08	1.25	100.64	0.898	0.108
DHS03	38835	core	50.80	0.51	7.02	1.07	2.88	0.08	15.26	0.00	19.89	1.74	99.25	0.904	0.093
DHS03	42/24	rim	50.66	0.51	6.89	0.88	3.01	0.09	15.37	0.09	20.04	1.64	99.18	0.901	0.079
DHS04	64/143	core	51.09	0.57	7.26	0.78	3.32	0.09	15.08	0.03	19.91	1.65	99.78	0.890	0.067
DHS04	64/144	rim	51.30	0.51	6.83	0.79	3.45	0.12	15.16	0.06	20.06	1.53	99.81	0.887	0.072
DHS05	24/3	core	51.39	0.49	7.12	0.89	3.11	0.12	15.00	0.12	19.81	1.72	99.77	0.896	0.077
DHS05	24/5	rim	52.09	0.36	6.49	0.70	3.05	0.08	15.38	0.01	20.13	1.54	99.83	0.900	0.067
DHS06	5/3	core	52.41	0.14	5.19	1.06	2.72	0.10	15.97	0.04	20.75	1.44	99.82	0.913	0.121
DHS06	2/5	rim	52.55	0.14	5.23	1.12	2.93	0.11	15.90	0.00	20.65	1.44	100.07	0.906	0.126
DHS07	52A/171	core	51.54	0.54	7.34	0.76	3.30	0.08	15.19	0.02	19.85	1.71	100.33	0.891	0.065
DHS07	52A/173	rim	51.53	0.55	7.11	0.76	3.35	0.09	15.10	0.04	19.95	1.56	100.04	0.889	0.067
DHS08	44/31	core	51.09	0.40	6.83	0.93	2.85	0.08	15.06	0.03	20.03	1.66	98.96	0.904	0.084
DHS08	44/34	rim	51.80	0.31	6.16	0.82	3.22	0.08	15.55	0.03	20.77	1.42	100.16	0.896	0.082
DHS11	85/330	core	51.54	0.56	6.87	0.89	2.96	0.10	15.13	0.03	20.43	1.69	100.20	0.901	0.080
DHS11	87/340	rim	51.67	0.46	6.69	0.92	3.06	0.06	15.16	0.06	20.46	1.65	100.19	0.898	0.084
DHS13	82/285	core	51.19	0.41	5.73	1.09	5.29	0.20	14.76	0.04	19.92	1.39	100.02	0.833	0.113
DHS13	82/287	rim	50.74	0.39	6.24	1.14	5.52	0.15	14.37	0.00	19.77	1.44	99.76	0.823	0.109
DHS14	96/396	core	51.19	0.51	6.90	0.73	3.21	0.09	14.97	0.02	20.58	1.52	99.72	0.893	0.066
DHS14	91/377	rim	51.76	0.44	6.47	0.71	3.30	0.10	15.04	0.07	20.85	1.47	100.21	0.890	0.069
DHS15	74/243	core	51.80	0.34	6.44	1.10	2.96	0.08	15.14	0.04	20.21	1.67	99.78	0.901	0.103
DHS15	74/245	rim	51.77	0.35	6.20	0.98	3.04	0.07	15.25	0.06	20.49	1.52	99.73	0.899	0.096
DHS16	109/455	core	51.58	0.35	7.19	0.85	2.72	0.11	15.34	0.06	19.99	1.70	99.89	0.910	0.073
DHS16	110/459	rim	51.79	0.39	6.71	0.75	2.96	0.10	15.23	0.07	20.12	1.59	99.71	0.902	0.070
DHS17	109/58	core	51.17	0.48	7.08	0.98	2.96	0.10	14.96	–	20.00	1.79	99.52	0.900	0.085
DHS17	102/89	rim	51.45	0.50	6.88	0.95	2.90	0.08	14.85	–	20.04	1.72	99.37	0.901	0.085
DHS18	75/151	core	50.60	0.52	7.53	0.83	2.83	0.11	15.32	0.03	19.38	1.90	99.05	0.906	0.069
DHS18	75/143	rim	50.51	0.49	7.11	0.76	3.18	0.08	15.34	0.06	19.90	1.58	99.01	0.896	0.067
DHS20	34/263	core	51.98	0.46	7.17	0.96	3.02	0.09	15.12	0.05	20.09	1.65	100.59	0.899	0.082
DHS20	34/261	rim	52.21	0.48	6.83	0.87	3.10	0.09	15.29	0.06	20.27	1.61	100.81	0.898	0.079
DHS21	68/27	core	51.27	0.29	6.46	1.06	3.03	0.11	15.44	0.03	20.36	1.57	99.62	0.901	0.099
DHS21	63/80	rim	51.13	0.21	5.66	0.91	3.28	0.08	15.89	0.03	20.53	1.38	99.10	0.896	0.097
DHS25	29/211	core	51.88	0.59	7.24	0.81	3.29	0.12	15.02	0.04	19.97	1.67	100.63	0.891	0.070
DHS25	29/209	rim	51.71	0.52	6.90	0.77	3.32	0.05	15.16	0.06	20.18	1.59	100.26	0.891	0.070
DHX02hzb	16/3	core	53.25	0.25	3.61	1.26	2.19	0.09	16.55	0.06	22.19	1.16	100.61	0.931	0.190
DHX02hzb	16/4	rim	53.03	0.25	3.55	1.11	2.26	0.05	16.61	0.04	22.36	1.07	100.33	0.929	0.173
DHX02wbt	21A/4	core	52.51	0.28	4.43	0.95	2.27	0.07	16.49	0.06	21.90	1.04	100.00	0.928	0.126
DHX02wbt	21A/6	rim	52.43	0.23	3.93	0.89	2.23	0.07	16.52	0.03	22.29	1.02	99.64	0.930	0.132
DHX03	33av	core	51.02	0.44	6.87	0.88	3.46	0.12	14.87	0.07	20.23	1.47	99.43	0.885	0.079
DHX03	34/127	rim	51.01	0.29	6.06	0.74	3.46	0.11	15.31	0.04	20.66	1.36	99.04	0.887	0.076

[a]Using $Fe^{2+} = Fe_{total}$.

Table 1d. Petrography and Representative Mineral Compositions of Xenoliths From Dish Hill

			Spinel									
Sample	Analysis	Location	TiO_2	Al_2O_3	Cr_2O_3	FeO	MnO	MgO	NiO	Total	Mg #[a]	Cr #
DHE01	4/4	core	0.17	28.82	38.03	16.00	0.19	16.00	0.22	99.43	0.792	0.471
DHE03	3/66	core	0.15	52.09	14.00	13.17	0.12	19.38	0.42	99.33	0.821	0.153
DHE04	43/3	core	0.06	57.92	9.98	11.02	0.18	20.34	0.40	99.90	0.811	0.104
DHE10	16/107	core	0.19	55.01	12.17	12.62	0.13	20.18	0.44	100.74	0.826	0.130
DHE11	55/3	core	0.48	45.90	21.16	12.92	0.25	19.06	0.43	100.20	0.818	0.237
DHE11	55/1	rim	0.48	46.83	19.55	12.98	0.19	19.00	0.34	99.37	0.814	0.220
DHE12	24/3	core	0.09	24.02	43.91	15.47	0.40	15.15	0.17	99.21	0.765	0.552
DHE13	39/7	core	0.19	45.84	20.31	14.24	0.23	17.93	0.33	99.07	0.788	0.230
DHN01	100/412	core	0.16	49.55	17.35	12.10	0.13	19.20	0.35	98.84	0.811	0.191
DHN05	24/188	core	0.09	38.89	29.18	13.98	0.15	17.33	0.27	99.89	0.775	0.336
DHN07	20/22	core	0.12	58.09	9.06	10.75	0.15	20.04	0.43	98.64	0.801	0.095
DHN08	1/52	core	0.07	59.11	7.87	11.31	0.15	20.64	0.42	99.57	0.828	0.082
DHN09	60/119	core	0.09	56.55	10.84	10.75	0.12	20.28	0.32	98.95	0.816	0.115
DHN11	11/155	core	0.47	47.54	13.96	24.03	0.19	13.98	0.25	100.42	0.651	0.165
DHN12	68/212	core	0.15	30.14	38.43	14.49	0.19	15.40	0.19	98.99	0.715	0.462
DHN16	45/47	core	0.05	56.23	10.76	11.43	0.18	19.77	0.42	98.84	0.806	0.114
DHS02	41/297	core	0.16	49.92	17.40	12.41	0.12	19.68	0.34	100.03	0.828	0.190
DHS03	38/3	core	0.14	55.39	11.86	11.14	0.17	19.86	0.39	98.95	0.806	0.126
DHS04	66/151	core	0.12	56.50	9.59	12.24	0.11	20.30	0.39	99.25	0.836	0.103
DHS05	26/21	core	0.07	57.06	10.22	11.02	0.16	20.94	0.43	99.90	0.849	0.108
DHS06	1/3	core	0.07	48.03	19.24	12.34	0.23	18.68	0.25	98.84	0.795	0.213
DHS07	49A/179	core	0.12	56.56	10.10	11.97	0.11	20.18	0.42	99.46	0.824	0.108
DHS08	43/24	core	0.08	54.49	12.04	11.98	0.10	19.62	0.39	98.70	0.811	0.130
DHS11	89/353	core	0.11	56.03	11.07	11.02	0.10	20.25	0.40	98.98	0.822	0.118
DHS13	79/268	core	0.21	45.50	15.32	22.24	0.21	15.43	0.32	99.23	0.760	0.185
DHS14	94/390	core	0.06	56.79	9.75	11.73	0.09	20.16	0.38	98.96	0.823	0.104
DHS16	107/448	core	0.08	57.10	10.09	11.19	0.10	20.41	0.37	99.34	0.823	0.107
DHS17	103/45	core	0.05	55.42	11.96	11.33	0.11	20.37	0.40	99.64	0.831	0.127
DHS18	71/112	core	0.08	57.65	9.80	11.16	0.17	20.34	0.39	99.59	0.816	0.103
DHS20	36/273	core	0.13	55.42	11.89	11.90	0.10	19.73	0.36	99.53	0.800	0.126
DHS21	61/65	core	0.07	52.48	14.52	12.04	0.18	19.28	0.35	98.92	0.802	0.157
DHS25	32/228	core	0.13	57.19	10.28	12.09	0.11	20.30	0.35	100.45	0.815	0.108
DHX02hzb	11/4	core	0.15	35.30	32.20	13.88	0.32	16.44	0.14	98.43	0.754	0.381
DHX02wbt	18/3	core	0.11	38.94	29.48	13.31	0.27	17.11	0.20	99.42	0.756	0.338

[a]Using Fe^{2+} calculated from charge balance.

and is the only type II xenolith we have examined; it marginally contains fragments of the host peridotite.

[17] We classified the textures of xenoliths using the systematics of *Pike and Schwarzman* [1977] (Tables 1a–1d). The vast majority of lherzolites and harzburgites are medium to coarse grained and have allotriomorphic granular and porphyroclastic textures. In samples belonging to the latter texture type, porphyroclasts commonly consist of 1–5 mm large, slightly deformed, and locally kinked orthopyroxene grains, which rarely contain fine clinopyroxene exsolution lamellae. Olivine porphyroclasts occur in just a few samples, and display undulose extinction and/or kink bands. In several xenoliths orthopyroxene, olivine and spinel grains host rounded inclusions of each other, but only exceptionally include clinopyroxene (in sample DHS04). Clinopyroxene mainly occurs as disseminated, in some places amoeboid grains commonly located at triple junctions among olivines and/or orthopyroxenes (mainly in harzburgites and clinopyroxene-poor lherzolites), and in association with orthopyroxene clusters, where it could represent recrystallized exsolutions of high-temperature pyroxenes or products of infiltrated melts (in all peridotites). Alternatively, clinopyroxene also occurs in lherzolites as distinct grain clusters. Fine-grained composite xenolith DHX02 is the only one dominated by equigranular-mosaic texture; the websterite vein crosscutting it preserves relic igneous features like spinel inclusions in poikilitic clinopyroxene. The other websterites are allotriomorphic granular, indicating long-standing high-temperature subsolidus reequilibration and, like vein DHX02wbt, locally preserve relic evidence of their igneous origin.

[18] Apart from the fine-grained and strongly foliated lherzolite DHS06, textural anisotropy is poor or absent in most of the xenoliths. Where visible, the weak foliation is marked by parallel trails of elongated spinel grains. Oblate olivine aggregates in samples DHS11, DHS16 and DHS18 also contribute to foliation. Individual silicate grains do not display shape-preferred orientation in these samples, suggesting extensive recrystallization in strain-free conditions.

[19] Amphibole is the only hydrous mineral observed in these xenoliths. About 15% of the lherzolites and harzburgites contain trace amounts (<1%) of late-formed Ti-pargasite and kaersutite either as disseminated interstitial grains, as reaction rims around spinel grains, rarely as metasomatic replacements of clinopyroxene along rims and cleavages, or as late veinlets. Although interstitial and vein-related phlogopite and plagioclase have been reported in rare xenoliths from Dish Hill [*Wilshire and Trask*, 1971; *Wilshire et al.*, 1988], none of these phases are present in the samples studied here.

[20] Most samples lack the visible reaction products commonly induced by decompression and melt infiltration during xenolith ascent. Except for lherzolite DHN08, in which most of the clinopyroxene grains are surrounded by thick sieve-textured olivine + plagioclase + secondary clinopyroxene coronas, rare pyrometamorphic microtex-

Table 2a. Trace Element Concentrations in Parts per Million in Clinopyroxenes From Dish Hill[a]

	Samples																					
	DHE01	DHE03	DHE10	DHN01	DHN05	DHN09	DHN12	DHS02	DHS04	DHS05	DHS07	DHS08	DHS11	DHS13	DHS14	DHS15	DHS16	DHS17	DHS20	DHS25	DHX02 hzb	DHX02 wbt
Li	0.869	2.06	1.86	1.22	1.4	1.42	0.925	1.08	2.77	2.54	2.3	2.31	1.43	2.54	2.15	2.32	1.49	1.87	1.12	1.77	1.94	1.94
Ti	736	2312	2711	1957	507	3064	760	2002	3360	2806	3122	2318	3395	2353	2947	2068	2359	2963	2583	3555	1110	1080
Rb	0.013	0.072	0.0111	0.0159	0.0388	0.0193	0.0054	0.004	0.0357	0.117	0.0267	0.032	0.0069	bd	0.017	0.0603	0.036	0.0745	0.0061	0.0222	0.0981	0.0701
Sr	11.3	43.9	53.3	32	14.8	61.5	82.7	42.1	53.8	39.6	58.6	34	59.3	61.4	43.2	44.6	49.5	54.2	36.7	57.4	75.8	69
Y	4.84	13.4	15.1	11.6	4.62	16.4	4.99	12.1	16.4	16.6	17.3	14.4	18.8	13.7	18.1	12.3	15.5	16.3	13	17.5	7.61	8.01
Zr	7.35	17.3	17.9	12.1	3.26	21.9	18.2	15.3	26.1	20.3	26.5	10.9	26.6	20	27.7	14.6	24.3	25.4	13.9	29.2	13.3	11.5
Nb	0.413	0.201	0.429	0.773	0.0469	0.275	0.614	0.679	0.0217	0.0287	0.0587	0.0431	0.276	0.313	0.207	0.215	0.479	0.122	0.348	0.182	0.35	0.258
Ba	0.0343	0.0676	0.0437	0.187	0.2	0.0154	0.0472	0.156	0.0092	0.0072	0.0111	0.0099	0.126	0.0185	0.0114	0.0313	0.0994	0.0162	0.0248	0.0112	0.189	0.203
La	0.108	0.729	1.32	0.607	0.227	1.23	2.32	0.926	0.888	0.365	0.822	0.748	0.665	0.708	0.673	1.65	0.688	1.14	0.276	0.975	0.494	0.471
Ce	0.437	2.52	4.26	1.95	0.866	4.56	7.51	2.57	3.59	2.08	3.49	2.19	3.45	2.56	3.41	3.56	2.62	3.68	1.28	4.16	1.92	1.9
Pr	0.111	0.451	0.616	0.346	0.145	0.703	1.18	0.44	0.66	0.46	0.666	0.372	0.672	0.484	0.62	0.48	0.46	0.604	0.304	0.721	0.344	0.348
Nd	0.974	2.84	3.41	2.19	0.805	3.71	5.84	2.85	3.88	3.14	4	2.2	4.05	3.02	3.51	2.5	2.56	3.5	2.29	4.23	2.14	2.2
Sm	0.591	1.25	1.44	1.03	0.313	1.52	1.36	1.24	1.6	1.47	1.6	1.01	1.71	1.31	1.36	1	1.12	1.5	1.23	1.74	0.797	0.839
Eu	0.235	0.533	0.605	0.428	0.134	0.656	0.497	0.517	0.684	0.657	0.68	0.445	0.684	0.544	0.586	0.439	0.501	0.64	0.54	0.724	0.355	0.374
Gd	0.769	2.06	2.11	1.58	0.538	2.25	1.31	1.83	2.52	2.4	2.54	1.84	2.29	1.92	2	1.71	1.66	2.39	1.9	2.54	1.16	1.22
Tb	0.132	0.353	0.368	0.28	0.0955	0.395	0.179	0.306	0.428	0.425	0.445	0.332	0.405	0.328	0.355	0.308	0.304	0.414	0.328	0.445	0.193	0.202
Dy	0.862	2.54	2.64	2.05	0.744	2.87	1.04	2.19	3.08	3	3.22	2.49	3.03	2.39	2.82	2.24	2.41	2.86	2.38	3.09	1.39	1.46
Ho	0.19	0.56	0.611	0.481	0.179	0.665	0.201	0.503	0.654	0.676	0.699	0.567	0.733	0.564	0.691	0.5	0.607	0.611	0.54	0.709	0.274	0.293
Er	0.525	1.57	1.67	1.36	0.548	1.88	0.527	1.38	1.86	1.98	1.97	1.67	2.11	1.57	2.02	1.43	1.81	1.78	1.53	1.96	0.777	0.816
Yb	0.483	1.46	1.55	1.29	0.578	1.78	0.447	1.26	1.8	1.95	1.91	1.66	1.97	1.47	1.95	1.42	1.79	1.67	1.55	1.85	0.684	0.721
Lu	0.0698	0.203	0.219	0.181	0.0852	0.245	0.0658	0.174	0.25	0.273	0.266	0.233	0.279	0.21	0.289	0.194	0.253	0.233	0.209	0.27	0.0948	0.1
Hf	0.286	0.674	0.746	0.49	0.12	0.752	0.466	0.619	0.81	0.729	0.838	0.397	0.896	0.682	0.656	0.506	0.606	0.816	0.573	0.977	0.434	0.362
Ta	0.0049	0.0069	0.0173	0.0233	bd	0.0152	0.0845	0.0679	0.0091	bd	0.0105	0.0063	bd	0.005	0.0028	0.0209	0.0079	0.0147	0.0028	0.0083	0.0133	0.0105
Pb	0.0203	0.0382	0.0336	0.0333	0.0079	0.0162	0.0339	0.015	0.031	0.0216	0.0166	0.0398	0.0067	0.0595	0.0111	0.0455	0.0326	0.0765	0.0142	0.0218	0.276	0.551
Ti/Ti*	0.415	0.530	0.577	0.571	0.452	0.605	0.224	0.494	0.615	0.537	0.571	0.612	0.651	0.553	0.653	0.572	0.620	0.576	0.613	0.630	0.415	0.384
Sr/Sr*	0.936	1.089	1.039	1.034	1.225	1.078	0.891	1.056	0.949	0.920	1.011	1.059	1.013	1.429	0.826	1.152	1.288	1.051	1.220	0.928	2.489	2.216
Zr/Zr*	0.627	0.616	0.542	0.539	0.439	0.622	0.433	0.545	0.707	0.631	0.709	0.487	0.682	0.678	0.858	0.621	0.966	0.745	0.545	0.725	0.688	0.572
Hf/Hf*	0.906	0.888	0.838	0.809	0.601	0.794	0.411	0.820	0.813	0.839	0.830	0.659	0.851	0.856	0.754	0.798	0.893	0.889	0.836	0.900	0.836	0.668
Pb/Pb*	0.388	0.155	0.090	0.176	0.097	0.039	0.049	0.061	0.087	0.095	0.047	0.191	0.019	0.231	0.033	0.151	0.129	0.223	0.096	0.054	1.468	2.940

[a]All data are from laser ablation inductively coupled plasma mass spectrometry (LA-ICP-MS) except for Ti, which is from electron microprobe; bd, below detection limit.

Table 2b. Trace Element Concentrations in Parts per Million in Cima Xenoliths[a]

	Samples						SC99-2 cpx Standard	
	CIP98-1	CIP98-12	CIP98-62	CIP98-66	CIP98-76	CIP98-8	Mean (Eight Analyses)	1 SD
Li	1.98	4.91	1.41	2.11	2.37	1.62	2.28	0.81
Ti	3082	3621	1852	4789	4622	1477		
Rb	0.041	0.0707	0.0313	0.0464	0.0396	0.0342	0.0174	0.0113
Sr	21.5	28.7	70.8	20	6.42	69.9	37.0	1.2
Y	17.4	15.9	10.5	21.3	21.3	7.07	23.8	0.6
Zr	15.4	26.7	13.6	55.7	26.8	14.5	27.8	0.6
Nb	0.137	0.105	0.0969	0.144	0.141	0.652	0.151	0.035
Ba	0.0134	0.0771	0.0638	0.138	0.0095	0.0583	0.0862	0.0751
La	1.36	1.6	1.57	1.63	1.25	2.82	0.35	0.01
Ce	4.18	4.56	4.77	6.23	3.89	8.47	2.69	0.06
Pr	0.612	0.744	0.68	1.17	0.695	1.28	0.650	0.013
Nd	3.36	4.19	3.12	7.23	4.44	6.18	4.52	0.13
Sm	1.43	1.69	0.929	2.86	2.07	1.49	2.03	0.05
Eu	0.642	0.711	0.381	1.06	0.787	0.456	0.849	0.012
Gd	2.41	2.6	1.47	4.01	3.31	1.35	3.27	0.07
Tb	0.427	0.441	0.259	0.659	0.57	0.201	0.568	0.012
Dy	3.11	3.09	1.84	4.29	4.05	1.24	4.11	0.13
Ho	0.68	0.64	0.401	0.879	0.866	0.264	0.88	0.03
Er	1.95	1.85	1.18	2.37	2.43	0.782	2.40	0.07
Yb	1.9	1.7	1.15	2.05	2.22	0.746	2.32	0.09
Lu	0.255	0.231	0.162	0.279	0.297	0.106	0.339	0.012
Hf	0.62	0.89	0.469	1.95	1.05	0.32	1.15	0.05
Ta	0	0.0083	0.0142	0.0255	0.0027	0.0868	0.0012	0.0007
Pb	0.0281	0.0477	0.0438	0.0354	0.0452	0.0492	0.0212	0.0087
Ti/Ti*	0.595	0.639	0.594	0.557	0.685	0.450		
Sr/Sr*	0.423	0.460	1.375	0.193	0.103	0.704		
Zr/Zr*	0.471	0.677	0.542	0.826	0.590	0.321		
Hf/Hf*	0.704	0.838	0.693	1.074	0.861	0.263		
Pb/Pb*	0.076	0.113	0.106	0.057	0.119	0.065		

[a]All data are from LA-ICP-MS except for Ti, which is from electron microprobe.

tures are restricted to thin glass + quench mineral envelopes coating some spinel and amphibole grains and to micron-size secondary clinopyroxene formed at the expense of primary clinopyroxene grains traversed by melt-infiltrated veinlets. Xenolith-basanite contacts are preserved in a few samples only, and are characterized by 1–5 mm thick reaction zones dominated by micron-size breakdown products of orthopyroxene and clinopyroxene plus glass.

4.2. Major Element Compositions of Minerals

[21] Minerals from 24 lherzolites, 8 harzburgites, 2 websterites, and composite xenolith DHX02 (harzburgite + websterite vein) were analyzed in detail. Composition profiles were analyzed on 2–4 grains per phase. Representative olivine, orthopyroxene, clinopyroxene, and spinel compositions are shown in Tables 1a–1d.

4.2.1. Olivine

[22] Olivine grains are homogeneous in all samples. Except for lherzolite DHS13 with 83.9% Fo and lherzolite DHE03 with 88.4% Fo possibly reflecting various degrees of metasomatism from neighboring mafic veins, peridotitic olivines range between 89.6 and 91.7% Fo and 0.006–0.010 Ni p.f.u. (per formula unit). Lherzolites contain olivine with Fo < 90.7%, whereas harzburgites are dominated by olivine with Fo > 90.8%. Olivines belonging to the two rock types largely overlap in their Ni content, although the lower and the higher ends of the range are characteristic for lherzolites and for harzburgites, respectively. Amphibole-spinel websterite DHN11 contains olivine with 80.4% Fo and 0.004 Ni p.f.u., which are the lowest values in the whole suite. On the other extreme, olivine in the amphibole-bearing spinel websterite vein DHX02wbt has 91.5% Fo, which is similar to the Fo 91.7% olivine in its host harzburgite; its 0.009 Ni p.f.u. is among the highest observed.

4.2.2. Orthopyroxene

[23] Orthopyroxenes are enstatite with Mg # = 0.89–0.92 and Cr # = 0.039–0.159 in all but one peridotite (Mg # = Mg/(Mg + Fe_{tot}), Cr # = Cr/(Cr + Al); cation ratios, Fe_{tot} = total iron as ferrous). In comparison, lherzolite DHS13 hosts orthopyroxene with similar Cr # = 0.075, but significantly lower Mg # = 0.83. Orthopyroxenes in lherzolites are confined to Mg # < 0.91 and Cr # < 0.09, and are relatively Al-rich (0.152–0.225 Al p.f.u.), whereas those in harzburgites are characterized by Mg # > 0.90, Cr # > 0.08, and lower Al contents (0.078–0.166 Al p.f.u.). Apart from the medium- to fine-grained samples in which matrix grains are dominantly homogeneous, most of the xenoliths contain chemically zoned orthopyroxene. Where present, porphyroclasts usually display higher Al, Cr, and Ca and lower Mg contents in cores than in rims (e.g., DHN08, DHS03, DHS17, DHS21, and DHX03). Highest concentration gradients are preserved in porphyroclasts in lherzolite DHX03, in which core-to-rim variations encompass 0.222–0.177 Al, 0.012–0.009 Cr, 0.045–0.033 Ca, and 1.660–1.693 Mg p.f.u. In other xenoliths, however, porphyroclasts displaying distinct Al, Cr and Mg zonation are homogeneous with respect to Ca (e.g., DHS05 and DHS15), and are indicative of diffusional decoupling of these components. Orthopyroxene neoblasts in coarse-grained allotriomorphic granular samples preserve similar, though much attenuated Al zonation, and show no variations in their Ca content. In contrast, porphyroclasts in lherzolite DHS13 show core-to-rim decrease of Al and increase of Ca. Websterite vein DHX02wbt contains orthopyroxene that is in average more aluminous

Table 3. Sm and Nd Concentrations and Nd Isotope Data in Clinopyroxenes From Dish Hill and Cima Xenoliths[a]

Sample	Sm (ppm)	Nd (ppm)	$^{143}Nd/^{144}Nd$ (0)	ε_{Nd}	T_{CHUR}	T_{DM}
			Dish Hill			
DHE01	1.31	3.19	0.513175	10.5	1.58	0.35
DHE03	na	na	0.513233	11.6	1.29	0.41
DHE10	1.09	2.38	0.513314	13.2	1.28	0.56
DHN01	1.02	2.11	0.513059	8.2	0.67	−0.12
DHN11	1.24	2.69	0.513445	15.7	1.50	0.89
DHN12	0.97	4.15	0.511970	−13.0	1.83	2.15
DHS05	na	na	0.513357	14.0	1.27	0.61
DHS07	na	na	0.512931	5.7	1.00	−1.46
DHS08	1.33	2.61	0.513463	16.1	1.13	0.62
DHS11	1.22	3.01	0.513341	13.7	2.21	1.50
DHS20	1.02	2.13	0.513289	12.7	1.07	0.40
DHX02hzb	0.50	1.27	0.512050	−11.5	−2.30	−12.05
DHX02wbt	0.81	1.96	0.512310	−6.4	−0.96	−4.60
			Cima			
LZ-MC-05	1.76	6.09	0.512324	−6.1	2.17	2.53
LZ-MC-06	0.98	3.41	0.512477	−3.1	1.08	2.01
LZ-MC-25	1.98	4.36	0.512634	−0.1	−0.01	−1.40

[a]Value ε_{Nd} was calculated using present-day $^{143}Nd/^{144}Nd$ (0). T_{CHUR} and T_{DM} are Nd model ages in Ga; present-day values are $^{143}Nd/^{144}Nd_{CHUR}$ = 0.512638, $^{147}Sm/^{144}Nd_{CHUR}$ = 0.1967, $^{143}Nd/^{144}Nd_{DM}$ = 0.513114, and $^{147}Sm/^{144}Nd_{DM}$ = 0.222. Sm/Nd and Nd model ages for DHE03, DHS05, and DHS07 were calculated from laser ablation ICP-MS data; na, not available.

(0.111 Al p.f.u.) and poorer in Cr (Cr # = 0.086) than orthopyroxene in the host harzburgite DHX02hzb (0.088 Al p.f.u., Cr # = 0.105), and has similar Mg # = 0.92. The Mg # = 0.82 of orthopyroxene in websterite DHN11 represents the lowest value in the whole xenolith suite.

4.2.3. Clinopyroxene

[24] Most clinopyroxenes in the spinel peridotites are dominantly homogeneous or poorly zoned Cr-diopside with Mg # = 0.87–0.94, Cr # = 0.05–0.25, 0.100–0.330 Al, 0.045–0.134 Na and <0.020 Ti p.f.u. Clinopyroxene in lherzolites are characterized by Mg # < 0.92, Cr # < 0.13, and Al > 0.265, Na > 0.087 and Ti > 0.004 p.f.u., whereas those in harzburgites tend to be more refractory, having Mg # > 0.90, Cr # > 0.12, and Al < 0.239, Na < 0.1 and Ti < 0.013 p.f.u. Lherzolite DHS13 has exceptionally low Mg #, between 0.82 and 0.83, but has Cr # and Al content well within the ranges of the suite. Where present, zonation of clinopyroxenes is, as a rule, expressed by core-to-rim enrichment in Ca, Mg and, in some samples, in Fe; these elemental enrichments are compensated by depletion in Al, Na, and, to a lesser extent, Cr. Weak reverse trends were observed across clinopyroxenes in samples DHE12 and DHN05. Lherzolite DHX03 displays the largest amplitude of core-to-rim variations, 0.789–0.808 Ca, 0.804–0.834 Mg, 0.100–0.112 Fe, 0.300–0.253 Al, 0.111–0.090 Na and 0.028–0.021 Cr p.f.u. A similar but slightly attenuated zonation trend characterizes clinopyroxenes from lherzolite xenoliths DHN09, DHS08 and DHS18; the amplitude of compositional variations in clinopyroxenes from the other samples is less than half of that shown for DHX03. Compositions of clinopyroxene in websterite vein DHX02wbt lies within the range of those analyzed in peridotites. Clinopyroxene in websterite DHN11, on the other hand, is richer in Ti (0.018–0.023 Ti p.f.u.) and has Mg # as low as 0.85.

4.2.4. Spinel

[25] Spinel grains are homogeneous in most of the peridotites. The range of Cr # = 0.22–0.55 representative for harzburgitic spinels indicates a markedly refractory character compared to the Cr # = 0.08–0.23 of the lherzolitic ones. The Mg #s of spinels range from 0.71 to 0.85, where the lower end is dominated by harzburgites (Mg # < 0.82) and the higher end by lherzolites (Mg # > 0.79). Lherzolite DHS13 containing spinel with Mg # = 0.76 is an outlier. Lherzolite DHX03 contains two types of spinel, both represented by homogeneous grains: those in olivine and orthopyroxene dominated microdomains are more magnesian (Mg # = 0.76) and less chromian (Cr # = 0.11) than those associated with clinopyroxene clusters (Mg # = 0.67 and Cr # = 0.13). Chemical zonation in spinels was

Table 4a. Whole-Rock Compositions of Dish Hill Peridotites: Major Element XRF Analyses

		Weight Percent															
Sample	Rock[a]	SiO_2	TiO_2	Al_2O_3	Cr_2O_3	FeO	MnO	MgO	NiO	CaO	Na_2O	K_2O	P_2O_5	Total	LOI	Mg #[b]	Cr #
DHE01	hzb	42.7	0.02	0.89	0.37	7.62	0.12	45.5	0.34	0.74	0.01	0.02	0.01	98.3	0.11		
DHE03	lhz	43.3	0.08	2.25	0.33	9.89	0.15	41.4	0.26	1.78	0.12	0.01	0.01	99.6	–	0.882	0.089
DHE04	lhz	44.3	0.10	3.21	0.38	8.56	0.15	40.6	0.27	2.58	0.19	0.00	0.01	100.4	–	0.894	0.074
DHE12	hzb	43.4	0.02	0.69	0.38	7.35	0.12	46.2	0.33	0.49	0.02	0.02	0.04	99.1	–	0.918	0.270
DHE13	lhz	44.8	0.09	2.05	0.39	8.50	0.14	42.6	0.29	1.44	0.10	0.01	0.01	100.4	–	0.899	0.114
DHN01	lhz	44.0	0.10	2.20	0.37	7.70	0.13	41.9	0.30	2.27	0.13	0.02	0.01	99.1	0.18	0.906	0.102
DHN05	hzb	43.4	0.05	1.36	0.38	7.84	0.13	43.8	0.32	1.09	0.02	0.02	0.01	98.4	−0.41	0.909	0.157
DHS02	lhz	43.4	0.06	2.20	0.36	7.69	0.12	41.9	0.30	1.13	0.05	0.02	0.02	97.3	−0.27	0.907	0.098
DHS03	lhz	43.8	0.09	2.93	0.43	8.20	0.13	40.8	0.28	2.36	0.19	0.02	0.01	99.2	–	0.899	0.090
DHS04	lhz	43.2	0.11	3.55	0.42	8.19	0.13	38.7	0.27	2.97	0.22	0.01	0.01	97.9	−0.40	0.894	0.074
DHS05	lhz	44.1	0.11	3.25	0.38	7.70	0.13	39.0	0.27	3.13	0.23	0.01	0.01	98.3	−0.34	0.900	0.073
DHS07	lhz	43.0	0.11	3.16	0.37	8.27	0.14	39.7	0.28	2.75	0.20	0.01	0.01	97.9	−0.48	0.895	0.073
DHS08	lhz	44.0	0.08	3.23	0.45	7.78	0.13	39.9	0.27	2.64	0.18	0.02	0.01	98.6	−0.29	0.901	0.086
DHS11	lhz	42.8	0.08	2.63	0.34	8.15	0.13	41.4	0.29	1.76	0.14	0.01	0.01	97.8	−0.46	0.901	0.079
DHS14	lhz	43.5	0.11	3.47	0.41	7.80	0.13	38.1	0.27	2.99	0.22	0.01	0.01	97.0	−0.36	0.897	0.073
DHS16	lhz	44.0	0.09	3.70	0.46	7.66	0.13	38.5	0.26	3.14	0.23	0.01	0.02	98.2	−0.38	0.900	0.077
DHS17	lhz	43.4	0.08	2.64	0.35	8.04	0.13	41.3	0.30	2.01	0.14	0.02	0.02	98.5	−0.40	0.902	0.083
DHS20	lhz	44.4	0.11	3.57	0.48	7.73	0.13	38.5	0.26	2.96	0.20	0.02	0.02	98.4	0.59	0.899	0.082
DHS21	lhz	44.5	0.06	2.63	0.41	7.96	0.13	41.6	0.29	2.23	0.21	0.03	0.02	100.0	–	0.903	0.094
DHS25	lhz	44.1	0.13	3.69	0.42	7.98	0.13	38.5	0.26	3.43	0.25	0.02	0.02	98.9	−0.26	0.896	0.071
DHX03	lhz	44.3	0.10	3.23	0.39	8.76	0.16	39.2	0.27	2.76	0.20	0.01	0.01	99.5	na	0.889	0.076

[a]Rock abbreviations are hzb, harzburgite; lhz, lherzolite.
[b]Using $Fe^{2+} = Fe_{total}$.

Table 4b. Whole-Rock Compositions of Dish Hill Peridotites: Trace Element XRF Analyses and Recalculated Mineral Modes[a]

	Parts per Million							Weight Percent			
Sample	Sc	V	Sr	Zr	Y	Cu	Zn	olv	opx	cpx	spl
DHE01	6.3	28	4.6	5.5	2.1	16	49	81.1	15.4	2.7	0.8
DHE03	11	53	4.6	5.3	2.9	9.0	59	71.5	19.3	7.8	1.5
DHE04	14	71	5.2	6.3	3.5	15	64	61.9	24.3	12	2.1
DHE12	5.9	21	11	5.9	1.5	9.4	47	79.1	19.1	1.1	0.7
DHE13	11	50	4.3	4.9	1.7	24	55	67.8	26.1	5.2	0.9
DHN01	12	56	8.5	7.2	2.5	19	50	67.4	21.7	9.9	1.0
DHN05	8.3	40	4.8	6.6	2.6	17	51	74.9	20.2	3.7	1.2
DHS02	9.0	46	5.0	7.0	2.0	21	49	68.1	26.6	3.9	1.4
DHS03	12	61	6.0	5.3	3.4	15	54	63.4	24.0	11	2.0
DHS04	14	73	12	8.3	5.5	31	60	59.3	24.3	14	2.4
DHS05	15	74	9.4	7.7	4.8	27	48	59.3	23.8	15	1.8
DHS07	12	69	11	8.7	4.4	32	55	64.7	19.9	13	2.3
DHS08	13	72	10	5.4	3.7	13	53	58.6	27.3	12	2.3
DHS11	11	55	7.9	8.1	3.2	12	53	68.1	22.1	7.8	2.0
DHS14	14	77	10	8.8	4.5	20	53	57.0	26.7	14	2.5
DHS16	16	79	9.4	8.6	4.3	18	54	57.6	25.1	15	2.7
DHS17	11	58	8.1	8.2	4.1	17	52	65.3	24.4	8.8	1.5
DHS20	16	76	8.4	7.3	4.7	33	53	56.6	27.7	13	2.4
DHS21	12	54	13	9.4	3.2	11	52	63.6	24.9	9.7	1.7
DHS25	16	77	13	10	4.8	25	53	57.9	23.6	16	2.5
DHX03	15	68	8.1	5.2	3.6	21	65	59.7	25.6	12	2.2

[a]Mineral abbreviations are olv, olivine; opx, orthopyroxene; cpx, clinopyroxene; spl, spinel.

observed in a limited number of samples, and is restricted to core-to-rim decrease of #Cr. Harzburgite DHE11 contains spinel grains with 1.455–1.480 Al and 0.450–0.418 Cr p.f.u., which represents the maximum zonation amplitude we observed in Dish Hill spinels. Spinel in websterite vein DHX02wbt is less chromian (Cr # = 0.34) than that equilibrated in the host harzburgite (Cr # = 0.38). The spinel in websterite DHN11 is the most ferroan (Mg # = 0.51) of the whole xenolith suite; its Cr # = 0.17 lies well within the range of the lherzolitic spinels from Dish Hill.

4.3. Trace Element Compositions of Clinopyroxenes From Peridotites

[26] Trace element abundances in clinopyroxene from 21 xenoliths from Dish Hill are summarized in Table 2a. Representative trace element contents in type I peridotitic clinopyroxenes from Cima are tabulated for comparison in Table 2b.

[27] Two types of peridotites can be distinguished at Dish Hill on the basis of the relative abundances of LREEs and HREEs (Figure 2) in clinopyroxenes. Harzburgite DHN12 containing clinopyroxene with LREE-enriched profile is a type IB xenolith [*Frey and Green*, 1974]. Clinopyroxene in this xenolith displays a smoothly descending slope from Nd to Yb, and CI chondrite-normalized $(Ce/Yb)_{CI}$ = 4.41. All other analyzed samples contain LREE depleted clinopyroxenes and are, according to the same systematics, type IA xenoliths. Most of these clinopyroxenes are characterized by nearly flat HREE-MREE patterns and show various degrees of LREE depletion, $(Ce/Yb)_{CI}$ = 0.22–0.72. As exceptions, clinopyroxenes in harzburgites DHE01 and DHX02hzb display upward convex REE patterns with apexes in the MREE range. All examined lherzolites contain LREE depleted clinopyroxenes with MREE and HREE concentrations confined to a narrow range, 1–1.74 ppm Sm, 1.29–1.97 ppm Yb, $(MREE, HREE)_{CI}$ = 6.79–13.42. Clinopyroxenes from harzburgites DHE01, DHN05 and DHX02hzb contain only 0.48–0.68 ppm Yb, being markedly more depleted in HREE than the other samples. However, their relative LREE depletions, $(Ce/Yb)_{CI}$ = 0.24–0.74, are broadly similar to those found in other clinopyroxenes from the suite. Overall, LREE depletions are significantly less pronounced than expected from fractional melting scenarios commonly seen in abyssal peridotites (Figure 2b) [*Johnson et al.*, 1990]. The few previously reported type IA clinopyroxene REE patterns from Dish Hill are similar to our results in the MREE-HREE range, but show significant LREE scattering (Figure 2a). While one of

Table 4c. Whole-Rock Compositions of Dish Hill Peridotites: Reconstructed Major Element Compositions

		Weight Percent												
Sample	Rock[a]	SiO_2	TiO_2	Al_2O_3	Cr_2O_3	FeO	MnO	MgO	NiO	CaO	Na_2O	Total	Mg #[b]	Cr #
DHE10	lhz	43.9	0.07	2.23	0.31	8.84	0.14	42.6	0.30	1.97	0.14	100.5	0.896	0.086
DHE11	hzb	44.3	0.04	1.27	0.29	8.03	0.12	44.6	0.34	1.29	0.10	100.4	0.908	0.132
DHN09	lhz	44.3	0.09	3.62	0.54	8.01	0.13	40.0	0.26	2.51	0.22	99.7	0.899	0.091
DHN16	lhz	44.7	0.11	3.77	0.53	7.58	0.14	38.8	0.29	3.55	0.27	99.7	0.901	0.086
DHS06	lhz	43.8	0.03	2.08	0.58	8.06	0.14	42.9	0.30	1.97	0.21	100.1	0.905	0.158
DHS15[c]	lhz	43.8	0.04	1.21	0.17	8.31	0.13	43.4	0.30	1.42	0.11	98.9	0.903	0.084
DHS18	lhz	43.5	0.11	3.22	0.41	7.94	0.14	40.7	0.28	2.56	0.29	99.2	0.901	0.079

[a]Rock abbreviations are hzb, harzburgite; lhz, lherzolite.
[b]Using $Fe^{2+} = Fe_{total}$.
[c]Composition estimated ignoring spinel, which was replaced by glass and quench crystals.

Table 4d. Whole-Rock Compositions of Dish Hill Peridotites: Mineral Modes From Point Counting[a]

	Weight Percent			
Sample	olv	opx	cpx	spl
DHE10	71.3	19.1	8.5	1.1
DHE11	74.7	19.9	5.1	0.3
DHN09	59.8	26.0	11	3.1
DHN16	55.9	25.3	16	2.6
DHS06	70.5	19.0	8.6	1.9
DHS15	74.2	19.5	6.0	0.3
DHS18	63.0	23.3	12	2.0

[a]Mineral abbreviations are olv, olivine; opx, orthopyroxene; cpx, clinopyroxene; spl, spinel.

the peridotites studied by *Johnson et al.* [1996] contains strongly LREE depleted clinopyroxene with $(Ce/Yb)_{CI}$ = 0.04, *Menzies et al.* [1985] and *Nielson et al.* [1993] identified significant LREE enrichment in peridotite xenoliths in contact with hornblendite dikes, showing that the transition from unmetasomatized type IA to strongly metasomatized type IB REE patterns in clinopyroxenes occurs at centimeter-decimeter scale. Thus, it is likely that some of the clinopyroxenes with higher LREE content observed in the present study indicate the proximity of such intrusions. As will be discussed below, the LREE-enriched profile of clinopyroxene from harzburgite DHN12 cannot be linked to such mafic veins. Clinopyroxenes in harzburgite DHX02hzb and hosted websterite DHX02wbt display remarkably similar trace element patterns indicating advanced degree of host-vein equilibration.

[28] Primitive mantle-normalized extended trace element patterns of clinopyroxenes from Dish Hill xenoliths (Figure 3) are marked by conspicuous negative anomalies for Ti, Zr, Hf, and (except for DHX02hzb) Pb, which are characteristic of clinopyroxenes from spinel facies peridotites that have undergone partial melting [e.g., *Salters and Shimizu*, 1988]. Apart from few outliers, for the type IA xenoliths, there are distinct negative correlations between the relative amplitude of the anomalies and the abundances of these elements (Figures 4a and 4b). For Zr, such correlation can be recognized in clinopyroxenes from abyssal peridotites [*Johnson et al.*, 1990] and as predicted by mineral-melt partition coefficients, likely reflect partial melting trends. The Ti-Ti/Ti* correlation, on the other hand, cannot be explained by partial melting, since the amplitude of Ti anomaly is not influenced by this process. Most samples show similar negative anomalies for the more incompatible Nb, which being more susceptible to metasomatic contaminations, also gained positive deviations in a small number of samples. Sr concentrations in clinopyroxenes from type IA lherzolites are limited to 32–62 ppm, and to 11–15 ppm in harzburgites DHE01 and DHN05, and show no significant spikes relative to adjacent elements in the pattern (Figure 4c). Moderate positive correlations between Sr and REE, HFSE (Figure 5) suggest that most type IA clinopyroxenes have not experienced significant hydrous metasomatic events that tend to decouple Sr from other similarly incompatible elements. In contrast, clinopyroxene in harzburgite DHX02hzb is distinctly enriched in Pb (0.25 ppm) and Sr (76 ppm), and displays positive Pb and Sr anomalies that have been induced probably by the injection of vein DHX02wbt. Except for the conspicuous enrichment in LREE and Sr, the trace element pattern of type IB harzburgite DHN12 resembles those from the type IA harzburgites.

[29] Clinopyroxenes in peridotites from Cima have on average higher concentrations of LREE and MREE than those from Dish Hill, and display a variety of REE patterns, some of which have not been identified in Dish Hill xenoliths (Figure 2a). Two samples are type IA xenoliths containing clinopyroxenes with nearly flat HREE-MREE patterns and $(Ce/Yb)_{CI} < 1$, and resemble the most fertile peridotites from Dish Hill. Another one is a type IB xenolith with clinopyroxene displaying $(Ce/Yb)_{CI} > 1$ similar to that in Dish Hill harzburgite DHN12. Two samples resemble DHX02hzb by having upward convex REE patterns. On the other hand, two samples with essentially flat REE pattern have no counterparts in clinopyroxenes from the Dish Hill peridotites. In contrast to type IA clinopyroxenes from Dish Hill, most trace element patterns of clinopyroxenes from Cima display strong negative Sr anomalies, show notable positive correlation between Sr and Sr/Sr*, and

Table 5. Whole-Rock REE Concentrations Recalculated From Clinopyroxene REE Concentrations and Mineral Modes[a]

Sample	La	Ce	Nd	Sm	Eu	Gd	Dy	Ho	Er	Yb	Lu
DHE01	0.003	0.0134	0.0276	0.0174	0.0072	0.0239	0.0301	0.007	0.0214	0.0243	0.004
DHE03	0.0571	0.115	0.227	0.103	0.0444	0.174	0.23	0.0527	0.156	0.166	0.025
DHE10	0.113	0.133	0.298	0.129	0.0548	0.194	0.258	0.0619	0.178	0.187	0.0286
DHN01	0.0606	0.129	0.222	0.106	0.0451	0.169	0.236	0.0576	0.172	0.189	0.029
DHN05	0.0086	0.0224	0.0321	0.0131	0.0058	0.0242	0.0383	0.0099	0.0333	0.044	0.0074
DHN09	0.138	0.2	0.42	0.174	0.0763	0.264	0.354	0.0841	0.249	0.263	0.0388
DHS02	0.0375	0.0522	0.122	0.0565	0.0247	0.091	0.128	0.0321	0.0981	0.116	0.0185
DHS04	0.125	0.254	0.554	0.231	0.1	0.371	0.474	0.103	0.303	0.321	0.0473
DHS05	0.0549	0.294	0.478	0.226	0.102	0.376	0.492	0.114	0.345	0.375	0.0559
DHS07	0.108	0.25	0.529	0.214	0.0919	0.345	0.454	0.101	0.293	0.306	0.0449
DHS08	0.0879	0.195	0.262	0.122	0.0544	0.228	0.323	0.0755	0.232	0.258	0.0388
DHS11	0.0519	0.154	0.32	0.137	0.0559	0.189	0.265	0.0661	0.201	0.212	0.0323
DHS14	0.0927	0.27	0.488	0.19	0.0832	0.286	0.42	0.105	0.319	0.34	0.0532
DHS15	0.099	0.0853	0.152	0.0624	0.0278	0.11	0.154	0.0356	0.108	0.124	0.0185
DHS16	0.101	0.263	0.379	0.167	0.0759	0.254	0.384	0.0986	0.305	0.329	0.0492
DHS17	0.101	0.149	0.316	0.137	0.0597	0.225	0.287	0.0635	0.195	0.21	0.0318
DHS20	0.0367	0.207	0.308	0.168	0.0748	0.266	0.349	0.0814	0.241	0.27	0.0388
DHS25	0.156	0.297	0.684	0.284	0.12	0.421	0.532	0.124	0.354	0.361	0.0553

[a]All values were recalculated according to *Witt-Eickschen and O'Neill* [2005], using T_{BKN} temperatures (Table 6; see text for details).

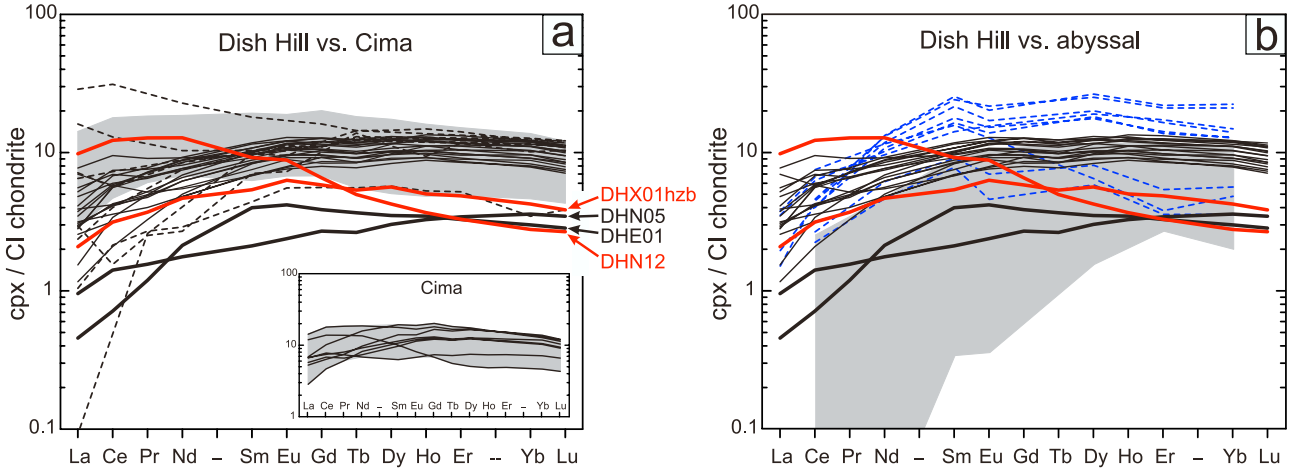

Figure 2. Chondrite-normalized rare earth element (REE) patterns of clinopyroxenes from Dish Hill peridotites. (a) Comparison with clinopyroxenes from Cima peridotites (gray field, detailed in inset) and previously reported peridotitic clinopyroxenes from Dish Hill (dashed lines) [*Menzies et al.*, 1985; *Nielson et al.*, 1993; *Johnson et al.*, 1996]. (b) Comparison with clinopyroxenes from abyssal peridotites, where the gray field shows various locations from *Johnson et al.* [1990] and the dashed lines show the East Romanche Fracture Zone from *Seyler and Bonatti* [1997]. Chondrite values are from *McDonough and Sun* [1995]. Solid thin lines and labeled bold lines are lherzolites and harzburgites, respectively. Details are given in text.

poor correlations between Ti and Ti/Ti*, and Zr and Zr/Zr* (Figure 4c). There are good negative correlations between Sr and HREE, Y, Ti, and positive correlations between Sr and Cr (Figure 5). Collectively, these observations suggest that unlike the Dish Hill type IA peridotites, all examined Cima samples have been affected by metasomatic processes capable of producing distinct Sr anomalies in clinopyroxenes. It is important to stress that, in this respect, clinopyroxenes from harzburgites DHN12 and DHX02hzb do not resemble those from the other peridotites from Dish Hill, but rather share trends observed in clinopyroxenes from Cima peridotites, and possibly shared their geochemical evolution, as well.

4.4. Nd Isotopic Composition of Clinopyroxenes

[30] The $^{143}Nd/^{144}Nd$ ratios in clinopyroxenes separated from 12 peridotites and 2 websterites from Dish Hill and 3 peridotites from Cima are presented in Table 3. Since clinopyroxene is the only significant Nd bearing phase in these peridotites, its $^{143}Nd/^{144}Nd$ is considered representative for the bulk samples. On the basis of $^{143}Nd/^{144}Nd$ ratios, the Dish Hill samples fall into two groups.

[31] The high-ε_{Nd} group, which includes only type IA peridotites plus websterite DHN11, is characterized by clinopyroxenes with radiogenic $^{143}Nd/^{144}Nd$ ranging between 0.51293 and 0.51346 (ε_{Nd} = 5.7 to 16.1) and according to *Menzies et al.* [1985] plot in the depleted mantle field (Figure 6). Similar values have been previously reported for nonmetasomatized clinopyroxenes in a composite xenolith from Dish Hill [*Menzies et al.*, 1985; *Nielson et al.*, 1993], and the entire data set also fits into the Sm/Nd versus $^{143}Nd/^{144}Nd$ cluster defined by clinopyroxenes in depleted peridotite xenoliths from the broader southwestern United States (e.g., San Carlos, Geronimo, Grand Canyon, and The Thumb [*Menzies et al.*, 1985; *Galer and O'Nions*, 1989; *Alibert*, 1994]). Sm/Nd and $^{143}Nd/^{144}Nd$ ratios of clinopyroxenes in mafic xenoliths of depleted mantle origin from Cima [*Mukasa and Wilshire*, 1997] fall in the same range. Samples DHN01 and DHS07 yield future T_{DM} model ages. Such anomalous ages can theoretically result either from a source more fertile than the reference DM depleted mantle model, or by metasomatic contamination driven by low-ε_{Nd} liquids.

[32] Harzburgites DHN12 and DHX02hzb, and websterite DHX02wbt define the low-ε_{Nd} group, and are characterized by clinopyroxenes having nonradiogenic $^{143}Nd/^{144}Nd$ that range between 0.51197 and 0.51231 ($\varepsilon_{Nd} = -13$ to -6.4). Clinopyroxene in DHN12 lies in the enriched mantle field (Figure 6) and thus shows affinities with clinopyroxenes in

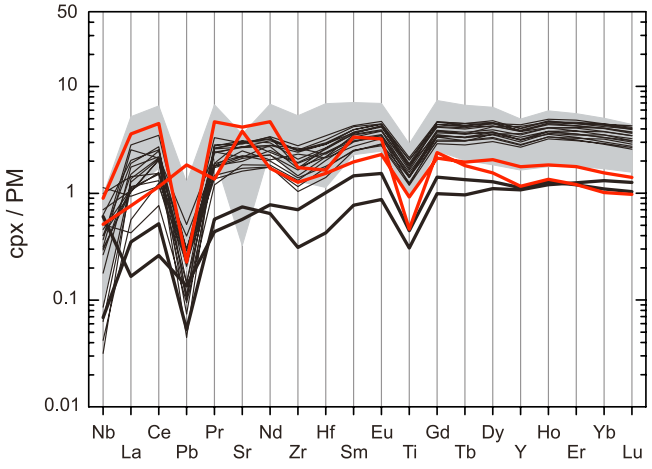

Figure 3. Primitive mantle-normalized extended trace element patterns of clinopyroxenes from Dish Hill and Cima peridotites. Primitive mantle (PM) values are from *McDonough and Sun* [1995]; patterns are the same as those in Figure 2.

Cima peridotite xenoliths (see *Mukasa and Wilshire* [1997] and our data in Table 3). Websterite vein DHX02wbt and its host harzburgite DHX02hzb contain clinopyroxenes that yield future T_{CHUR} and T_{DM} model ages. One possible explanation is recent melting of ancient metasomatized peridotites (e.g., enriched mantle; Figure 6) with low time-integrated Sm/Nd ratios. Such a process would preserve the ancient (enriched) $^{143}Nd/^{144}Nd$ signature, but produce a harzburgitic residuum with Sm/Nd ratios fractionated to higher values owing to preferential Nd depletion. Subsequent injection of a high $^{143}Nd/^{144}Nd$ – high Sm/Nd melt into the low $^{143}Nd/^{144}Nd$ – high Sm/Nd harzburgite could have generated the array trending toward MORB-like mantle (Figure 6). Such melts might have been parental to Dish Hill websterite DHN11 from Dish Hill and some mafic xenoliths from Cima [*Mukasa and Wilshire*, 1997] and also might have contaminated peridotite LZ-MC-25. An alternative explanation for the low $^{143}Nd/^{144}Nd$ samples could be that they resulted from pervasive reaction of high-ε_{Nd} peridotites with very low-ε_{Nd} mafic liquids.

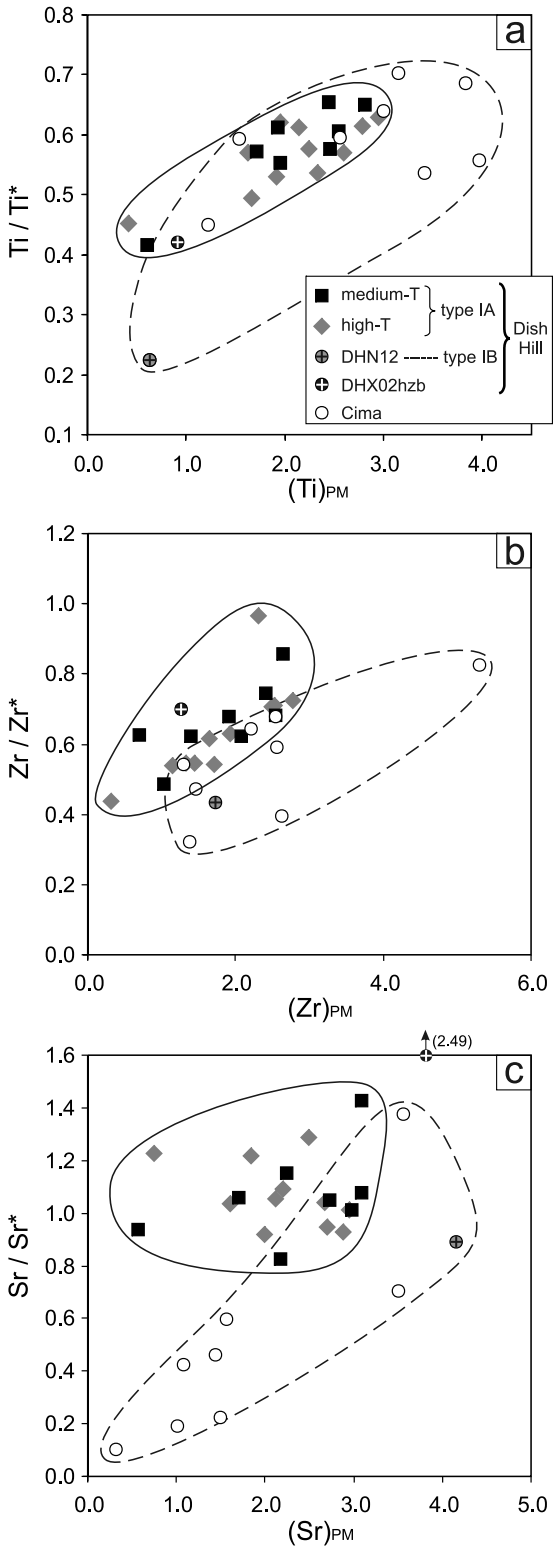

Figure 4. Relationships between (a) $(Ti)_{PM}$ and Ti/Ti*, (b) $(Zr)_{PM}$ and Zr/Zr*, and (c) $(Sr)_{PM}$ and Sr/Sr*, in clinopyroxenes from peridotite xenoliths from Dish Hill and Cima. Ti* = (Eu + Gd)/2, Zr* = (Nd + Sm)/2, and Sr* = (Pr + Nd)/2, where all values are normalized to PM. Solid line outlines the field of type IA peridotites from Dish Hill. Dashed line delimits the field defined by peridotites from Cima plus low-T samples DHN12 and DHX02hzb from Dish Hill. Low-T, medium-T, and high-T arrays are defined in text and Figure 11.

4.5. Peridotite Whole-Rock Chemistry and Modal Compositions

[33] Major and trace element compositions of representative spinel peridotites from Dish Hill obtained from XRF analyses are reported in Tables 4a and 4b. Compositions of peridotites reconstructed from mineral modes and compositions are presented in Tables 4c and 4d. Harzburgites are in general richer in MgO (43.83–46.25 wt %) and Ni (2478–2699 ppm), and poorer in Al_2O_3 (0.69–1.36 wt %), CaO (0.49–1.29 wt %) and Na_2O (0.01–0.10 wt %) than lherzolites, which have 38.10–43.43 wt % MgO, 2012–2384 ppm Ni, 1.21–3.77 wt % Al_2O_3, 1.13–3.55 wt % CaO, and 0.05–0.29 wt % Na_2O. The Mg # of the analyzed samples scatter in the 0.88–0.92 range, the more refractory harzburgites and the more fertile peridotites being delimited at Mg # = 0.91. The positive correlation of MgO with Ni, and its negative correlations with SiO_2, Al_2O_3, CaO, Na_2O, TiO_2, Sc, V, Y, and HREEs overlap the covariation arrays defined by spinel peridotites found world wide [*Maaløe and Aoki*, 1977; *McDonough*, 1990; *Griffin et al.*, 1999] and in particular in the southwestern United States [*Frey and Prinz*, 1978; *Smith*, 1979; *Ehrenberg*, 1982; *Wilshire et al.*, 1988, 1991; *Wilshire and Mukasa*, 1997; *Smith et al.*, 1999; *Lee et al.*, 2003; *Kil and Wendlandt*, 2007] (Figure 7). While the covariation of MgO with most major elements is similar to that found in abyssal peridotites [e.g., *Asimow*, 1999; *Baker and Beckett*, 1999], Dish Hill peridotites extend to more fertile compositions, and are, for any given MgO, richer in TiO_2 and Na_2O than most abyssal samples. This is a common feature of many continental and ocean island spinel peridotite xenoliths, but it has been also observed in some off-axis abyssal peridotites of the Romanche Fracture Zone [*Seyler and Bonatti*, 1997].

[34] The data presented in Tables 4a–4d are largely similar to previously published Dish Hill peridotite compositions [*Wilshire et al.*, 1988; *Lee et al.*, 2003], but appear to

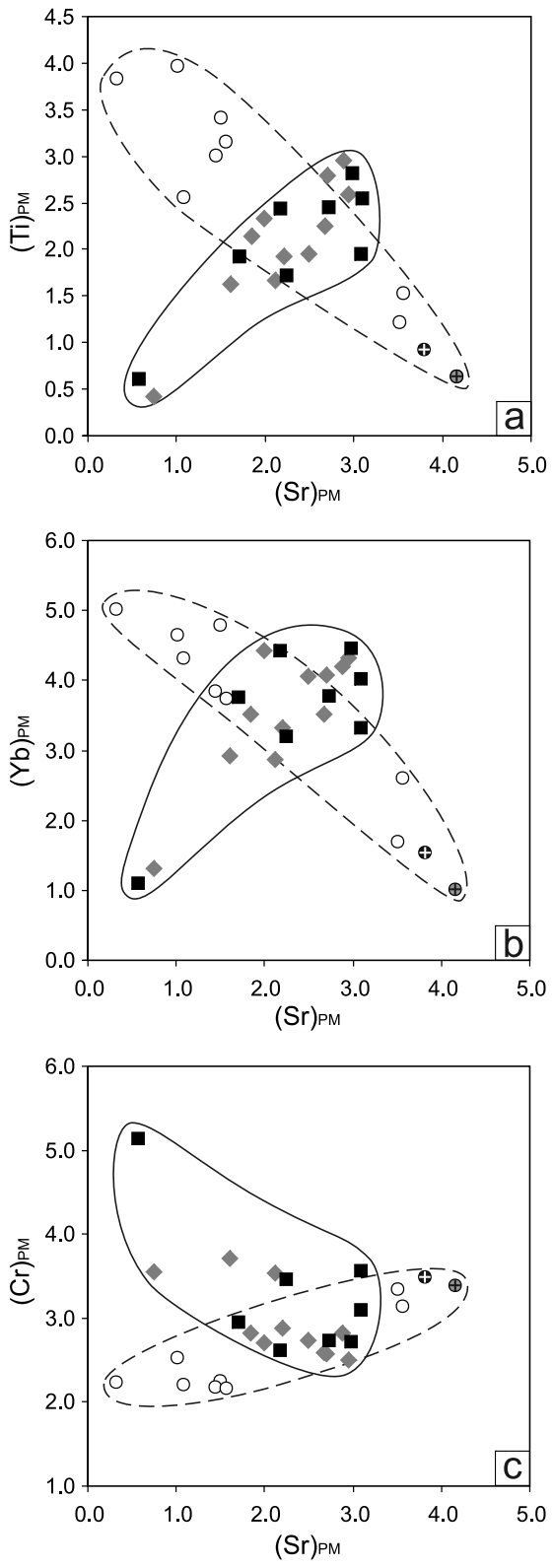

Figure 5. Relationships between $(Sr)_{PM}$ and (a) $(Ti)_{PM}$, (b) $(Yb)_{PM}$, and (c) $(Cr)_{PM}$, in clinopyroxenes from peridotite xenoliths from Dish Hill and Cima. Al values are normalized to primitive mantle [*McDonough and Sun*, 1995]. Solid line outlines the field of type IA peridotites from Dish Hill. See Figure 4 for symbols and details.

be poorer in Na_2O than samples reported by *Lee et al.* [2003], very likely due to the higher accuracy of XRF analyses used in the present study. Indeed, for the samples studied here, whole-rock Na_2O contents obtained from XRF overlap within error with whole-rock Na_2O contents reconstructed using clinopyroxene modes and Na_2O contents (linear regression is $Na_2O^{reconstructed} = 1.01 \cdot Na_2O^{XRF}$, $R^2 = 0.94$). Data from the Cima peridotite xenolith suite in general show larger scattering than those from Dish Hill.

[35] Mineral modes for 28 representative lherzolite and harzburgite xenoliths (Tables 4a–4d) indicate that Dish Hill lherzolites and harzburgites lie along the melting depletion trend of spinel peridotites (Figure 8). Their average composition, 65.5% olivine (1σ SD = 7.2), 23% orthopyroxene (1σ = 3.2), 9.8% clinopyroxene (1σ = 4.2), 1.8% spinel (1σ = 0.7) resembles the average of world-wide spinel peridotites [*Maaløe and Aoki*, 1977; *McDonough*, 1990]. These results differ slightly from the Dish Hill peridotite xenolith compositions obtained on the basis of field estimates [*Wilshire and Trask*, 1971; *Wilshire et al.*, 1988] that consistently yielded higher olivine modes and nearly equal orthopyroxene and clinopyroxene modes, and do not fit into the general depletion trend of spinel peridotites.

4.6. Mantle Geothermometry

4.6.1. Choice of Geothermometers

[36] Geothermometry based on equilibrium between coexisting orthopyroxene and clinopyroxene [*Wood and Banno*, 1973; *Wells*, 1977; *Bertrand and Mercier*, 1985; *Brey and Köhler*, 1990] can be used to estimate preeruption temperatures in spinel facies peridotite and websterite xenoliths. The geothermometer of *Brey and Köhler* [1990], T_{BKN}, is presently the most refined version of two-pyroxene thermometers as it is applicable to mantle rocks with Mg # > 80 and T > 900°C. The Ca-in-orthopyroxene geothermometer formulated by *Brey and Köhler* [1990], $T_{Ca\text{-}Opx}$, is based on the assumption that knowledge of the Ca content of only orthopyroxene (in equilibrium with clinopyroxene) is sufficient to retrieve equilibrium temperatures. Although less reliable than T_{BKN}, $T_{Ca\text{-}Opx}$ is also commonly applied to spinel facies peridotite xenoliths found world wide, and is thought to more accurately reflect equilibria below 1000°C than does T_{BKN} [*Smith*, 1999].

[37] Equilibrium temperatures in spinel facies peridotites can also be derived from orthopyroxene-spinel Cr-Al exchange equilibria [*Sachtleben and Seck*, 1981; *Witt-Eickschen and Seck*, 1991], and, ideally, Cr and Al contents in orthopyroxene are sufficient to obtain equilibrium temperatures ($T_{Cr/Al\text{-}opx}$) [*Witt-Eickschen and Seck*, 1991]. Because diffusion rates of Al and Cr in orthopyroxene are much lower than those of Ca in the temperature range of interest (800–1200°C) [*Smith and Barron*, 1991; *Witt-Eickschen and Seck*, 1991; *Griffin et al.*, 1996, and references therein], $T_{Cr/Al\text{-}Opx}$ may be the only geothermometer able to track long-term thermal histories recorded by zoned orthopyroxene porphyroclasts.

[38] We have estimated equilibrium temperatures for 34 xenoliths from Dish Hill on the basis of results from several geothermometers. In the following we will evaluate results from the most recent geothermometers, T_{BKN}, $T_{Ca\text{-}Opx}$, and $T_{Cr/Al\text{-}Opx}$ in comparison with temperatures obtained from

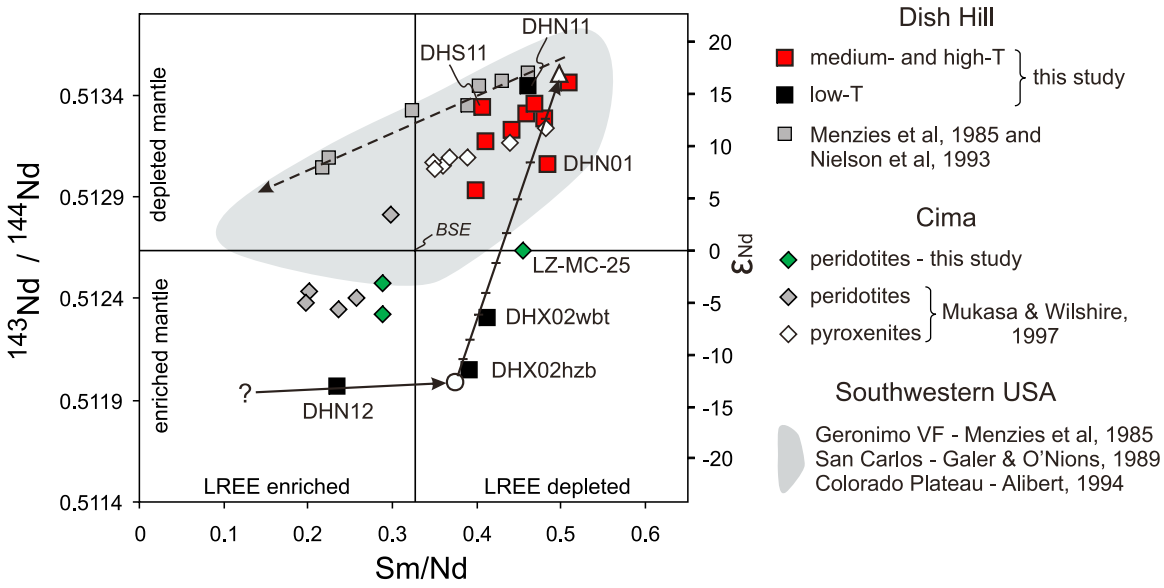

Figure 6. Sm/Nd versus Nd isotope ratios of clinopyroxenes from Dish Hill xenoliths in comparison with those from Cima and the broader southwestern United States. Diagram subdivisions are from *Menzies et al.* [1985]. The contamination trend observed in a Dish Hill peridotite crosscut by a low Sm/Nd mafic vein [*Nielson et al.*, 1993] is qualitatively reproduced by the dashed mixing line. Mixing line with tick marks suggests a possible origin of Sm/Nd and Nd isotope ratios in samples DHX02 and LZ-MC-25 as a result of percolation of mafic liquid with high Sm/Nd and Nd isotope ratios (open triangle) through a high Sm/Nd harzburgite (open circle) that resulted from partial melting of very low Sm/Nd peridotite (question mark). Details are given in text. BSE, bulk silicate earth.

two previous calibrations, T_W [*Wells*, 1977] and T_{BM} [*Bertrand and Mercier*, 1985] (corrected following the recommendation of *Brey and Köhler* [1990]). In the absence of reliable geobarometers applicable to spinel facies peridotites and websterites, we used 1.5 GPa as reference.

[39] Several xenoliths from Dish Hill, especially the allotriomorphic granular ones, are dominated by chemically homogeneous minerals suggesting thermodynamic equilibrium achieved at the hand sample length scale prior to eruption. These xenoliths are the most reliable to constrain the thermal state of the lithospheric mantle beneath Dish Hill at the time of eruption. On the other hand, xenoliths containing zoned minerals, like most of the porphyroclastic spinel peridotites, are valuable witnesses of the thermal evolution of the mantle, but require careful consideration in order to become useful in quantitative geothermometry. Most pyroxene grains displaying noticeable zonation indicate cooling. Diopside/enstatite ratios decrease rimward in orthopyroxenes, and increase rimward in clinopyroxenes, while the proportions of jadeite and tschermak components decrease from core to rim in both pyroxenes. Compositions of the outermost micron-scale rims may not obey this trend, and locally indicate very recent heating associated with the host magma or its precursor. To avoid the effects of host magma heating and melt infiltration, the outermost ~5 μm were excluded from our thermobarometric calculations. This length scale was chosen because the high rates of Fe-Mg interdiffusion in pyroxenes (compared to other cations used in thermobarometric calculations) allows for the calculation of a well documented upper bound on the diffusion length scales associated with xenolith entrainment [*Ganguly and Tazzoli*, 1994; *Dimanov and Sautter*, 2000]: diffusion length scales have been shown to not exceed 5 μm in the case of xenoliths ascending at rates >0.1 m/s [*Spera*, 1984] from depth <60 km for magma temperatures of 1100–1300°C. All "rim compositions" mentioned from here on refer to analyses acquired >5 μm away from grain boundaries. In the case of Dish Hill xenoliths, rim temperatures (T^{rim}) obtained in this way are indistinguishable from temperatures estimated from hypothetical preeruption outermost rim compositions reconstructed via linear extrapolation of near-rim compositions. To calculate T^{rim}, we used rim compositions of orthopyroxene and clinopyroxene grains in contact. In sample DHN08 pyrometamorphic coronas enveloping clinopyroxenes have erased such contacts; in this case, T^{rim} was estimated using clinopyroxene compositions next to these reaction products. Core compositions of pyroxene grains similar in size were used in order to calculate core temperatures (T^{core}). The application of two-pyroxene geothermometry to cores of orthopyroxene porphyroclasts is problematic, because clinopyroxene grains may be too small to preserve core compositions in equilibrium with the cores of the 3–10 times larger zoned orthopyroxene porphyroclasts. Moreover, the observation that these porphyroclasts contain only olivine and spinel inclusions suggests that orthopyroxene cores equilibrated in

Figure 7. Major element composition of peridotite xenoliths from Dish Hill in comparison with other xenoliths from the southwestern United States and selected abyssal peridotites.

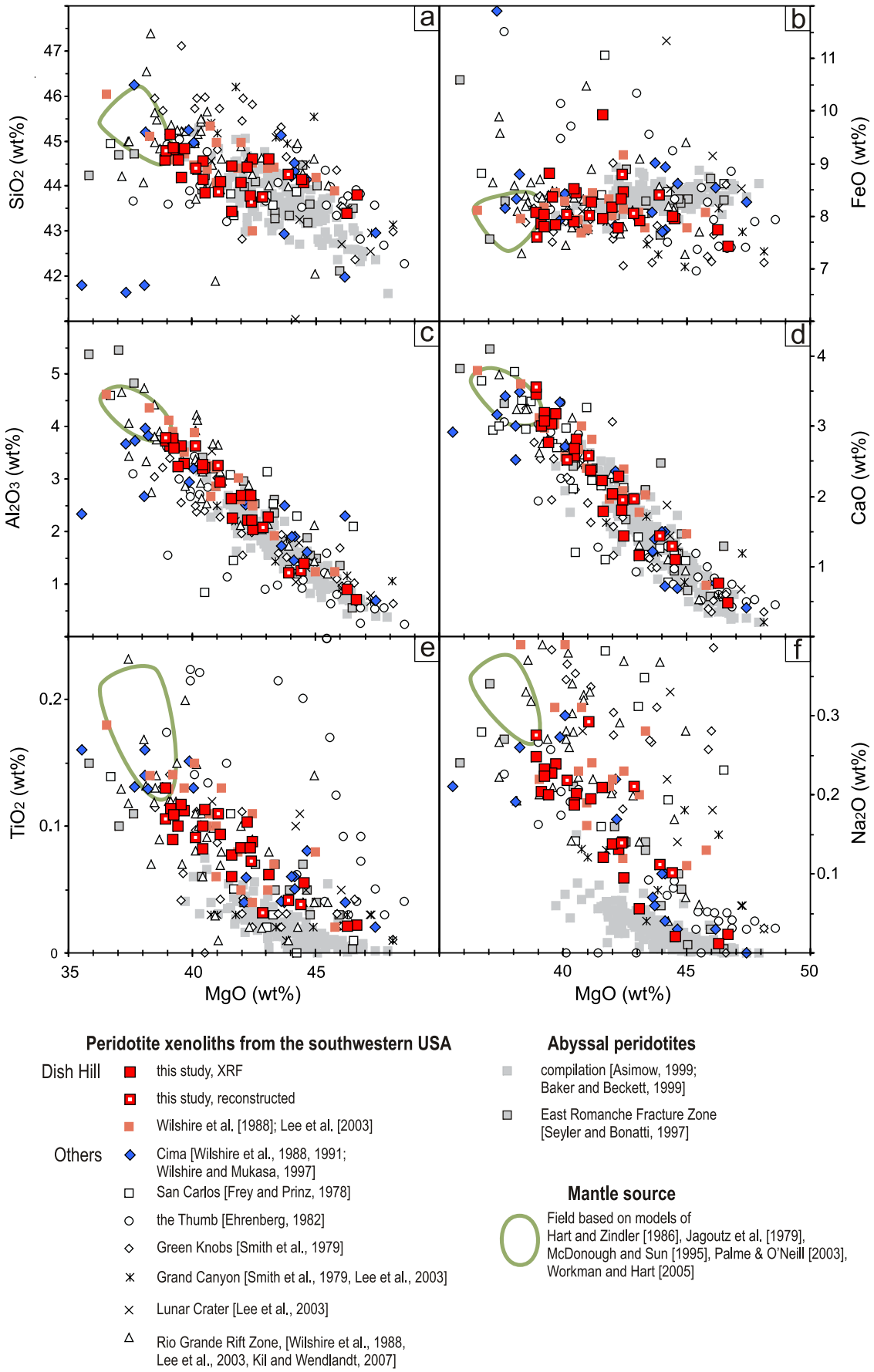
a
b
c
d
e
f
SiO2 (wt%)
FeO (wt%)
Al2O3 (wt%)
CaO (wt%)
TiO2 (wt%)
Na2O (wt%)
MgO (wt%)
MgO (wt%)
Peridotite xenoliths from the southwestern USA
Dish Hill
this study, XRF
this study, reconstructed
Wilshire et al. [1988]; Lee et al. [2003]
Others
Cima [Wilshire et al., 1988, 1991; Wilshire and Mukasa, 1997]
San Carlos [Frey and Prinz, 1978]
the Thumb [Ehrenberg, 1982]
Green Knobs [Smith et al., 1979]
Grand Canyon [Smith et al., 1979, Lee et al., 2003]
Lunar Crater [Lee et al., 2003]
Rio Grande Rift Zone, [Wilshire et al., 1988, Lee et al., 2003, Kil and Wendlandt, 2007]
Abyssal peridotites
compilation [Asimow, 1999; Baker and Beckett, 1999]
East Romanche Fracture Zone [Seyler and Bonatti, 1997]
Mantle source
Field based on models of Hart and Zindler [1986], Jagoutz et al. [1979], McDonough and Sun [1995], Palme & O'Neill [2003], Workman and Hart [2005]

Figure 7

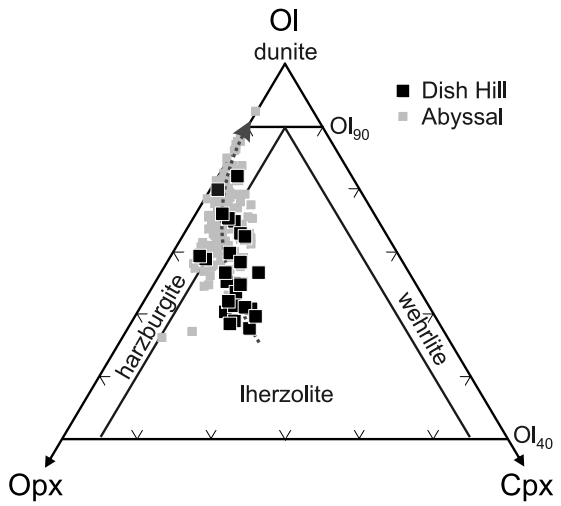

Figure 8. Modal composition of representative Dish Hill peridotites. Abyssal peridotites [*Asimow*, 1999; *Baker and Beckett*, 1999] are shown for comparison. The dashed arrow approximates the melt-depletion trend observed in worldwide spinel peridotites.

clinopyroxene-poor assemblage and that most clinopyroxene formed relatively late. In such conditions $T_{Cr/Al\text{-}Opx}$ may represent the only means to estimate temperatures at which cores of orthopyroxene porphyroclasts formed.

4.6.2. Geothermometry Results

[40] Temperature estimates for the vast majority of Dish Hill xenoliths fall in the 820–1100°C range (Table 6). All geothermometers but $T_{Cr/Al\text{-}Opx}$ yield for the majority of the xenoliths $\Delta T^{core\text{-}rim} = T^{core} - T^{rim}$ smaller than their individual calibration uncertainties (±15–19°C, 1σ; Figures 9a and 9b). This indicates that mineral zonations, where present, are too weak to significantly influence two-pyroxene geothermometry. As predicted by Ca profiles found in most of the zoned orthopyroxenes, $T_{Ca\text{-}Opx}$ yields small, dominantly positive $\Delta T^{core\text{-}rim}$ deviations that, even for most of the porphyroclasts, do not exceed the calibration uncertainty (±19°C, 1σ).

[41] $\Delta T^{core\text{-}rim} > 20$°C recorded in websterites DHN11 and DHX02wbt may be related to the incomplete equilibration that followed their injection and crystallization in colder peridotites. For a few peridotites T_{BKN}, T_{BM}, and T_W result in positive or negative $\Delta T^{core\text{-}rim}$ values that slightly exceed the calibration uncertainties. No correlation between T^{core} (or T^{rim}) and the sign of $\Delta T^{core\text{-}rim}$ was found in these, and thus local-scale thermal processes (e.g., minor intrusions like those producing websterites DHN11 and DHX02wbt) and/or cumulated errors are the most likely causes for such core-rim contrasts.

[42] Dominantly positive $\Delta T^{core\text{-}rim}_{Cr/Al\text{-}Opx}$ values that exceed the calibration uncertainties were obtained for several xenoliths, in agreement with the amplitude of observed Al

Table 6. Calculated Temperatures[a]

	T_{BKN}		$T_{Ca\text{-}Opx}$		T_W		T_{BM}		$T_{Cr/Al\text{-}Opx}$		
Sample	Core	Rim	Core	Rim	Core	Rim	Core	Rim	Core (m)	Core (p)	Rim
DHE01	1002	1012	1020	1014	973	984	1009	1020	969	972	953
DHE03	1081	1078	1075	1085	1023	1021	1054	1061	na	1057	1051
DHE04	986	992	975	970	940	953	977	981	950	996	964
DHE10	1091	1073	1074	1073	1037	1024	1098	1076	1009	1040	1037
DHE11	1098	1093	1083	1095	1047	1036	1087	1080	1045	1076	1066
DHE12	996	1014	1027	1047	997	1005	995	1009	948	948	929
DHE13	1077	1082	1080	1079	1018	1030	1057	1068	1063	1098	1062
DHN01	1072	1066	1083	1075	1026	1022	1078	1070	na	1086	1043
DHN05	1066	1086	1098	1104	1038	1057	1067	1095	na	1062	1055
DHN07	993	1003	991	995	951	955	987	994	972	1006	971
DHN08	1048	1044	1013	1016	985	988	1030	1024	974	997	969
DHN09	987	966	990	977	946	940	999	976	977	977	957
DHN11	851	820	953	960	891	873	886	861	866	866	833
DHN12	858	858	970	958	892	892	886	885	903	904	906
DHN16	974	965	1004	993	941	940	960	954	953	995	944
DHS02	1080	1087	1074	1085	1038	1043	1085	1091	1075	1075	1055
DHS03	1011	1011	1001	1015	961	961	997	994	996	1019	1015
DHS04	1022	1024	1018	1016	975	975	1026	1025	994	994	972
DHS05	1030	1027	994	997	960	976	1010	1012	984	994	964
DHS06	978	996	992	998	952	961	972	983	972	1018	985
DHS07	1031	1037	1021	1023	983	984	1038	1038	984	984	964
DHS08	994	982	1001	1001	956	955	1002	985	973	973	973
DHS11	986	979	1000	999	945	943	990	982	984	984	982
DHS13	1001	1004	1045	1065	978	964	1025	1012	na	1021	969
DHS14	979	960	996	995	947	928	983	960	na	975	913
DHS15	991	983	1005	1004	954	952	996	987	996	996	971
DHS16	1011	1013	1012	1007	972	971	1029	1020	na	977	969
DHS17	992	993	1017	1003	944	948	979	981	1024	1027	1002
DHS18	1032	1027	1027	1014	968	975	1020	1009	1027	1027	983
DHS20	1023	1020	1023	1014	974	967	1031	1005	991	991	983
DHS21	994	999	1009	1003	949	965	980	978	997	1065	948
DHS25	1031	1014	1017	1011	981	973	1033	1016	975	993	983
DHX02hzb	868	852	917	929	883	879	881	867	885	885	874
DHX02wbt	922	853	922	921	925	881	926	868	906	919	884
DHX03	985	973	1021	1023	949	943	970	956	1029	1037	953

[a]Core (m), matrix/fine orthopyroxene; Core (p), porphyroclastic/coarse orthopyroxene; na, not available.

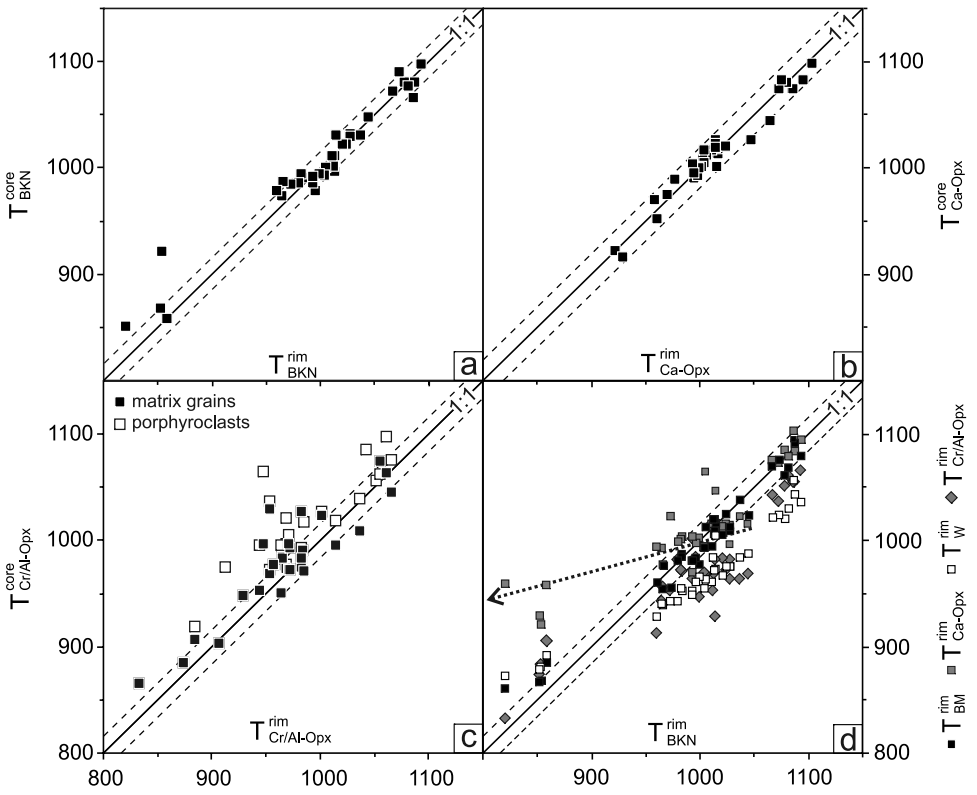

Figure 9. Geothermometry on Dish Hill xenoliths: (a–c) comparison of core and rim temperatures obtained using representative geothermometers and (d) comparison of T_{BKN} and other geothermometers using rim compositions, where the heavy dotted arrow shows the increasing difference between T_{BKN} and $T_{Ca\text{-}Opx}$ with decreasing temperature. Dashed lines in Figures 9a–9c represent calibration uncertainties; in Figure 9d the dashed lines correspond to uncertainties in T_{BKN}. All temperatures are in °C; abbreviations and details are explained in text.

zonations in many orthopyroxenes, especially porphyroclasts (Figure 9c). $T_{Cr/Al\text{-}Opx}$ suggests that several samples experienced cooling in excess of 40°C, the most significant decrease, 117°C, being recorded in orthopyroxene porphyroclasts in sample DHS21. Owing to potential diffusive annealing of zonations, these values reflect minimum cooling. The amplitude of $\Delta T^{core\text{-}rim}_{Cr/Al\text{-}Opx}$ is apparently temperature dependent. Cooling in excess of 50°C is recorded in five xenoliths, all with $T^{rim}_{Cr/Al\text{-}Opx} < 1000$°C, whereas all samples with $T^{rim}_{Cr/Al\text{-}Opx} > 1000$°C are confined to $\Delta T^{core\text{-}rim}_{Cr/Al\text{-}Opx} < 50$°C. Temperature-dependent rate of diffusive homogenization of orthopyroxene grains cannot alone produce this contrast, because differences among samples in terms of T^{rim} are too small to impose significant differences in diffusion rates, and also there is no correlation between the sizes of porphyroclasts and the temperatures they have recorded.

[43] Rim temperatures obtained by various geothermometers are compared in Figure 9d. T^{rim}_{BKN} and T^{rim}_{BM} temperatures are identical within calibration uncertainties for all but the coldest xenoliths, for which T_{BM} yields somewhat higher temperatures. T^{rim}_{W} temperatures overestimate T^{rim}_{BKN} below 900°C, and are consistently lower than T^{rim}_{BKN} above 900°C. The same trend has been obtained by *Brey and Köhler* [1990] when applying T_W to their experimental products, and has been ascribed to the inability of T_W to reproduce equilibrium temperatures in the case of chemically complex peridotitic pyroxenes. $T^{rim}_{Ca\text{-}Opx}$ temperatures are within error similar to T^{rim}_{BKN} at the hotter end of the series, while a distinct negative correlation between T^{rim}_{BKN} and the $T^{rim}_{Ca\text{-}Opx}$-T^{rim}_{BKN} difference is visible at lower temperatures. Similar correlations between $T_{Ca\text{-}Opx}$ and T_{BKN} have been observed in low-temperature xenoliths world wide (e.g., Kaapvaal craton [*Brey and Köhler*, 1990], Basin and Range and Colorado Plateau [*Smith*, 1999], and Ontong-Java Plateau [*Ishikawa et al.*, 2004]), and have been ascribed to the influence of Na on Ca incorporation in orthopyroxene. The correlation between $T^{rim}_{Cr/Al\text{-}Opx}$ and T^{rim}_{BKN} is rather poor, and $T^{rim}_{Cr/Al\text{-}Opx}$ tend to underestimate T^{rim}_{BKN} at medium and high temperatures, but overestimate them at low temperatures. Such differences are expected, since calibration of $T_{Cr/Al\text{-}Opx}$ is based on $T_{Ca\text{-}Opx}$.

[44] For the reasons discussed above, T_{BKN} appears to be the best geothermometer for Dish Hill xenoliths hotter than 950°C. Accounting for errors potentially affecting lower-temperature estimates when involving two-pyroxene equilibria, we have elected to double the uncertainties for samples with $T_{BKN} < 900$°C in order to maintain the internal consistency of results. Owing to discrepancies between $T^{rim}_{Cr/Al\text{-}Opx}$ and T^{rim}_{BKN}, and to the potential diffusive attenuation of orthopyroxene zonations, $T_{Cr/Al\text{-}Opx}$ will be

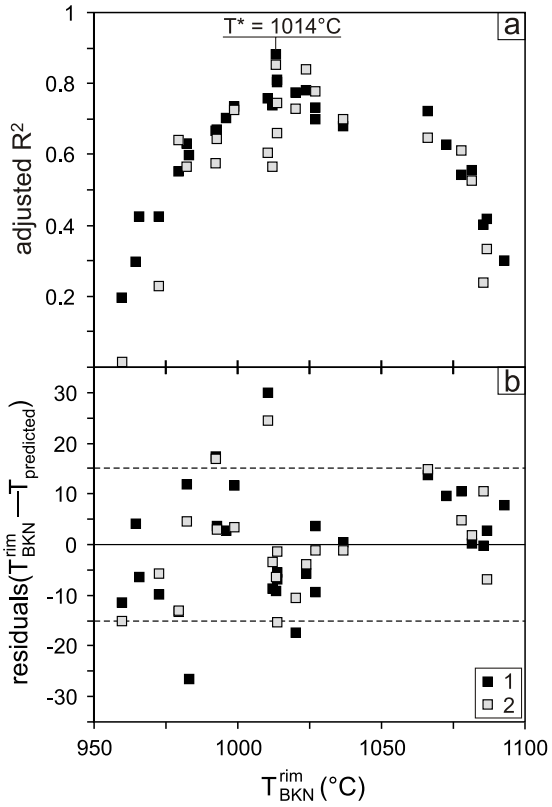

Figure 10. Temperature-composition correlation in the high-ε_{Nd} peridotite group evaluated by multiple regression analysis of temperature (T^{rim}_{BKN}) against two sets of variables. Set 1 (black squares, 28 samples) consists of olivine, clinopyroxene, Al_2O_3, MgO, NiO, CaO, and Na_2O (wt %) plus a dummy variable; set 2 (gray squares, 21 samples) consists of the same variables as in set 1 plus Sc and V (ppm). The dummy variable is introduced to distinguish samples belonging to the two temperature subgroups that result by dividing the high-ε_{Nd} peridotite group at a given T* temperature. (a) T* is varied in the 960–1093°C interval, and the corresponding adjusted R^2 value (coefficient of determination adjusted for the number of variables) of the multiple regression is calculated. The adjusted R^2 value reaches a maximum at T* = 1014°C; therefore we assume that dividing the high-ε_{Nd} peridotite group at this temperature is the most meaningful from a geological perspective, and we accordingly define two distinct temperature-composition arrays. (b) T^{rim}_{BKN} versus residuals ($T_{BKN}{}^{rim}$ minus the temperature predicted from multiple linear regression, $T_{predicted}$) in the case of group division at T* = 1014°C. In this case, the temperatures predicted by multiple regression fall within the ±15°C uncertainty range of T_{BKN} for >85% of the samples, and no systematic variations between T^{rim}_{BKN} and residuals can be observed.

taken as a qualitative indicator of temperature changes experienced by some of the xenoliths.

[45] T^{rim}_{BKN} temperatures indicate a gap of ~100°C that separates the small group of low-temperature (<860°C) low-ε_{Nd} xenoliths DHN11, DHN12 and DHX02 from the rest of the samples (>960°C), in which most analyzed clinopyroxenes display LREE depleted patterns and, to the extent of our current knowledge, belong to the high-ε_{Nd} group. Although not all studied samples were analyzed for Nd isotope composition, for simplicity we will refer to the two groups as to low-ε_{Nd} and high-ε_{Nd} xenoliths. *Johnson et al.* [1996] calculated for two LREE depleted lherzolite xenoliths from Dish Hill T_W = 893°C which, if the T_{BKN}-T_W correlation in Figure 9d is realistic, corresponds to T_{BKN} ~ 900°C. If this value represents a true equilibrium temperature, then the thermal gap in our data set may reflect a simple sampling hiatus. On the other hand, one of the three Dish Hill peridotites reported by *Smith* [2000] equilibrated at T_{BKN} = 1113°C. This suggests that the range of mantle temperatures covered by xenoliths erupted at Dish Hill may extend to somewhat higher values than that determined from the suite we studied.

4.7. Temperature-Composition Relationships in High-ε_{Nd} Peridotites From Dish Hill

[46] High-ε_{Nd} peridotites display a distinct correlation between their composition and equilibrium temperature. Multiple regression analysis based on whole-rock chemical compositions, mineral modes and T^{rim}_{BKN} temperatures indicates that these xenoliths define two distinct temperature-composition arrays (Figure 10). We distinguish the medium-temperature array defined by samples equilibrated in the 960–1014°C range from the high-temperature array that includes xenoliths equilibrated in the 1014–1093°C range (Figure 11). In both arrays, composition trends expressed as variations in mineral modes and whole-rock major and trace element abundances show correlations with temperature: the hotter extremes of the two arrays are defined by harzburgites, and the lower temperatures are associated with increases in clinopyroxene mode and decreases in olivine modes (orthopyroxene modes varies systematically with temperature in the medium-temperature array but not in the high-temperature array). Major and trace elements follow the same trend in accordance with their preference for olivine or clinopyroxene: in both arrays MgO and Ni decrease, whereas CaO, Al_2O_3, Na_2O, TiO_2, Sc, V, Y, and HREEs increase from the hotter toward the colder end. Notably, whole-rock compositions reconstructed from mineral compositions and modes fit well into these arrays. Excluding a few samples that equilibrated around 1014°C, the temperature-composition gap separating the two arrays is larger than the uncertainties associated with T_{BKN}. Substituting T^{rim}_{BKN} by T^{core}_{BKN} (not shown) alters somewhat the quality of temperature-composition correlations, but maintains the distinction between the two arrays, as well as the above described trends within the individual arrays.

[47] The correlation between temperature and Nd isotopic composition of clinopyroxenes is insignificant at the scale of individual arrays, but at the scale of the whole group of high-ε_{Nd} xenoliths hotter samples tend to have lower ε_{Nd}.

4.8. Depths of Xenolith Entrainment

[48] There are no reliable geobarometers constraining equilibrium pressure for spinel peridotites, thus our approach for the Dish Hill xenoliths is to define bounds on their entrainment depths. At first order, the maximum stability of spinel in the absence of garnet [*O'Neill*, 1981] and the lithosphere-asthenosphere boundary beneath the

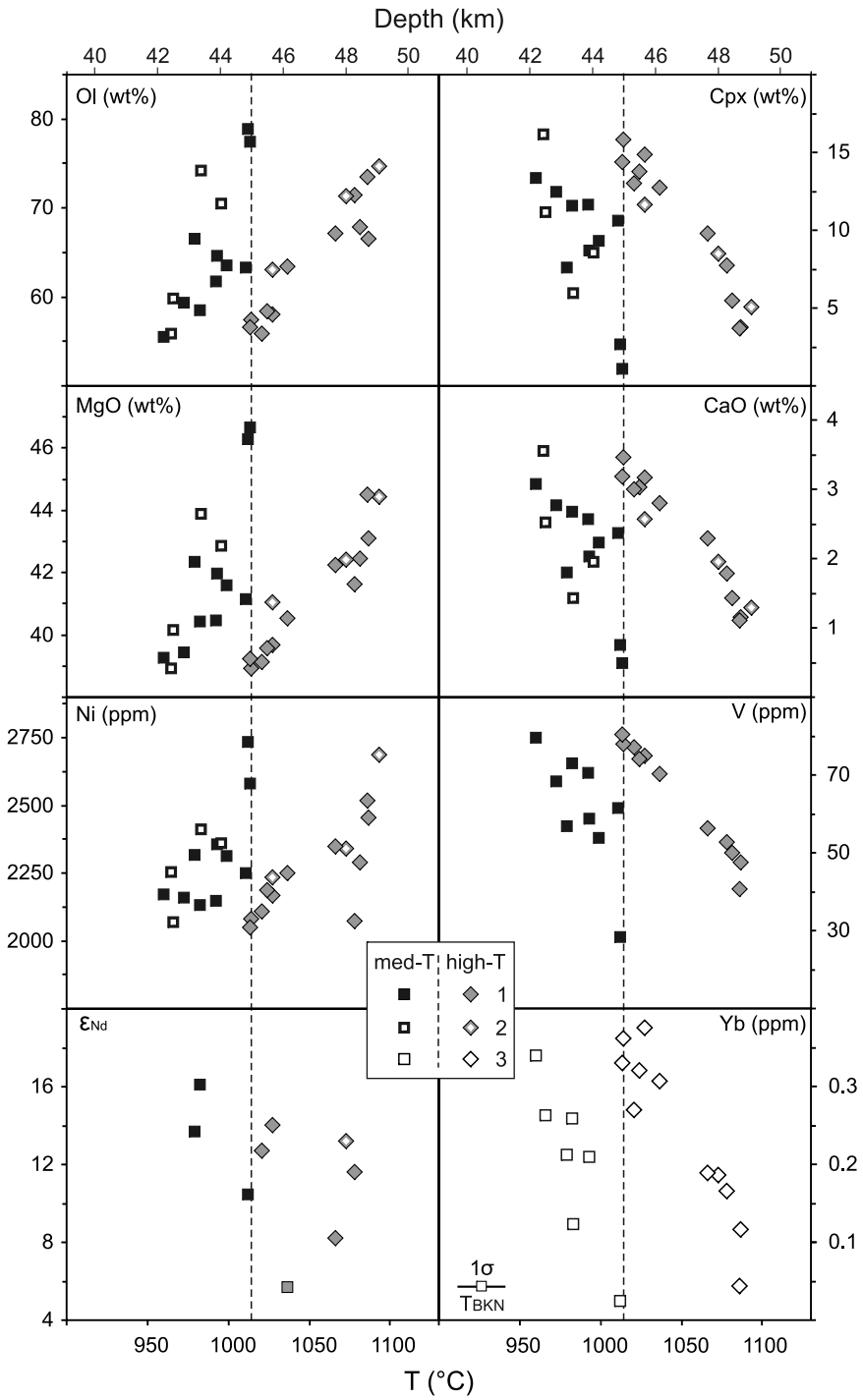

Figure 11. T_{BKN} versus whole-rock compositions in high-ε_{Nd} peridotites. Xenolith entrainment depths correspond to a 95 mW/m^2 geotherm (details in text and Figure 12). Squares show medium-T array, and diamonds show high-T array. 1, XRF analyses, mineral modes calculated by the least squares method; 2, reconstructed from mineral compositions and modes from point counting; 3, reconstructed from Cpx(Yb) and mineral modes, following *Witt-Eickschen and O'Neill* [2005].

central Mojave [*Li et al.*, 2007] limit the maximum equilibration depths of the samples to 50–70 km. Minimum depths are constrained by the depth of Moho [*Das and Nolet*, 1998; *Yan and Clayton*, 2007] and the spinel-plagioclase transition [*Green and Ringwood*, 1970] to ~30 km (Figure 12).

[49] These depth constraints can be further refined by projecting the xenolith temperatures onto steady state model geotherms that are based on measured surface heat flow and reasonable estimates of crustal heat production and mantle heat flux. We are aware of all the uncertainties associated with assuming steady state conduction if the lithospheric

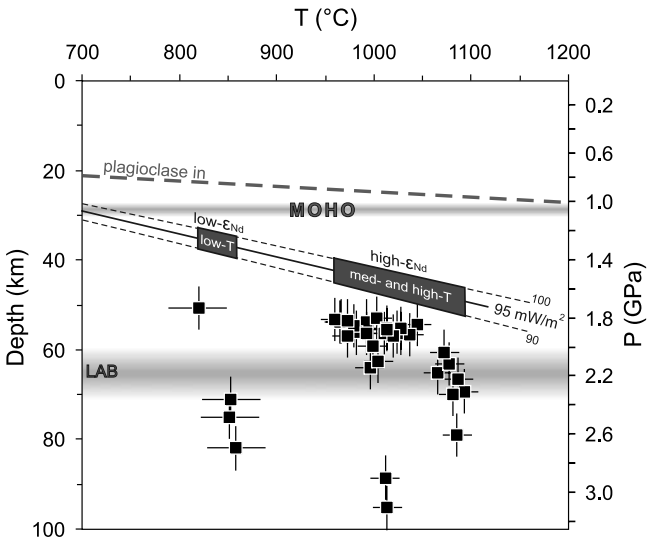

Figure 12. Entrainment depths of xenoliths from Dish Hill constrained by geothermometry, phase assemblages, and surface heat flow data. Black squares indicate maximum pressures of stability of individual xenolith assemblages constrained by Cr contents in spinel in the absence of garnet, at T_{BKN}; associated error bars are 0.15 GPa [*O'Neill*, 1981] and 15°C and 30°C for the high-ε_{Nd} and low-ε_{Nd} samples, respectively. Minimum pressures are constrained by the plagioclase/spinel transition in lherzolites [*Green and Ringwood*, 1970]. Continental conductive geotherms corresponding to 95 ± 5 mW/m^2 surface heat flows assumed for Dish Hill were calculated applying the approach of *Turcotte and Schubert* [2002, equation 4–31] for mantle heat fluxes of 57 ± 3 mW/m^2, an exponentially decreasing heat production with depth (using an average characteristic length scale of 13 km) and thermal conductivity of 3 W/mK; applying the approach of *Pollack and Chapman* [1977] yields similar results. Boxes labeled as "low-T" and "med- and high-T" represent entrainment conditions resulting for low-ε_{Nd} and high-ε_{Nd} samples, respectively. Depth of Moho beneath the central Mojave is 27–29 km [*Das and Nolet*, 1998; *Yan and Clayton*, 2007]; lithosphere-asthenosphere boundary (LAB) is at 60–70 km [*Li et al.*, 2007]. Densities of 2.75 g/cm^3 for crust and 3.30 g/cm^3 for mantle were used for depth-pressure conversion. Further details are given in text.

thermal state is transient, as could be the case in Cenozoic western North America. For example, transient cases represented by inverted geotherms, such as might have been imparted during flat subduction of the Farallon plate during the Laramide [*Dumitru et al.*, 1991], would severely complicate any projections. However, simple back-of-the-envelope calculations on thermal relaxation times indicate that this early Tertiary temperature inversion would have been erased by Miocene times, since hot, young oceanic lithosphere was being subducted in the late Laramide. Transient cases involving heating could also be problematic. For example, asthenospheric upwelling in response to the post-Laramide removal of the Farallon slab [e.g., *Humphreys*, 1995] in mid-Tertiary times could have heated the base of the lithosphere. However, such heating anomaly would have dissipated within 5–10 Ma after the process ceased. It is also important to note that probably no significant magma-induced perturbation of the surface heat flow preceded or accompanied the volcanic eruption at Dish Hill: as discussed above, most of the xenoliths do not record temperature variations, or record cooling that cannot be related to basaltic magmatism; temperature increase is recorded in few samples only. For these reasons, we will use present-day heat flow in the Mojave Desert to approximate lithospheric geotherms.

[50] A large surface heat flow data set from western United States [*Lachenbruch et al.*, 1978, 1985; *Sass et al.*, 1994] indicates a relatively uniform heat flow of 65–75 mW/m^2 over most of the central and western Mojave, whereas a rapid increase to more than 100 mW/m^2 may be observed eastward from the Granite Mountain fault [*Dokka*, 1983], the southward extension of the Death Valley fault zone. Simple thermal modeling suggests that the rate of migration of the isothermal surfaces induced by conductive cooling in the Mojave lithospheric mantle is less than ±0.5 km/Ma and thus, similar heat fluxes must have been characteristic for the Mojave Desert during the late Pliocene–early Pleistocene entrainment event, as well. A surface heat flow of 95 (±5) mW/m^2 may be considered representative for Dish Hill located at the boundary between the above mentioned high- and low-heat-flux domains; this value is similar to the average heat flow of the Basin and Range province [*Roy et al.*, 1968; *Sass et al.*, 1971, 1994].

[51] Assuming the xenoliths from Dish Hill originated on a 95 (±5) mW/m^2 geotherm, temperature projections imply they represent a ~15 km thick mantle slice ranging between ~35 and ~50 km in depth. The 90 mW/m^2 geotherm represents the lowest gradient at which the entire xenolith suite would safely avoid stabilization of garnet (Figure 12); an 85 mW/m^2 geotherm would significantly increase the chance of garnet bearing peridotites to occur at Dish Hill. On the other hand, a geotherm much hotter than 100 mW/m^2 is unlikely, too, because it would result in unreasonable crustal level equilibration depths of the shallowest peridotites and, in addition, would represent a transient positive thermal anomaly in the regional context that would be recorded as "prograde" zonations in orthopyroxenes. Hence, probably no more than ±5 km uncertainty should be associated to the estimated 15 km thickness of the mantle slice sampled by xenoliths. Within this slice, the colder, low-ε_{Nd} xenoliths would represent the shallow 35–38 km depth interval, whereas the hotter pieces, the high-ε_{Nd} group, would compose the bottom 42–50 km.

[52] T_{BKN} temperatures for Cima peridotite xenoliths scatter in the 911–1055°C range (supplementary data set of *Smith* [2000]). Assuming that the eastward increase of surface heat flow [*Sass et al.*, 1994] mainly reflects differences in crustal heat production, and that the regional mantle heat flow at the Moho is roughly constant, these temperatures would imply that the maximum extraction depths of xenoliths from Cima and Dish Hill were within error similar. Alternatively, if surface heat flow variations reflect differences at the Moho, then Cima xenoliths might have originated from a 10–15 mW/m^2 hotter geotherm and,

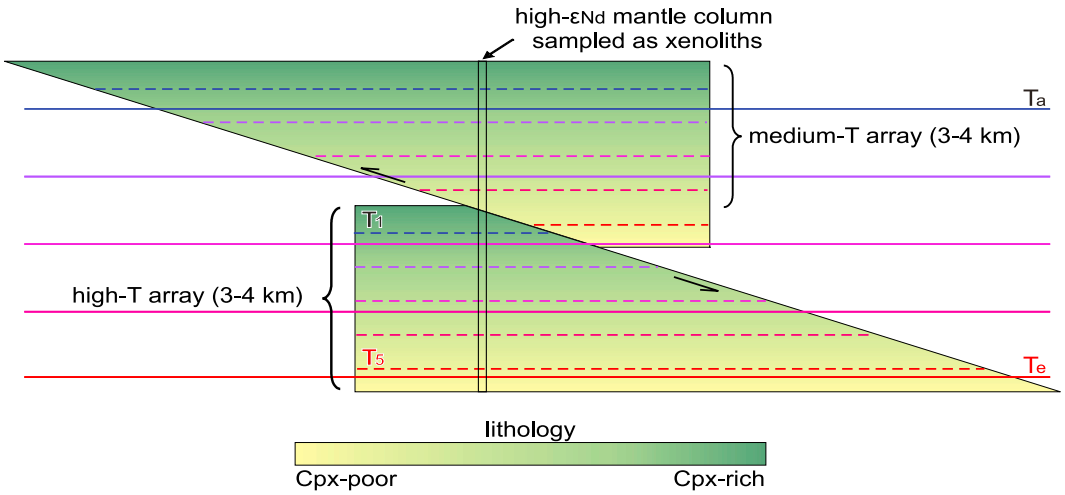

Figure 13. Diagram illustrating the envisaged mechanism responsible for the mantle lithostratigraphy reconstructed from temperature-composition trends identified in high-ε_{Nd} peridotite xenoliths. Initially a ~4 km thick mantle layer grading from harzburgites in the bottom to clinopyroxene-rich lherzolites in the top equilibrated along a geotherm marked by isotherms T_1-T_5 (dashed lines). Subsequent tectonic imbrication and thermal relaxation led to the superposition of the observed medium-T and high-T arrays, where T_{BKN} temperatures reflect the new thermal gradient marked by isotherms T_a-T_e. High $T_{Cr/Al\text{-}opx}$ temperatures recorded in orthopyroxene porphyroclast cores from the cooled medium-T array represent relics of the preimbrication geotherm.

accordingly, from 8 to 10 km shallower depths than the high-ε_{Nd} samples from Dish Hill.

5. Discussion

5.1. Late Pliocene–Early Pleistocene Shallow Mantle Lithostratigraphy Beneath Dish Hill

[53] Xenolith compositions in combination with estimated extraction depths reveal a complex vertical layering in the shallow mantle lithosphere beneath Dish Hill, which indicates a strong relationship between large-scale geochemical and tectonic processes.

5.1.1. Discontinuity Between Low-Nd and High-Nd Isotopic Domains (D1)

[54] Nd isotope ratios and trace element patterns in clinopyroxenes indicate a sharp compositional discontinuity somewhere in the unsampled 37–42 km depth range, which separates a shallower, relatively enriched domain represented by the colder low-ε_{Nd} harzburgites DHN12 and DHX02hzb, and a deeper, relatively depleted domain consisting of hotter high-ε_{Nd} peridotites (Figure 12). We address here possible origins of the observed isotopic contrast.

[55] One possibility is that the low-ε_{Nd} harzburgites are not representative of the shallow mantle, but rather are small-scale metasomatized domains in contact with very low-ε_{Nd} mafic veins intruded into a high-ε_{Nd} lithospheric mantle. Such an interpretation is unrealistic as long as no shallow high-ε_{Nd} peridotites have been found, and mafic xenoliths in the region have high-ε_{Nd} (DHN11 from Dish Hill and xenoliths from Cima, described by *Nielson et al.* [1993], *Leventhal et al.* [1995], and *Mukasa and Wilshire* [1997]); contamination by such veins tends to raise the Nd isotopic ratios in low-ε_{Nd} harzburgites, as suggested by host-vein relationships in composite xenolith DHX02. The second possibility is that the high-ε_{Nd} peridotites resulted from the influx of LREE-depleted mafic liquids with highly radiogenic Nd isotopic signature into low-ε_{Nd} harzburgites, which now are preserved as relics in the shallowest mantle. Such an interpretation is at odds with the observation that most depleted samples of the medium- and high-temperature arrays have the lowest Nd isotopic ratios, because harzburgitic clinopyroxenes, owing to their low modes and Nd concentrations, are significantly more susceptible to metasomatism than clinopyroxenes in fertile peridotites. The third possibility is that the low-ε_{Nd} signatures of the shallow harzburgites are the result of a series of events which, as discussed in section 4.5, likely included pervasive metasomatic overprinting by fluids or melts derived from an underlying enriched source (e.g., a subducted altered oceanic plate, ancient or Farallon), partial melting, and limited input of mafic liquids. This scenario implies that the high-ε_{Nd} peridotites, which make up the underlying mantle, must have been emplaced after the pervasive metasomatic event, because otherwise it seems unlikely that they could have entirely avoided contamination by LREE-enriched nonradiogenic Nd component. High-ε_{Nd} clinopyroxenes display rather uniform REE patterns, and do not show any correlation between REE and Nd isotopic enrichments that could be linked to the pronounced LREE enrichment observed in shallow low-ε_{Nd} harzburgite DHN12.

[56] On the basis of the foregoing discussion, we conclude that the Nd isotopic discontinuity identified in the mantle beneath Dish Hill resulted from the tectonic juxtaposition of two isotopically contrasting mantle domains. Henceforth, we shall refer to the discontinuity between these domains as D1.

5.1.2. Discontinuity Within the High-Nd Isotopic Domain (D2)

[57] The medium- and high-temperature arrays defined by high-ε_{Nd} xenoliths correspond to two superposed, yet sim-

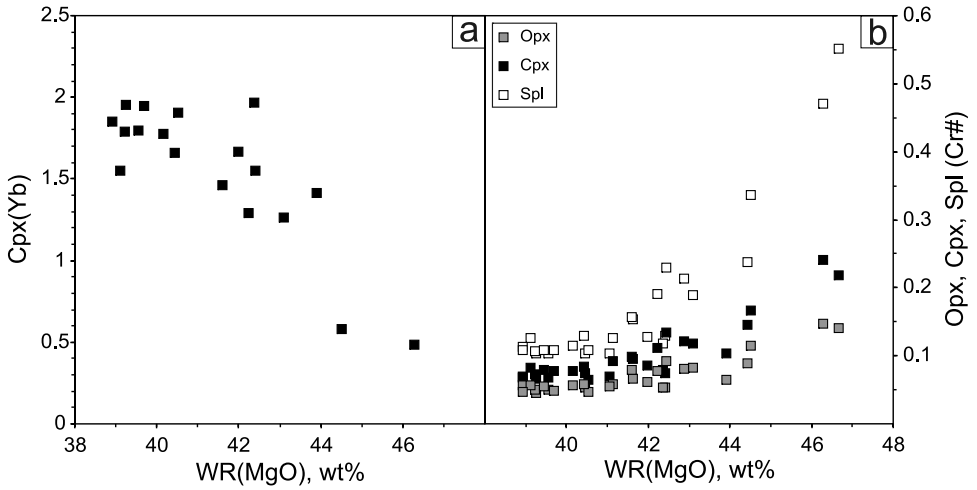

Figure 14. Covariation of whole-rock MgO in high-ε_{Nd} peridotite xenoliths from Dish Hill (a) with Yb concentration in clinopyroxenes and (b) with Cr # in orthopyroxene (Opx), clinopyroxene (Cpx), and spinel (Spl).

ilar mantle sequences, which together represent a ~7 km thick vertical section (~3 and ~4 km, in accordance with the temperature intervals encompassed by the two arrays) located somewhere in the 42–50 km depth interval within the relatively depleted domain (Figures 11 and 12). The broad compositional range covered by the two temperature-composition arrays, their similar compositional trends, and the presence of a sharp contact between harzburgites and clinopyroxene-rich lherzolites at ~45 km (i.e., ~1014°C) suggest that the superposition of the two sequences represents a tectonic duplex resulting from imbrication. In this context it is conceivable that, as suggested by $T^{core}_{Cr/Al\text{-}Opx}$, the high-Al orthopyroxene cores observed in xenoliths from the medium-temperature array preserve a record of higher thermal equilibration prior to imbrication and cooling; this is because Al in pyroxene diffuses much slower than Ca and thus cooled orthopyroxenes more readily preserve relict high $T_{Cr/Al\text{-}opx}$ temperatures (Figure 13). Whether such imbrication extends above and below the two superposed sequences recognized here, and whether it is representative of the sub-Mojave lithospheric mantle at larger scales, remains an open question. This discontinuity is here referred to as D2.

[58] The recognition of tectonic imbrication in the high-ε_{Nd} mantle domain implies that all mineralogical and chemical components defining the upward enriched trends in the two arrays were inherited from a preimbrication state. In this respect, the robustness of temperature-composition correlation in the two arrays is somewhat surprising because it suggests that the metasomatic processes affecting the lithosphere beneath Dish Hill [*Wilshire et al.*, 1980; *Menzies et al.*, 1985; *Nielson et al.*, 1993; *Johnson et al.*, 1996] acted only at the local scale, in the close proximity of veins, and were not strong enough to disturb the compositional layering recognized in the high-ε_{Nd} mantle domain.

5.2. Petrogenetic Origin of the High-ε_{Nd} Sub-Mojave Mantle Lithosphere

[59] As discussed above, the high-ε_{Nd} and low-ε_{Nd} mantle domains must have been juxtaposed along D1 after each domain had evolved into their distinctive geochemical signatures. If this feature is a regional feature of the central Mojave lithosphere rather than a peculiar local anomaly, then large-scale transport must be considered in order to explain the juxtaposition between the shallower low-ε_{Nd} and deeper high-ε_{Nd} Mojave mantle. This section explores possible origins of the high-ε_{Nd} lithospheric mantle. Hypotheses include (1) decompression-induced melt depletion of the sub-Mojave asthenospheric mantle at depth, followed by cooling and underplating of the resulting mantle residuum to the base of the overriding continental lithosphere, (2) in situ melt depletion of the deeper lithospheric mantle due to an isobaric heating event, and (3) shallow pressure melt depletion followed by underthrusting of such mantle residua to deeper depths to form the present-day Mojavian lithosphere.

[60] The first scenario relies on the idea that upwelling and adiabatic melting of the subcontinental asthenosphere beneath the Mojave occurred as a consequence of the post-Laramide removal of the flat-lying Farallon slab via roll-back [*Saleeby*, 2003] and/or slab window opening after that the East Pacific Rise reached western North America in the early Miocene [*Dickinson and Snyder*, 1979; *Severinghaus and Atwater*, 1990; *Dickinson*, 1997; *Wilson et al.*, 2005]. In this scenario the Farallon plate has been stripped away from beneath the Mojave Desert at ~40 km depth, so that the D1 discontinuity corresponds to the contact between a shallower and older low-ε_{Nd} mantle (whose isotopic signatures suggest a common history with the overlying ancient continental crust) and a deeper high-ε_{Nd} mantle that resulted from melt depletion and cooling of the underplated and isotopically depleted asthenosphere. In the second scenario, removal of the Farallon slab occurred just beneath the high-ε_{Nd} lithospheric mantle, and the xenolith compositions reflect isobaric melting and/or melt reenrichment caused by the heating associated with upwelling asthenosphere that impinged against the base of the continental lithosphere. Finally, the third scenario implies that the high-ε_{Nd} lithospheric mantle has been depleted in a different geological setting, and then underthrusted along D1. As we discuss in section 5.2.1, the xenolith-based mantle structure and re-

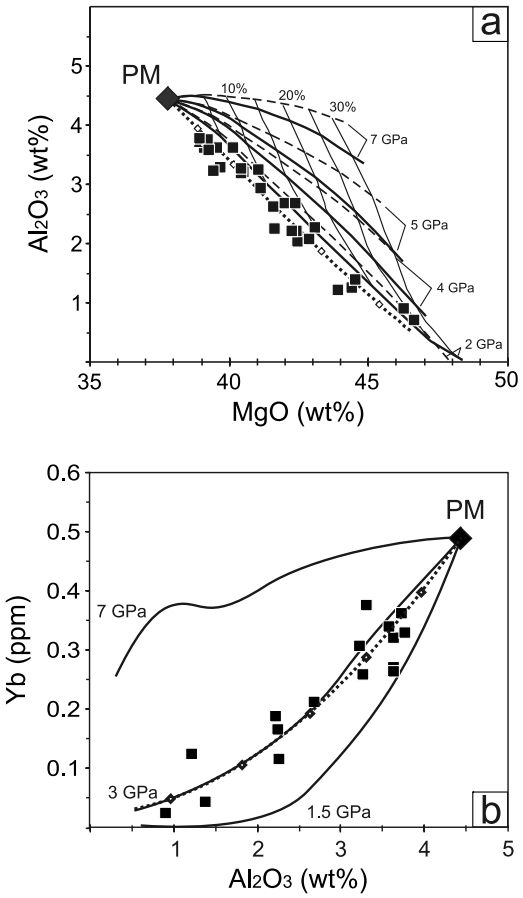

Figure 15. Constraints on partial melting pressures of high-ε_{Nd} Dish Hill peridotites (black squares) from covariation of (a) Al_2O_3 and MgO and (b) Al_2O_3 and Yb, assuming near-fractional melting (1% melt porosity) and a primitive mantle source [*Sun and McDonough*, 1989]. In Figure 15a, heavy solid and dashed lines correspond to compositions of residua formed by progressive melting via adiabatic decompression and isobaric heating, respectively, starting at various pressures, as labeled; light solid lines mark melting degrees, F (%). These calculations are based on the parameterization of *Walter* [1999] and yield results that are essentially identical to those given by *Herzberg* [2004]. In Figure 15b, solid lines indicate isobaric fractional melting paths at different pressures as labeled, according to *Canil* [2004]. Dotted lines in Figures 15a and 15b correspond to residua of adiabatic melting starting at 2.5 GPa as resulting from Adiabat_1ph [*Smith and Asimow*, 2005] running with pMELTS thermodynamic database [*Ghiorso et al.*, 2002], mineral-melt partition coefficients from *Niu and Hékinian* [1997], and fayalite-magnetite-quartz oxygen buffer. Diamonds indicate F(%) = 5, 10, 15, 20, and 25.

gional geology constraints, in combination with estimated melting conditions and depletion degrees of the high-ε_{Nd} samples, reveal that these scenarios are not equally likely.

5.2.1. Constraints From Mantle Structure and Regional Geology

[61] As shown above, the recurrent compositional trend recognized in the high-ε_{Nd} mantle beneath Dish Hill was achieved most likely by tectonic shortening, that is, imbrication along D2. Such an interpretation is key to further constraining the origin of the Mojave lithospheric mantle because the central Mojave did not experience tectonic shortening during the late-Cenozoic (the East California Shear Zone has no thrust component [*Hardebeck and Hauksson*, 2001]), and thus the inferred imbrication must have predated the late- and post-Laramide regional extension [*Saleeby*, 2003]. This implies that D2 might have formed either in the compressional regime imposed by underthrusting Farallon slab during the Laramide or in an earlier shortening episode. Consequently, the preimbrication compositional trends in the high-ε_{Nd} domain are very likely pre-Tertiary and thus, cannot be related in any way to decompression melting of the subcontinental asthenosphere beneath the Mojave triggered by removal of the Farallon slab.

5.2.2. Constraints From Melting Conditions and Depletion Degree of Mantle Source

[62] High-ε_{Nd} peridotite xenoliths from Dish Hill range from primitive mantle-like fertile lherzolites to depleted harzburgites, and their bulk composition (except for Na_2O and TiO_2 which, in spite of their incompatibility, show linear correlation with MgO) closely follow the spinel facies melt-depletion trends predicted by experiments [*Walter*, 2003; *Herzberg*, 2004] and recognized in world-wide spinel peridotites (Figures 7 and 8). The decrease of HREE concentrations in clinopyroxene and increase of Cr # in clinopyroxene, orthopyroxene, and spinel with whole-rock MgO (Figure 14*)* are also suggestive of progressive melt removal. However, a series of post melt-depletion modification processes like metamorphic differentiation [*Palme and O'Neill*, 2003; *Ionov*, 2004], mingling with pyroxenites [*Bodinier and Godard*, 2003; *van Acken et al.*, 2008, and references therein], and porous melt infiltration [*Elthon*, 1992; *Le Roux et al.*, 2007; *van Acken et al.*, 2008, and references therein] may also produce similar compositional trends and, in addition, explain the linear MgO-TiO_2 and MgO-Na_2O trends observed here and in many other peridotite suites. We discuss these possibilities in turn below.

[63] Metamorphic differentiation is thought to have effects at limited length scales and, thus, has probably negligible contribution to the kilometer-scale continuous compositional trends identified in the lithospheric mantle beneath Dish Hill. The other two modification mechanisms imply refertilization, as they require net input of mafic material, and may represent, either alone or in combination, viable explanations for these trends. We note that advanced equilibration between residual peridotite and added mafic component may imply the obliteration of textural evidence of refertilization mechanisms. In such cases, mingling of mafic veins and depleted peridotites under high strain may result in fertile peridotites that are indistinguishable at all scales from those formed by enrichment of depleted peridotites by basaltic liquids via porous flow. In any of these cases, the composition of high-ε_{Nd} nodules would indicate an apparent depletion corresponding to their minimum degree of melting before refertilization. As we discuss below, the minimum depletion experienced by these peridotites, and in particular harzburgites, is crucial to understanding the origin of their mantle source.

[64] There are several ways in which the physical conditions and degree of melting experienced by peridotites can

Table 7. Melting Degrees From Whole-Rock Al_2O_3, MgO, and Yb Contents, Calculated by Various Approaches[a]

	Niu [1997], -dF/dP = 1.25%		*Walter* [1999], -dF/dP = 1.25%		Adiabat_1ph/pMELTS, -dF/dP Variable		
Sample	F_{Al2O3} (%)	F_{MgO} (%)	F_{Al2O3} (%)	F_{MgO} (%)	F_{Al2O3} (%)	F_{MgO} (%)	F_{Yb} (%)
DHE01	24.0	26.5	22.9	23.7	25.2	26.9	27.1
DHE03	13.5	12.6	15.6	11.1	17.4	14.9	16.3
DHE04	7.2	8.9	9.6	7.8	11.1	11.1	na
DHE10	13.7	15.2	15.8	13.4	17.6	17.3	15.1
DHE11	21.1	21.2	21.1	18.9	23.2	22.6	na
DHE12	25.9	27.6	23.9	24.6	26.4	27.8	na
DHE13	15.0	15.2	16.9	13.5	18.7	17.4	na
DHN01	13.7	14.6	15.8	12.9	17.6	16.8	15.0
DHN05	20.1	21.5	20.5	19.1	22.5	22.8	25.3
DHN09	4.6	7.9	6.6	6.9	7.7	10.0	11.1
DHN16	3.8	3.9	5.6	3.2	6.4	5.2	na
DHS02	13.4	17.2	15.5	15.3	17.3	19.2	19.6
DHS03	8.8	11.2	11.3	9.8	12.8	13.4	na
DHS04	4.6	6.0	6.7	5.1	7.7	7.8	8.4
DHS05	6.6	6.4	8.9	5.5	10.3	8.3	5.9
DHS06	14.7	16.6	16.6	14.7	18.4	18.6	na
DHS07	7.0	9.2	9.5	8.0	10.9	11.4	9.1
DHS08	6.8	8.9	9.2	7.7	10.5	11.0	11.4
DHS11	10.5	15.0	13.0	13.3	14.6	17.2	13.7
DHS14	4.9	5.0	7.0	4.2	8.1	6.5	7.6
DHS15	21.4	19.7	21.3	17.5	23.4	21.3	19.0
DHS16	3.8	4.9	5.7	4.1	6.5	6.4	8.0
DHS17	10.5	13.8	13.0	12.2	14.6	16.1	13.8
DHS18	6.9	10.8	9.3	9.5	10.7	13.1	na
DHS20	4.6	4.5	6.7	3.8	7.7	6.0	10.8
DHS21	10.9	12.6	13.3	11.1	15.0	14.9	na
DHS25	4.1	3.9	6.0	3.2	6.9	5.2	6.5
DHX03	6.9	5.6	9.3	4.7	10.7	7.2	na

[a]Here na, data not available.

be assessed, and ideally these yield identical results. For example, over a broad range of physical conditions and melting mechanisms, partial fusion produces peridotite residua progressively enriched in Mg and depleted in Al and Yb, and the covariation paths of these elements are sensitive to the pressure of melting [*Walter*, 2003; *Canil*, 2004; *Herzberg*, 2004]. Assuming a dry primitive mantle source [*McDonough and Sun*, 1995], we constrained the maximum pressure of fusion and estimated the extent of melt depletion of Dish Hill peridotites using their whole-rock MgO, Al_2O_3 (Tables 4a–4d), and reconstructed Yb contents (Table 5). The advantage of this approach is that major elements, such as MgO, Al_2O_3, and moderately incompatible trace elements as Yb, are sensitive to the extent of melting, but are not easily influenced by small-scale metasomatic processes and alterations. One caveat is that representative bulk rock compositions are difficult to obtain in coarse-grained small xenoliths because the mode of some phases could be overestimated or underestimated. Therefore, in some cases Al_2O_3 and/or Yb contents can be underestimated, and thus melt depletion overestimated, such as in sample DHS15 for which the bulk composition has been recalculated from mineral compositions and modes. This sample lacks visible primary spinel grains (a tiny melt pocket with micron-size secondary euhedral Mg-chromite inclusions has been counted as decomposed spinel), and therefore its Al_2O_3 content may be underestimated. However, given the nearly harzburgitic composition of this sample, the spinel it contains must be relatively Cr-rich, and therefore the amplitude of Al_2O_3 underestimation is probably acceptable for our purpose. All the other samples are large and/or fine grained enough to meet the homogeneity criteria.

[65] In order to limit the model dependency of results we applied several different approaches: the parameterizations of *Niu* [1997], *Walter* [1999], and *Canil* [2004], as well as the Adiabat_1ph software [*Smith and Asimow*, 2005] running with the pMELTS thermodynamic database [*Ghiorso et al.*, 2002] and mineral-melt REE partition coefficients of *Niu and Hékinian* [1997]. All calculations were performed assuming a near-fractional melting regime with 1% melt porosity, simulated as a combination of incremental batch melting and melt removal.

[66] Pressure-dependent covariations of MgO with Al_2O_3, and Yb with Al_2O_3 during partial melting strongly suggest that high-ε_{Nd} Dish Hill peridotites most likely experienced partial melting at pressures that did not exceed 3GPa (Figure 15). This implies that garnet, if ever present in the high-ε_{Nd} mantle lithosphere beneath Dish Hill, melted out early and did not play a role in controlling the composition of the residua. Such a conclusion is consistent with the essentially flat chondrite-normalized MREE-HREE patterns observed in clinopyroxenes (Figure 2). Isobaric melting and adiabatic decompression melting produce residua with very similar MgO-Al_2O_3 trends at low pressures, therefore these melting paths are practically undistinguishable (Figure 15a).

[67] We calculated the extent of melt depletion of Dish Hill peridotites assuming an adiabatic near-fractional melting path starting at 2.5 GPa, which corresponds to a mantle potential temperature of 1390°C. Results are presented in Table 7. The MgO, Al_2O_3, and Yb contents in peridotites yield reasonably similar degrees of melt depletion for all samples including DHS15 (Figure 16). The results of the fundamentally different approaches are similar, in particular at the inferred minimum and maximum melting degrees.

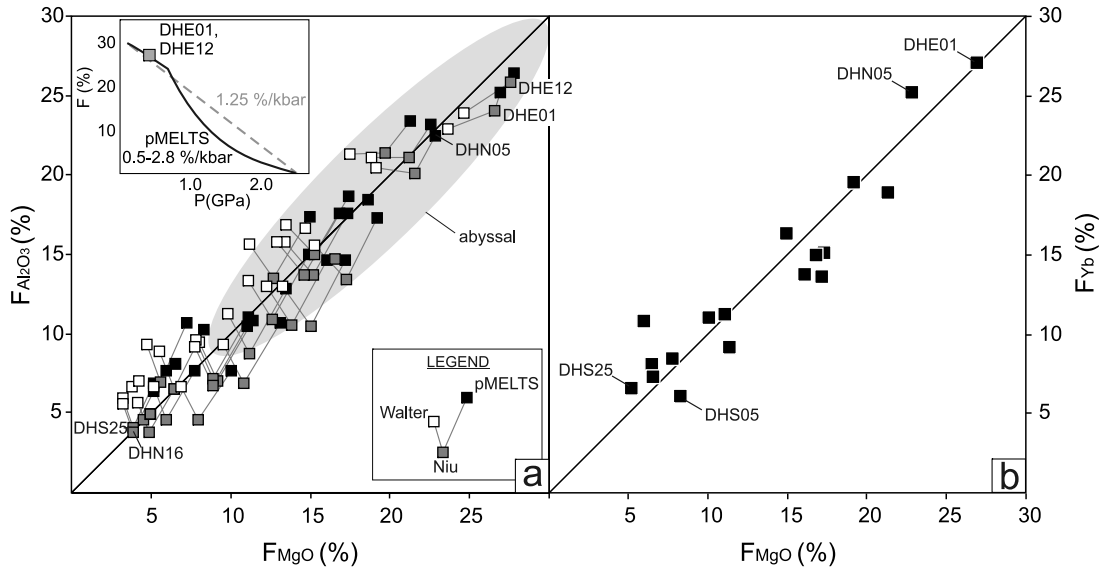

Figure 16. Melting degrees F(%) of high-ε_{Nd} peridotites from Dish Hill corresponding to their MgO, Al_2O_3, and Yb contents, assuming mantle source, melting regime, and path as in Figure 15. (a) $F_{MgO(\%)}$ versus $F_{Al2O3(\%)}$ calculated by the approaches of *Niu* [1997], *Walter* [1999], and Adiabat_1ph. (b) $F_{MgO(\%)}$ versus $F_{Yb(\%)}$ resulting from Adiabat_1ph and mineral-melt REE partition coefficients from *Niu and Hékinian* [1997]. Most fertile and most depleted samples are labeled for reference. The parameterizations of *Niu* [1997] and *Walter* [1999] were used assuming a constant rate of fractional melting of 1.25% per kbar; calculations with Adiabat_1ph implied variable melting rates (0.5–2.8% per kbar). Melting degrees for individual samples were obtained by reverting their MgO, Al_2O_3, and Yb contents to F(%) resulting from the different approaches. In Figure 16a, light lines link symbols corresponding to melting degrees obtained for each sample by the different methods, the gray field outlines the range obtained for abyssal peridotites (compositions taken from the same references as those in Figure 7), and inset plot shows the increase of F(%) with decreasing pressure, according to the different melting models. Most depleted samples DHE12 and DHE01 (gray square in inset plot) require 25–28% partial melting and decompression of 2–2.1 GPa, regardless of the adopted model.

Results indicate that most fertile lherzolites underwent minimum 3–6% melting, whereas most depleted harzburgites experienced as much as 25–28% liquid removal. The total amount of decompression required for the depletion observed in the most refractory harzburgites DHE12 and DHE01 is 2–2.2 GPa, regardless of whether using Walter's and Niu's parameterizations [*Walter*, 1999; *Niu*, 1997] with an imposed constant melting rate of 1.25% per kbar (the average of values used by *Klein and Langmuir* [1987] and *McKenzie and Bickle* [1988]), or running Adiabat_1ph with reaction-dependent variable melting rates of 0.5–2.8% per kbar as constrained by pMELTS. If a depleted MORB mantle model (DMM) [*Workman and Hart*, 2005] had been used instead of the chosen primitive mantle source, the most depleted samples would require slightly less, 22–25% melting, whereas the most fertile peridotites of the high-ε_{Nd} suite would imply no melting at all, since they are as fertile as DMM.

5.3. The Preferred Model: Underthrusted Farallon Plate

[68] The above formulated constraints and arguments indicate that the Mojave lithosphere gained its structure not later than in the late-Laramide. As we discuss below, the high degrees of melting experienced by the Dish Hill xenoliths strongly suggest that melting of the sub-Mojave asthenosphere cannot account for the majority of high-ε_{Nd} Dish Hill peridotites.

[69] As argued above, at least 2 GPa adiabatic decompression is necessary to form the most depleted Dish Hill harzburgites by near-fractional melting. Therefore, in order to obtain 25% melt depletion before reaching discontinuity D1 at ~40 km depth, fusion should commence at >105 km depth. This would require an elevated mantle potential temperature of ~1480°C that is not justified in the Mojave Desert and surrounding areas [*Bradshaw et al.*, 1993; *Lee et al.*, 2009]. Assuming a more reasonable mantle potential temperature (~1390°C), our pMELTS calculations indicate that melting starts at ~75 km and produces not more than 8% melting before it reaches the base of a 40 km thick lithosphere (inset in Figure 16a). Even if we had allowed for a more generous constant melting rate of 1.25% per kbar, not more than 14% melting would be achieved. This line of argument also rules out high-degree melting by isobaric heating, as such a process would also require anomalously high potential temperatures. Collectively, these petrologic constraints and arguments lead us to conclude that the high-ε_{Nd} peridotites represent underthrusted segments rather than being formed at great depth. The question now is whether these underthrusted mantle segments represent slivers of subduction-modified Cordilleran continental lithospheric mantle dragged northeastward by the flat-subducting Far-

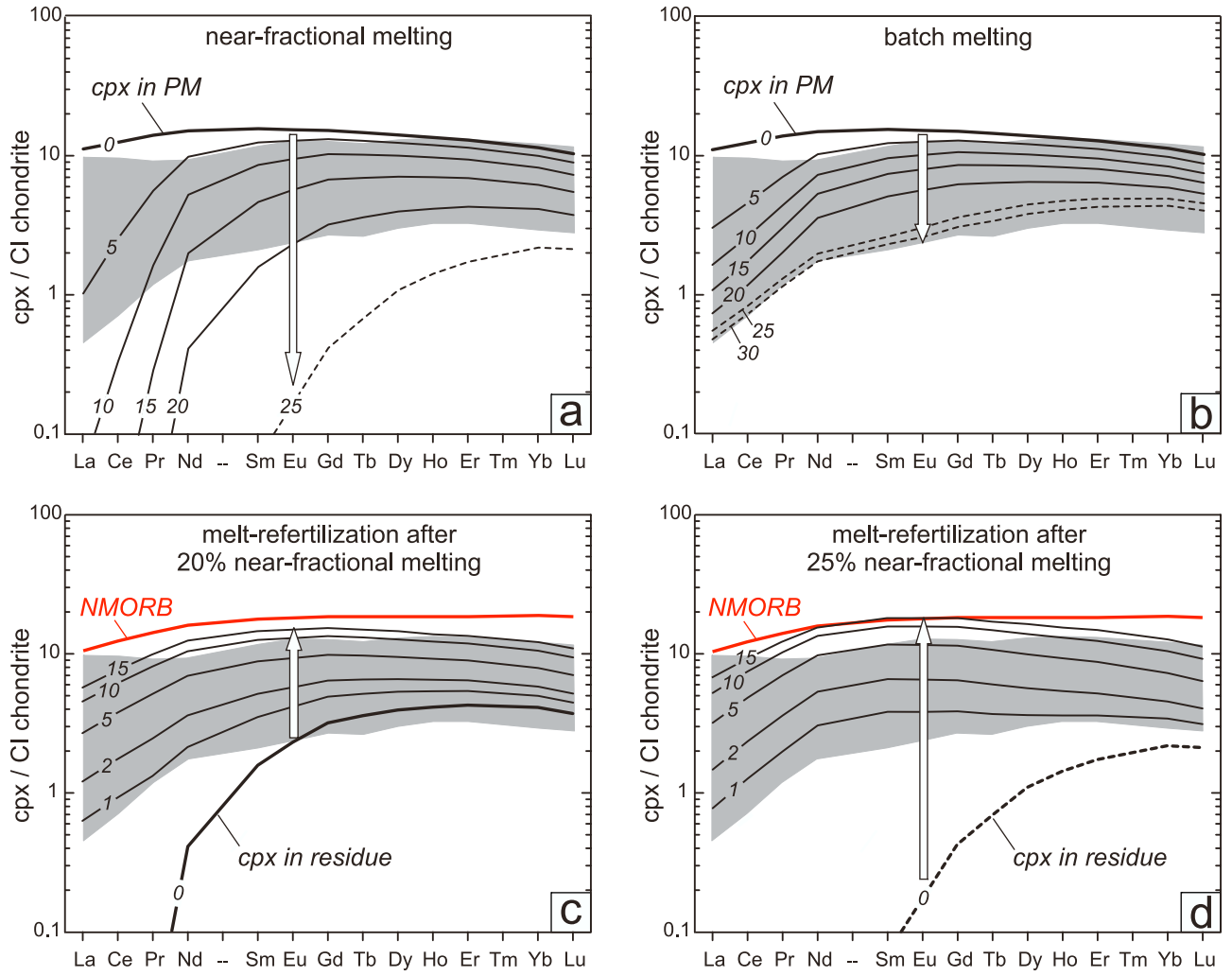

Figure 17. REE range of clinopyroxenes in high-ε_{Nd} peridotites from Dish Hill in comparison with REE concentrations in clinopyroxenes equilibrated in peridotite during adiabatic melting and refertilization, as modeled with Adiabat_1ph (starting conditions same as those in Figure 15): (a) near-fractional melting, (b) batch melting, (c) near-fractional melting residua corresponding to F(%) = 20, submitted to batch refertilization by a MORB-like component, and (d) same as Figure 17c but F(%) = 25. Grey field outlines the range of Dish Hill clinopyroxenes. Labeled lines are clinopyroxene patterns that correspond to various F(%) in Figures 17a and 17b and to various amounts of mafic component (wt %) added to residua in Figures 17c and 17d. All patterns were recalculated on the basis of mineral modes that correspond to subsolidus equilibrium at 1100°C, 1.5 GPa, as obtained with Adiabat_1ph. Dashed lines represent clinopyroxenes resulting exclusively from exsolution from residual orthopyroxene due to equilibration at the chosen subsolidus equilibrium conditions. The refertilizing component in Figures 17c and 17d is MORB end-member "L" of *Elthon* [1992] and has REE concentration as NMORB [*Sun and McDonough*, 1989]. Arrows show effects of melt removal and addition, respectively. See text for discussion.

allon slab, or if they are pieces of the slab itself, imbricated in response to the shearing between slab and overriding continental lithosphere.

[70] We do not favor the forearc or subarc lithosphere origin for the following reasons. Metasomatized forearc and subarc peridotites commonly display distinct enrichment in subducted slab-derived fluid-mobile elements (e.g., Cs, Rb, Ba, Sr, and Pb [cf. *Parkinson and Pearce*, 1998; *Bizimis et al.*, 2000; *Parkinson et al.*, 2003; *Lee*, 2005]), but the Dish Hill xenoliths show no hint of a subduction trace element signature. While depleted subarc harzburgites commonly contain spinel with extremely high Cr # ($\leq$0.8–0.85), no Dish Hill xenolith contains spinel with Cr # > 0.55. Sierra Nevadan ultramafic xenoliths, including garnet pyroxenites and peridotites, believed to represent the sub-Cordilleran batholitic root have conspicuous nonradiogenic Nd isotopic signatures [*Ducea and Saleeby*, 1998b]. However, we found no Dish Hill xenolith from beneath D1 that has negative ε_{Nd}. There is, of course, the possibility that the Dish Hill xenoliths once possessed subarc geochemical signatures, only to be obliterated later on by remelting or metasomatic processes occurring after subduction ended [*Lee*, 2005].

However, the distinct lithostratigraphic relations we report here argue against wholesale metasomatic overprinting.

[71] A much simpler hypothesis is that the underthrusted material represents the Farallon plate, as most of our geochemical and petrologic observations match what is seen and expected beneath mid-ocean ridges. First, the Nd isotopic compositions (positive ε_{Nd}) of the Dish Hill xenoliths resemble those observed in mid-ocean ridge basalts (MORBs) ($^{143}Nd/^{144}Nd = 0.5130$ [*Ito et al.*, 1987]). Second, the most depleted samples are consistent with the high degree of melting achieved by low-pressure melting beneath mid-ocean ridges. Third, major element compositions and mineral modes (Figures 7 and 8) largely match those observed in abyssal peridotites, the latter thought to represent residues of mid-ocean ridge basalts. These similarities with MORB mantle residues lead us to conclude that the high-ε_{Nd} xenoliths represent oceanic lithospheric mantle associated with the Farallon plate.

5.4. Evidence for Suboceanic Refertilization

[72] Although most whole-rock major element trends in the high-ε_{Nd} peridotites (the hypothesized fossil Farallon plate) can be explained by a simple partial melting scenario, a series of independent reasons suggest the compositions of these xenoliths might have been modified by subsequent refertilization.

[73] First, as pointed out above, in most samples there is textural evidence that clinopyroxene formed relatively late. Whereas in harzburgites this may be attributed to exsolution from orthopyroxene due to cooling, high clinopyroxene modes in lherzolites are obviously incompatible with such an interpretation, and thus require input of clinopyroxene components.

[74] Second, the continuous transition from the most fertile to the most depleted samples in the two arrays defined by the high-ε_{Nd} peridotites does not fit the predicted residual column associated with adiabatic decompression melting beneath a ridge. The observed compositional range occurs over less than 4 km, but the compositions themselves require a $\sim$40–60 km long melting column if the compositions are taken at face value to have been imparted purely by melt depletion. In addition, such a melting column would display an upward depleted trend, but the reverse is seen in the high-ε_{Nd} xenolith arrays. If these xenoliths represent simple melt residues from an adiabatic decompression column, a telescoping effect of >1000% extension and complete turnover is required, which seems unrealistic.

[75] Third, modeling of REE behavior during melting indicates that, while HREE concentrations in clinopyroxenes are consistent with reasonable degrees of adiabatic near-fractional melting of primitive mantle source, MREE and particularly LREE concentrations are systematically higher than predicted by fractional melting (Figure 17a). We note that a batch melting scenario could better reproduce the REE patterns of Dish Hill clinopyroxenes (Figure 17b), but would require the retention (and, then wholesale removal) of unrealistically high melt fractions, particularly in the case of harzburgites. Thus, the clinopyroxene REE patterns probably reflect instead various degrees of refertilization by addition of a LREE depleted component. As illustrated in Figures 17c and 17d, these clinopyroxenes can be best explained as deriving from fertile peridotites formed by mixing of 0.5 to 10–15 wt % of a basaltic liquid with NMORB trace element compositions [*Sun and McDonough*, 1989] into harzburgites that are the residua of earlier 20–25% adiabatic near-fractional melting of primitive mantle source. We note that adding LREE-enriched components akin to ocean island basalts and other low-degree melts cannot explain the observed REE patterns.

[76] Forth, whole-rock MgO-Na_2O covariation in high-ε_{Nd} peridotites from Dish Hill follows a linear trend that cannot directly result from low-pressure partial melting, because sodium is highly incompatible in such conditions, thereby yielding distinctly nonlinear trends when plotted against MgO or any other compatible element [e.g., *Langmuir et al.*, 1992; *Niu*, 1997; *Asimow*, 1999, and references therein] (Figure 18). Linear MgO versus Na_2O systematics have long been recognized in abyssal peridotites and explained either as a combination of adiabatic batch and fractional melting of fertile peridotites [*Asimow*, 1999], or as melt refertilization of depleted harzburgites [*Elthon*, 1992]. In the context of the latter, *Elthon* [1992] defined three primitive MORB end-members ("D," "L," and "H") with different major element compositions and argued that the addition of up to 10 wt % of low-Na_2O end-member "D" to depleted harzburgites can explain the linear MgO-Na_2O trends observed in abyssal peridotites. Likewise, we show in Figure 18 that the MgO-Na_2O trend defined by Dish Hill peridotites can be reproduced by mixing of harzburgitic residua resulting from 20 to 28% adiabatic near-fractional melting of primitive mantle source with up to 15–18 wt % end-member "L" [*Elthon*, 1992], which is about 3 times richer in Na_2O than end-member "D." Similar mixing may account for the MgO-Na_2O trend in abyssal peridotites from the East Romanche Fracture Zone described by *Seyler and Bonatti* [1997]. We note that low-degree melts are too rich in sodium and thus cannot account for the observed MgO-Na_2O trend.

[77] In summary, high-ε_{Nd} peridotites from Dish Hill consist of harzburgitic residues of high-degree melting and more fertile peridotites, the latter of which likely formed by the addition of a MORB-like component to the depleted harzburgites. Exactly when and how this refertilization occurred is difficult to answer. However, we note that there are no relict minerals of the depleted precursors, which suggests that enough time has passed to fully reequilibrate any textural or mineral-scale compositional heterogeneities associated with the refertilization event. One possibility is that refertilization was intimately associated with the melt extraction that formed the high-ε_{Nd} Dish Hill peridotites. If so, we suggest that the addition of MORB-like component might have occurred along a postadiabatic cooling path beneath a mid-ocean ridge (perhaps the ancestral northern extension of the East Pacific Rise), as the harzburgitic residua moved away from the spreading ridge axial zone. In this context, the peridotite composition trends seen in the high-ε_{Nd} samples may be a manifestation of refertilization, wherein the colder (shallower) parts of the lithospheric mantle were most affected by capture and freezing in of infiltrated melts. On the other hand, the inferred MORB-like liquid composition renders a sub-Mojave refertilization unlikely.

[78] A near-oceanic ridge refertilization origin would be ideally reflected by the isochronous alignment of the high-

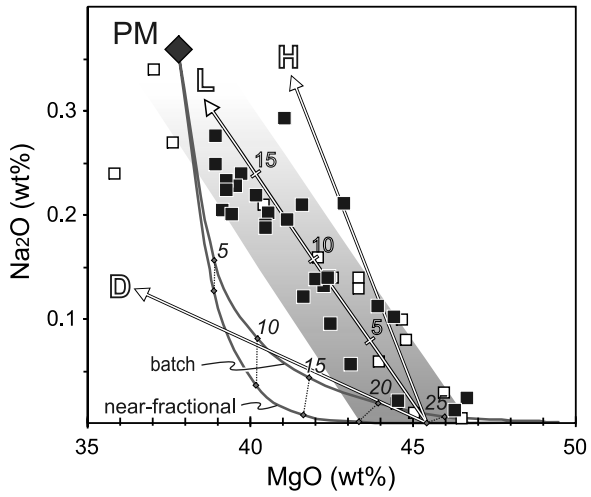

Figure 18. MgO-Na_2O covariation in high-ε_{Nd} peridotites from Dish Hill. Most xenoliths are too rich in Na_2O for given MgO to result from partial melting alone; however, their linear covariation is consistent with refertilization of depleted harzburgites with a MORB-like component. Adiabatic batch and near-fractional melting paths are derived with Adiabat_1ph (tick marks along melting paths indicate melting degrees, as labeled in italics; see text and Figure 15 for details). Arrows are mixing vectors defined by harzburgite resulting from 25% adiabatic near-fractional melting and MORB end-members "D," "L," and "H" of *Elthon* [1992]. Most Dish Hill peridotites (black squares) are reasonably well explained by the addition of up to 15–18 wt % component "L" to harzburgite residua resulting from 20–28% adiabatic near-fractional melting of primitive mantle source (gray field). Clinopyroxenes in abyssal peridotites from the East Romanche Fracture Zone (open squares) [*Seyler and Bonatti*, 1997] are shown for comparison.

ε_{Nd} peridotites in the Sm/Nd versus $^{143}Nd/^{144}Nd$ diagram (Figure 6). Whereas such an alignment can be distinguished for six of the high-ε_{Nd} xenoliths, this is clearly not the case for the whole high-ε_{Nd} group. The observed scattering can be attributed to MORB source Nd isotopic heterogeneity and/or late stage (postunderthrusting) contamination with mafic liquids of contrasting compositions similar to those observed by *Menzies et al.* [1985] and *Nielson et al.* [1993] (Figure 6).

[79] The evidence we see for refertilization is intriguing. If our interpretation that the high-ε_{Nd} Dish Hill xenoliths represent Farallon oceanic lithosphere is correct, the implication is that oceanic lithospheric mantle might be more heterogeneous than represented by the majority of abyssal peridotites, which are in general highly depleted. In this context, abyssal peridotites of the East Romanche Oceanic Fracture Zone are particularly interesting because, while they deviate from common abyssal mantle compositions, they resemble the Dish Hill peridotites in several respects. The East Romanche peridotites have high TiO_2 and Na_2O for given MgO, the suite contains fertile samples (i.e., low in MgO and high in Al_2O_3, CaO, and other incompatible components; Figure 7), and clinopyroxenes show only mild LREE depletion (Figure 2b). These features are inconsistent with a simple partial melting scenario and have been attributed to peridotite-melt reactions during late stage mantle upwelling beneath the Mid-Atlantic Ridge [*Seyler and Bonatti*, 1997]. We thus speculate that fertile compositions may be rather common in the oceanic lithospheric mantle, and not just accidental heterogeneities sampled in hot spot magmas.

5.5. Broader Implications

[80] New data reported here along with the results of previous studies yield an important update to our view on the structure and evolution of the Mojavian lithospheric mantle, and thus improve our understanding of the origin and evolution of the continental lithospheric mantle in southwestern United States. Re-Os ages of peridotites from Cima [*Lee et al.*, 2001] are consistent with Sm-Nd T_{DM} model ages of the oldest crustal rocks exposed across the Mojave Desert and surrounding areas [*Bennett and DePaolo*, 1987; *Wooden and Miller*, 1990; *Rämö and Calzia*, 1998], and may indicate Archean to Early Proterozoic crust-mantle differentiation in the region. Previous geochemical data [*Mukasa and Wilshire*, 1997] corroborated by results of this study show that the late Pliocene–early Pleistocene shallow (<40–50 km) lithospheric mantle beneath Cima is dominated by variably metasomatized peridotites displaying more or less pronounced incompatible trace element enrichments, as well as highly radiogenic Sr and Pb, and nonradiogenic Nd isotopic signatures. On the other hand, xenoliths erupted at Dish Hill reveal a geochemically layered lithospheric mantle of which shallower part (<40 km), akin to the sub-Cima mantle, appears to have nonradiogenic Nd isotopic signature and may represent a relic of the original Precambrian continental lithospheric mantle, whereas its deeper levels, located beneath the tectonic discontinuity D1, are depleted in incompatible trace elements, enriched in radiogenic Nd, and interpreted here to be of Farallon mantle lithosphere origin. In this view, the D1 discontinuity would coincide with *Kistler and Peterman*'s [1973] $Sr_i = 0.706$ isotopic boundary reinterpreted by *Miller et al.* [2000] as representing the western edge of the Precambrian North American mantle lithosphere. There are insufficient xenolith data to constrain the lateral extent of D1. Compositions and estimated entrainment depths of xenoliths from Cima indicate the absence of D1 at depths shallower than 40–50 km. D1 may traverse the lithospheric mantle beneath Cima deeper than the xenolith record, or, alternatively, it may dip relatively steeply to the NNE so that it intersects the lithosphere-asthenosphere boundary somewhere between the two xenolith localities. The duplex structure comprising upward enriched high-ε_{Nd} mantle slivers of oceanic origin might have formed during low-angle underthrusting of the Farallon plate along D1, or alternatively during the putative rollback phase during the demise of shallow flat subduction [i.e., *Saleeby*, 2003].

[81] Collectively, our observations are consistent with the view that the ancient North American continental lithospheric mantle, once underlying the central part of Mojave, underwent profound tectonic erosion by the shallowing of subduction of the Farallon plate during the onset of the Laramide orogeny [*Bird*, 1988]. The presence of low-ε_{Nd} mantle xenoliths at Dish Hill and Cima corroborate previous arguments that the ancient mantle was not entirely removed

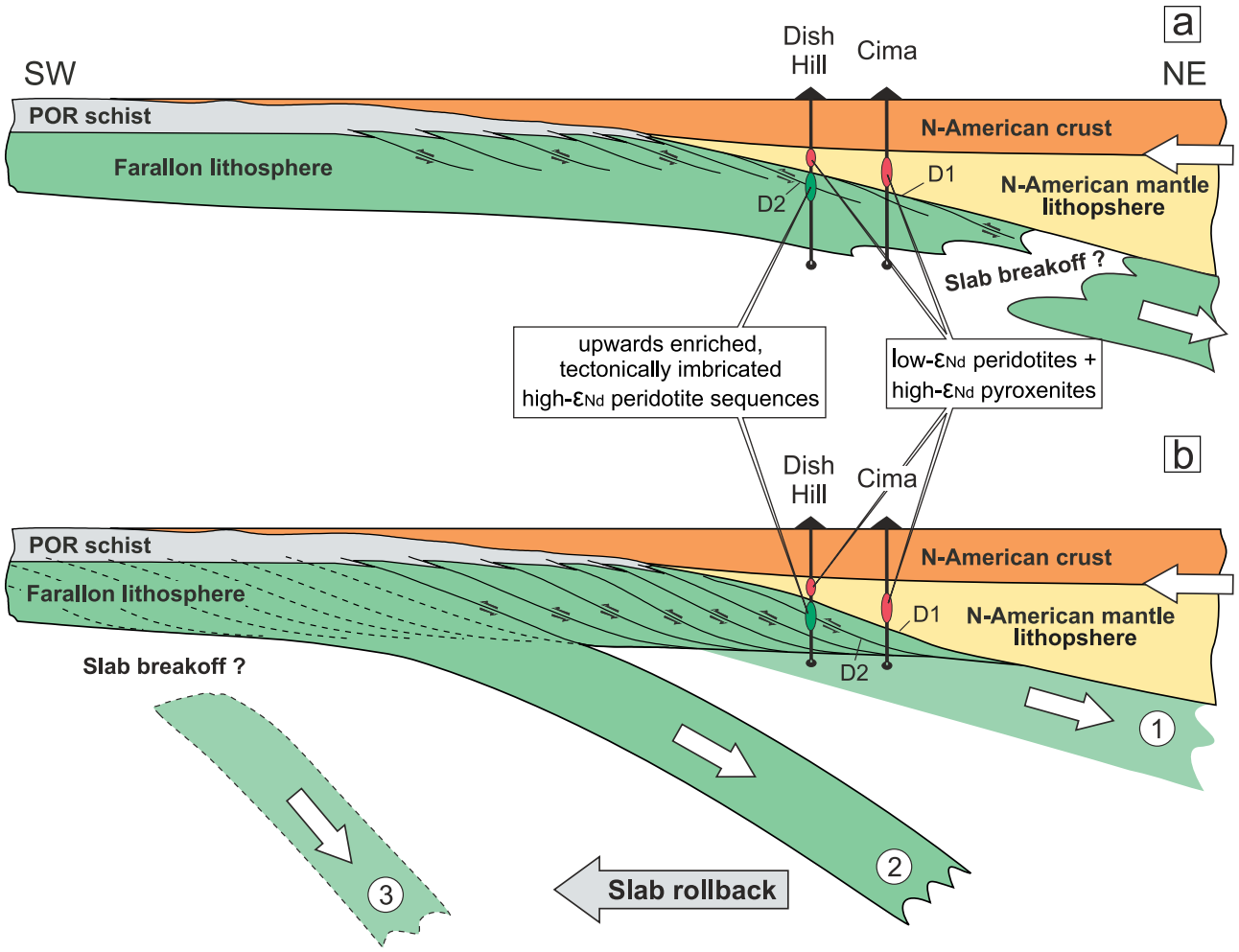

Figure 19. Rebuilding the Mojave lithosphere by underplating Farallon slab: diagram cross sections illustrating possible mechanisms of oceanic mantle addition to the thinned Mojave lithosphere during the early- to mid-Cenozoic Farallon subduction, as inferred from xenolith data from Dish Hill and Cima. (a) Large, coherent piece of Farallon slab stalling beneath the Mojave lithosphere. (b) Successive subcretion of Farallon slab fragments beneath the Mojave lithosphere. Stage 1 corresponds to the Laramide shallow subduction of Farallon slab. Stage 2 highlights slab rollback in progress, while mantle slivers are disrupted from the Farallon lithosphere and attached to the North American continent. The initiation of slab rollback might have begun in latest Cretaceous time on the basis of regional crustal extension having initiated in the Mojave region at this time [*Carl et al.*, 1991; *Applegate and Hodges*, 1995; *Wood and Saleeby*, 1998; *Wells et al.*, 2005]. Stage 3 illustrates final slab removal, possibly triggered by break off upon slab window initiated at ~28–30 Ma. D1 is the tectonic discontinuity separating low-ε_{Nd} and high-ε_{Nd} mantle domains; D2 delimits the medium- and high-temperature arrays of the high-ε_{Nd} domain. No scale is implied; in Figure 19b, subcreted mantle sliver thicknesses are exaggerated for visibility. POR, Pelona-Orocopia-Rand schist.

[*Livaccari and Perry*, 1993; *Ducea and Saleeby*, 1998b; *Miller et al.*, 2000]. Furthermore, the identification of underplated suboceanic peridotites beneath Dish Hill leads us to the hypothesis that subcreted nappes derived from the Farallon plate have significantly contributed to rebuilding the thinned continental lithosphere beneath the Mojave, and consolidated it to an extent that might have prevented widespread Neogene extension, a process that played a fundamental role in shaping the Basin and Range Province to the north and south of the Mojave Desert. One possible explanation for how Farallon mantle has been added to the Mojave lithosphere is that a large, coherent portion of the slab stalled beneath the region (Figure 19a). In this case, mantle duplexes similar to the one identified beneath Dish Hill may be representative for the top of slab that has been sheared in contact with the overlying continental lithosphere and previously underplated accretionary wedge material. Another possibility is that slivers detached from the slab's top were successively subcreted to the continental lithosphere as the slab retreated (Figure 19b). In this scenario, the high-ε_{Nd} peridotite suites identified beneath Dish Hill would be representative for individual slab fragments successively attached to the continent.

[82] If the high-ε_{Nd} xenoliths indeed represent the shallow Farallon mantle, then, ideally, MORB-like garnet granulite xenoliths representative of the overlying oceanic crust are expected to be found as well. The absence of such samples may have various causes. Sampling hiatus could be the one of these. In our model, the subducted MORB crust is predicted to lie along D1, that is, sandwiched between continental mantle in the top, and Farallon mantle in the bottom. However, as discussed in section 5.1, discontinuity D1 is marked by a ~5 km wide sampling gap. The fact that we found only three xenoliths shallower than D1 indicates that, for yet unclear reasons, Dish Hill basanites barely sampled the lithosphere above D1. Another cause could be that tectonic erosion accompanying the subduction ripped off the crustal section of the Farallon slab segment now underplating the central Mojave. It is indeed plausible that large pieces of oceanic crust remained sequestered beneath the western part of the Mojave, because metabasite blocks of MORB affinity are ubiquitous in the exhumed Pelona-Orocopia-Rand schists [*Jacobson et al.*, 1988] and seismic data [*Fuis et al.*, 2003; *Yan et al.*, 2005] suggest that their abundance in the schists increases with depth.

[83] Our interpretation is consistent with the low surface heat flow [*Lachenbruch et al.*, 1978, 1985; *Sass et al.*, 1994], as well as the anomalously high shear wave velocities of mantle [*Yang and Forsyth*, 2006] observed in the central and western part of the Mojave Desert.

[84] On the basis of the Mojavian lithosphere model emerging from our study, we further speculate that replacement of ancient lithospheric mantle by flat-subducted young oceanic peridotites at active continental margins may be an efficient mechanism of continent rejuvenation, which, in contrast with arcs, may lead to sharp crust-mantle isotopic contrasts, because it does not necessarily involve chemical modifications of the overlying crust.

[85] **Acknowledgments.** We kindly acknowledge assistance in xenolith field collecting from Lingsen Zeng and Zorka Saleeby. The manuscript greatly benefited from discussions with Paul Asimow, John Eiler, and Aniko Sandor. We are thankful for constructive reviews by Associate Editor Michael Bizimis, John Shervais, and an anonymous reviewer. Support was provided by the Gordon and Betty Moore Foundation to P. Luffi, by NSF grant EAR-0087347 to J. B. Saleeby, and by NSF EAR and EarthScope grants and the Packard Foundation to C.-T. A. Lee. This is contribution number 87 of Caltech Tectonics Observatory.

References

Agranier, A., and C. T. A. Lee (2007), Quantifying trace element disequilibria in mantle xenoliths and abyssal peridotites, *Earth Planet. Sci. Lett.*, *257*, 290–298, doi:10.1016/j.epsl.2007.02.041.

Alibert, C. (1994), Peridotite xenoliths from Western Grand-Canyon and the Thumb: A probe into the subcontinental mantle of the Colorado Plateau, *J. Geophys. Res.*, *99*, 21,605–21,620, doi:10.1029/94JB01555.

Applegate, J. D. R., and K. V. Hodges (1995), Mesozoic and Cenozoic extension recorded by metamorphic rocks in the Funeral-Mountains, California, *Geol. Soc. Am. Bull.*, *107*, 1063–1076, doi:10.1130/0016-7606(1995)107<1063:MACERB>2.3.CO;2.

Armstrong, J. (1988), Quantitative analysis of silicate and oxide minerals: Comparison of Monte Carlo, ZAF and φ ((z) procedures, in *Microbeam Analysis*, edited by D. Newbury, pp. 239–246, San Francisco Press, San Francisco, Calif.

Asimow, P. D. (1999), A model that reconciles major- and trace-element data from abyssal peridotites, *Earth Planet. Sci. Lett.*, *169*, 303–319, doi:10.1016/S0012-821X(99)00084-9.

Baker, M. B., and J. R. Beckett (1999), The origin of abyssal peridotites: A reinterpretation of constraints based on primary bulk compositions, *Earth Planet. Sci. Lett.*, *171*, 49–61, doi:10.1016/S0012-821X(99)00130-2.

Barbeau, D. L., M. N. Ducea, G. E. Gehrels, S. Kidder, and P. H. Wetmore (2005), U-Pb detrital-zircon geochronology of northern Salinian basement and cover rocks, *Geol. Soc. Am. Bull.*, *117*, 466–481, doi:10.1130/B25496.1.

Barth, A. P., and J. S. Schneiderman (1996), A comparison of structures in the Andean Orogen of northern Chile and exhumed midcrustal structures in Southern California, USA: An analogy in tectonic style?, *Int. Geol. Rev.*, *38*, 1075–1085.

Bennett, V. C., and D. J. DePaolo (1987), Proterozoic crustal history of the western United States as determined by neodymium isotopic mapping, *Geol. Soc. Am. Bull.*, *99*, 674–685, doi:10.1130/0016-7606(1987)99<674:PCHOTW>2.0.CO;2.

Bertrand, P., and J. C. C. Mercier (1985), The mutual solubility of coexisting ortho-pyroxene and clinopyroxene: Toward an absolute geothermometer for the natural system, *Earth Planet. Sci. Lett.*, *76*, 109–122, doi:10.1016/0012-821X(85)90152-9.

Bird, P. (1988), Formation of the Rocky Mountains, western United States: A continuum computer model, *Science*, *239*, 1501–1507, doi:10.1126/science.239.4847.1501.

Bizimis, M., V. J. M. Salters, and E. Bonatti (2000), Trace and REE content of clinopyroxenes from supra-subduction zone peridotites: Implications for melting and enrichment processes in island arcs, *Chem. Geol.*, *165*, 67–85, doi:10.1016/S0009-2541(99)00164-3.

Bodinier, J. L., and M. Godard (2003), Orogenic, ophiolitic, and abyssal peridotites, in *Treatise on Geochemistry, vol. 2, Geochemistry of the Mantle and Core*, edited by D. H. Heinrich and K. T. Karl, pp. 103–170, Elsevier, New York.

Bradshaw, T. K., C. J. Hawkesworth, and K. Gallagher (1993), Basaltic volcanism in the southern Basin and Range: No role for a mantle plume, *Earth Planet. Sci. Lett.*, *116*, 45–62, doi:10.1016/0012-821X(93)90044-A.

Brey, G. P., and T. Köhler (1990), Geothermobarometry in 4-phase lherzolites: 2. New thermobarometers, and practical assessment of existing thermobarometers, *J. Petrol.*, *31*, 1353–1378.

Burchfiel, B. C., D. S. Cowan, and G. A. Davis (1992), Tectonic overview of the Cordilleran Orogen in the western United States, in *The Cordilleran Orogen: Conterminous U.S.*, edited by B. C. Burchfiel et al., pp. 407–479, Geol. Soc. of Am., Boulder, Colo.

Canil, D. (2004), Mildly incompatible elements in peridotites and the origins of mantle lithosphere, *Lithos*, *77*, 375–393, doi:10.1016/j.lithos.2004.04.014.

Carl, B. S., C. F. Miller, and D. A. Foster (1991), Western Old Woman Mountains Shear Zone: Evidence for late ductile extension in the Cordilleran orogenic belt, *Geology*, *19*, 893–896, doi:10.1130/0091-7613(1991)019<0893:WOWMSZ>2.3.CO;2.

Cheadle, M. J., B. L. Czuchra, T. Byrne, C. J. Ando, J. E. Oliver, L. D. Brown, S. Kaufman, P. E. Malin, and R. A. Phinney (1986), The deep crustal structure of the Mojave Desert, California, from COCORP seismic-reflection data, *Tectonics*, *5*, 293–320, doi:10.1029/TC005i002p00293.

Clark, M. K., G. Maheo, J. B. Saleeby, and K. A. Farley (2005), The non-equilibrium landscape of the southern Sierra Nevada, California, *GSA Today*, *15*, 4–10, doi:10.1130/1052-5173(2005)015[4:TNLOTS]2.0.CO;2.

Das, T., and G. Nolet (1998), Crustal thickness map of the western United States by partitioned waveform inversion, *J. Geophys. Res.*, *103*, 30,021–30,038, doi:10.1029/98JB01119.

Davis, G. A., J. W. H. Monger, and B. C. Burchfiel (1978), Construction of the Cordilleran "collage" central British Columbia to central California, in *Mesozoic Paleogeography of the Western United States*, edited by D. G. Howell and K. A. McDougall, pp. 1–32, Pac. Sect. of the Soc. of Econ. Paleontol. and Mineral, Los Angeles, Calif.

Dickinson, W. R. (1997), Tectonic implications of Cenozoic volcanism in coastal California, *Geol. Soc. Am. Bull.*, *109*, 936–954, doi:10.1130/0016-7606(1997)109<0936:OTIOCV>2.3.CO;2.

Dickinson, W. R., and T. F. Lawton (2001), Tectonic setting and sandstone petrofacies of the Bisbee basin (USA-Mexico), *J. South Am. Earth Sci.*, *14*, 475–504, doi:10.1016/S0895-9811(01)00046-3.

Dickinson, W. R., and W. S. Snyder (1979), Geometry of subducted slabs related to San-Andreas transform, *J. Geol.*, *87*, 609–627.

Dimanov, A., and V. Sautter (2000), "Average" interdiffusion of (Fe, Mn)-Mg in natural diopside, *Eur. J. Mineral.*, *12*, 749–760.

Dokka, R. K. (1983), Displacements on late Cenozoic strike-slip faults of the Central Mojave Desert, *Calif. Geol.*, *11*, 305–308.

Ducea, M. N. (2001), The California Arc: Thick granitic batholiths, eclogitic residues, lithospheric-scale thrusting, and magmatic flare-ups, *GSA Today*, *11*, 4–10, doi:10.1130/1052-5173(2001)011<0004:TCATGB>2.0.CO;2.

Ducea, M. N., and J. B. Saleeby (1996), Buoyancy sources for a large, unrooted mountain range, the Sierra Nevada, California: Evidence from xenolith thermobarometry, *J. Geophys. Res.*, *101*, 8229–8244, doi:10.1029/95JB03452.

Ducea, M. N., and J. B. Saleeby (1998a), Crustal recycling beneath continental arcs: Silica-rich glass inclusions in ultramafic xenoliths from the Sierra Nevada, California, *Earth Planet. Sci. Lett.*, *156*, 101–116, doi:10.1016/S0012-821X(98)00021-1.

Ducea, M. N., and J. B. Saleeby (1998b), The age and origin of a thick mafic-ultramafic keel from beneath the Sierra Nevada batholith, *Contrib. Mineral. Petrol.*, *133*, 169–185, doi:10.1007/s004100050445.

Ducea, M. N., and J. B. Saleeby (1998c), A case for delamination of the deep batholithic crust beneath the Sierra Nevada, California, *Int. Geol. Rev.*, *40*, 78–93.

Ducea, M. N., J. Ganguly, E. J. Rosenberg, P. J. Patchett, W. J. Cheng, and C. Isachsen (2003), Sm-Nd dating of spatially controlled domains of garnet single crystals: A new method of high-temperature thermochronology, *Earth Planet. Sci. Lett.*, *213*, 31–42, doi:10.1016/S0012-821X(03)00298-X.

Ducea, M. N., J. B. Saleeby, J. Morrison, and V. A. Valencia (2005), Subducted carbonates, metasomatism of mantle wedges, and possible connections to diamond formation: An example from California, *Am. Mineral.*, *90*, 864–870, doi:10.2138/am.2005.1670.

Dumitru, T. A., P. B. Gans, D. A. Foster, and E. L. Miller (1991), Refrigeration of the western Cordilleran lithosphere during Laramide shallow-angle subduction, *Geology*, *19*, 1145–1148, doi:10.1130/0091-7613(1991)019<1145:ROTWCL>2.3.CO;2.

Ehrenberg, S. N. (1982), Petrogenesis of garnet lherzolite and megacrystalline nodules from the Thumb, Navajo Volcanic Field, *J. Petrol.*, *23*, 507–547.

Elthon, D. (1992), Chemical trends in abyssal peridotites: Refertilization of depleted suboceanic mantle, *J. Geophys. Res.*, *97*, 9015–9025, doi:10.1029/92JB00723.

Frey, F. A., and D. H. Green (1974), Mineralogy, geochemistry and origin of lherzolite inclusions in Victorian basanites, *Geochim. Cosmochim. Acta*, *38*, 1023–1059, doi:10.1016/0016-7037(74)90003-9.

Frey, F. A., and M. Prinz (1978), Ultramafic inclusions from San-Carlos, Arizona: Petrologic and geochemical data bearing on their petrogenesis, *Earth Planet. Sci. Lett.*, *38*, 129–176, doi:10.1016/0012-821X(78)90130-9.

Fuis, G. S., et al. (2003), Fault systems of the 1971 San Fernando and 1994 Northridge earthquakes, southern California: Relocated aftershocks and seismic images from LARSE II, *Geology*, *31*, 171–174, doi:10.1130/0091-7613(2003)031<0171:FSOTSF>2.0.CO;2.

Gabrielse, H., J. W. H. Monger, J. O. Wheeler, and C. J. Yorath (1992), Tectonic framework, morphogeological belts, tectonic assemblages and terranes, in *Geology of the Cordilleran Orogen in Canada*, edited by H. Gabrielse and C. J. Yorath, pp. 15–28, Geol. Soc. of Am., Boulder, Colo.

Galer, S. J. G., and R. K. O'Nions (1989), Chemical and isotopic studies of ultramafic inclusions from the San-Carlos Volcanic Field, Arizona: A bearing on their petrogenesis, *J. Petrol.*, *30*, 1033–1064.

Ganguly, J., and V. Tazzoli (1994), Fe^{2+}-Mg interdiffusion in orthopyroxene: Retrieval from the data on intracrystalline exchange reaction, *Am. Mineral.*, *79*, 930–937.

Gao, S., X. M. Liu, H. L. Yuan, B. Hattendorf, D. Gunther, L. Chen, and S. H. Hu (2002), Determination of forty two major and trace elements in USGS and NIST SRM glasses by laser ablation-inductively coupled plasma-mass spectrometry, *Geostand. Newsl.*, *26*, 181–196, doi:10.1111/j.1751-908X.2002.tb00886.x.

Ghiorso, M. S., M. M. Hirschmann, P. W. Reiners, and V. C. Kress (2002), The pMELTS: A revision of MELTS for improved calculation of phase relations and major element partitioning related to partial melting of the mantle to 3 GPa, *Geochem. Geophys. Geosyst.*, *3*(5), 1030, doi:10.1029/2001GC000217.

Green, D. H., and A. E. Ringwood (1970), Mineralogy of peridotitic compositions under mantle conditions, *Phys Earth Planet. Inter.*, *3*, 359–371, doi:10.1016/0031-9201(70)90076-2.

Griffin, W. L., D. Smith, C. G. Ryan, S. Y. O'Reilly, and T. T. Win (1996), Trace-element zoning in mantle minerals: Metasomatism and thermal events in the upper mantle, *Can. Mineral.*, *34*, 1179–1193.

Griffin, W. L., S. Y. O'Reilly, and C. G. Ryan (1999), The composition and origin of sub-continental lithospheric mantle, in *Mantle Petrology: Field Observations and High-Pressure Experimentation: A Tribute to Francis R. (Joe) Boyd*, edited by Y. Fei et al., *Spec. Publ. Geochem. Soc.*, *6*, 13–45.

Grove, M., C. E. Jacobson, A. P. Barth, and A. Vucic (2003), Temporal and spatial trends of Late Cretaceous-early Tertiary underplating Pelona and related schist beneath Southern California and southwestern Arizona, *Spec. Pap. Geol. Soc. Am.*, *374*, 381–406.

Hall, C. A., Jr. (1991), Geology of the Point Sur-Lopez Point region, Coast Ranges, California: A part of the Southern California Allochthon, *Spec. Pap. Geol. Soc. Am.*, *266*, 40 pp.

Hardebeck, J. L., and E. Hauksson (2001), Crustal stress field in southern California and its implications for fault mechanics, *J. Geophys. Res.*, *106*, 21,859–21,882, doi:10.1029/2001JB000292.

Hart, S. R., and A. Zindler (1986), In search of a bulk-earth composition, *Chem. Geol.*, *57*, 247–267.

Herzberg, C. (2004), Geodynamic information in peridotite petrology, *J. Petrol.*, *45*, 2507–2530, doi:10.1093/petrology/egh039.

Huffman, O. F. (1972), Lateral displacement of upper Miocene rocks and Neogene history of offset along San Andreas Fault in central California, *Geol. Soc. Am. Bull.*, *83*, 2913–2946, doi:10.1130/0016-7606(1972)83[2913:LDOUMR]2.0.CO;2.

Humphreys, E. D. (1995), Postlaramide removal of the Farallon slab, western United States, *Geology*, *23*, 987–990, doi:10.1130/0091-7613(1995)023<0987:PLROTF>2.3.CO;2.

Ionov, D. (2004), Chemical variations in peridotite xenoliths from Vitim, Siberia: Inferences for REE and Hf behaviour in the garnet-facies upper mantle, *J. Petrol.*, *45*, 343–367, doi:10.1093/petrology/egg090.

Ishikawa, A., S. Maruyama, and T. Komiya (2004), Layered lithospheric mantle beneath the Ontong Java Plateau: Implications from xenoliths in Alnoite, Malaita, Solomon Islands, *J. Petrol.*, *45*, 2011–2044, doi:10.1093/petrology/egh046.

Ito, E., W. M. White, and C. Gopel (1987), The O, Sr, Nd and Pb isotope geochemistry of MORB, *Chem. Geol.*, *62*, 157–176, doi:10.1016/0009-2541(87)90083-0.

Jacobson, C. E. (1995), Qualitative thermobarometry of inverted metamorphism in the Pelona and Rand Schists, southern California, using calciferous amphibole in mafic schist, *J. Metamorph. Geol.*, *13*, 79–92, doi:10.1111/j.1525-1314.1995.tb00206.x.

Jacobson, C. E., M. R. Dawson, and C. E. Postlethwaite (1988), Structure, metamorphism, and tectonic significance of the Pelona, Orocopia, and Rand schists, Southern California, in *Metamorphism and Crustal Evolution of the Western United States, Rubey Volume*, edited by W. G. Ernst, pp. 976–997, Prentice-Hall, Upper Saddle River, N. J.

Jagoutz, E., H. Palme, H. Baddenhausen, K. Blum, M. Cendales, G. Dreibus, B. Spettel, V. Lorenz, and H. Waenke (1979), The abundances of major, minor and trace elements in the Earth's mantle as derived from primitive ultramafic nodules, *Geochim. Cosmochim. Acta*, *Suppl. 11*, 2031–2050.

Johnson, D. M., P. R. Hooper, and R. M. Conrey (1999), XRF analysis of rocks and minerals for major and trace elements on a single low dilution Li-tetraborate fused bead, *Adv. X-Ray Anal.*, *41*, 843–867.

Johnson, K. E., A. M. Davis, and L. T. Bryndzia (1996), Contrasting styles of hydrous metasomatism in the upper mantle: An ion microprobe investigation, *Geochim. Cosmochim. Acta*, *60*, 1367–1385, doi:10.1016/0016-7037(96)00018-X.

Johnson, K. T. M., H. J. B. Dick, and N. Shimizu (1990), Melting in the oceanic upper mantle: An ion microprobe study of diopsides in abyssal peridotites, *J. Geophys. Res.*, *95*, 2661–2678, doi:10.1029/JB095iB03p02661.

Jones, C. H., and R. A. Phinney (1998), Seismic structure of the lithosphere from teleseismic converted arrivals observed at small arrays in the southern Sierra Nevada and vicinity, California, *J. Geophys. Res.*, *103*, 10,065–10,090, doi:10.1029/97JB03540.

Kidder, S., and M. N. Ducea (2006), High temperatures and inverted metamorphism in the schist of Sierra de Salinas, California, *Earth Planet. Sci. Lett.*, *241*, 422–437, doi:10.1016/j.epsl.2005.11.037.

Kil, Y., and R. F. Wendlandt (2007), Depleted and enriched mantle processes under the Rio Grande rift: Spinel peridotite xenoliths, *Contrib. Mineral. Petrol.*, *154*, 135–151, doi:10.1007/s00410-007-0183-y.

Kistler, R. W., and D. E. Champion (2001), Rb-Sr whole-rock and mineral ages, K-Ar, $^{40}Ar/^{39}Ar$, and U-Pb mineral ages, and strontium, lead, neodymium, and oxygen isotopic compositions for granitic rocks from the Salinian Composite Terrane, California, *U.S. Geol. Surv. Open File Rep., 01-0453*, 83 pp.

Kistler, R. W., and Z. E. Peterman (1973), Variations in Sr, Rb, K, Na, and Initial Sr^{87}-Sr^{86} in Mesozoic granitic rocks and intruded wall rocks in central California, *Geol. Soc. Am. Bull.*, *84*, 3489–3511, doi:10.1130/0016-7606(1973)84<3489:VISRKN>2.0.CO;2.

Kistler, R. W., and Z. E. Peterman (1978), Reconstruction of crustal blocks of California on the basis of initial strontium isotopic compositions of Mesozoic granitic rocks, *U.S. Geol. Surv. Prof. Pap., 1071*, 17 pp.

Klein, E. M., and C. H. Langmuir (1987), Global correlations of ocean ridge basalt chemistry with axial depth and crustal thickness, *J. Geophys. Res.*, *92*, 8089–8115, doi:10.1029/JB092iB08p08089.

Lachenbruch, A. H., J. H. Sass, and S. P. Galanis (1978), New heat-flow results from Southern-California, *Eos Trans. AGU*, *59*, 1051.

Lachenbruch, A. H., J. H. Sass, and S. P. Galanis (1985), Heat-flow in southernmost California and the origin of the Salton Trough, *J. Geophys. Res.*, *90*, 6709–6736, doi:10.1029/JB090iB08p06709.

Langmuir, C. H., E. M. Klein, and T. Plank (1992), Petrological systematics of mid-ocean ridge basalts: Constraints on melt generation beneath ocean ridges, in *Mantle Flow and Melt Generation at Mid-Ocean Ridges*, *Geo-*

phys. Monogr. Ser., vol. 71, edited by J. P. Morgan, D. K. Blackman, and J. M. Sinton, pp. 183–280, AGU, Washington, D.C.

Lee, C. T. A. (2005), Trace element evidence for hydrous metasomatism at the base of the North American lithosphere and possible association with Laramide low-angle subduction, *J. Geol.*, *113*, 673–685, doi:10.1086/449327.

Lee, C. T., Q. Z. Yin, R. L. Rudnick, and S. B. Jacobsen (2001), Preservation of ancient and fertile lithospheric mantle beneath the southwestern United States, *Nature*, *411*, 69–73, doi:10.1038/35075048.

Lee, C. T. A., A. D. Brandon, and M. Norman (2003), Vanadium in peridotites as a proxy for paleo-fO_2 during partial melting: Prospects, limitations, and implications, *Geochim. Cosmochim. Acta*, *67*, 3045–3064, doi:10.1016/S0016-7037(03)00268-0.

Lee, C. T. A., P. Luffi, T. Plank, H. Dalton, and W. P. Leeman (2009), Constraints on the depths and temperatures of basaltic magma generation on Earth and other terrestrial planets using new thermobarometers for mafic magmas, *Earth Planet. Sci. Lett.*, in press.

Le Roux, V., J. L. Bodinier, A. Tommasi, O. Alard, J. M. Dautria, A. Vauchez, and A. J. V. Riches (2007), The Lherz spinel lherzolite: Refertilized rather than pristine mantle, *Earth Planet. Sci. Lett.*, *259*, 599–612, doi:10.1016/j.epsl.2007.05.026.

Leventhal, J. A., M. R. Reid, A. Montana, and P. Holden (1995), Mesozoic invasion of crust by MORB-source asthenospheric magmas, US Cordilleran interior, *Geology*, *23*, 399–402, doi:10.1130/0091-7613(1995)023<0399:MIOCBM>2.3.CO;2.

Li, X. Q., X. H. Yuan, and R. Kind (2007), The lithosphere-asthenosphere boundary beneath the western United States, *Geophys. J. Int.*, *170*, 700–710, doi:10.1111/j.1365-246X.2007.03428.x.

Li, Y. G., T. L. Henyey, and L. T. Silver (1992), Aspects of the crustal structure of the western Mojave Desert, California, from seismic-reflection and gravity-data, *J. Geophys. Res.*, *97*, 8805–8816, doi:10.1029/91JB02119.

Livaccari, R. F., and F. V. Perry (1993), Isotopic evidence for preservation of Cordilleran lithospheric mantle during the Sevier-Laramide Orogeny, western United States, *Geology*, *21*, 719–722, doi:10.1130/0091-7613(1993)021<0719:IEFPOC>2.3.CO;2.

Ludington, S., et al. (2005), Preliminary integrated geologic map databases for the United States, western States: California, Nevada, Arizona, Washington, Oregon, Idaho, and Utah, version 1.2, *U.S. Geol. Surv. Open File Rep., 2005-1305*.

Maaløe, S., and K. I. Aoki (1977), Major element composition of upper mantle estimated from composition of lherzolites, *Contrib. Mineral. Petrol.*, *63*, 161–173, doi:10.1007/BF00398777.

Malin, P. E., E. D. Goodman, T. L. Henyey, Y. G. Li, D. A. Okaya, and J. B. Saleeby (1995), Significance of seismic reflections beneath a tilted exposure of deep continental crust, Tehachapi Mountains, California, *J. Geophys. Res.*, *100*, 2069–2087, doi:10.1029/94JB02127.

Martin, M. W., and J. D. Walker (1995), Stratigraphy and paleogeographic significance of metamorphic rocks in the Shadow Mountains, western Mojave Desert, California, *Geol. Soc. Am. Bull.*, *107*, 354–366, doi:10.1130/0016-7606(1995)107<0354:SAPSOM>2.3.CO;2.

McDonough, W. F. (1990), Constraints on the composition of the continental lithospheric mantle, *Earth Planet. Sci. Lett.*, *101*, 1–18, doi:10.1016/0012-821X(90)90119-I.

McDonough, W. F., and S. S. Sun (1995), The composition of the Earth, *Chem. Geol.*, *120*, 223–253, doi:10.1016/0009-2541(94)00140-4.

McKenzie, D., and M. J. Bickle (1988), The volume and composition of melt generated by extension of the lithosphere, *J. Petrol.*, *29*, 625–679.

Menzies, M., P. Kempton, and M. Dungan (1985), Interaction of continental lithosphere and asthenospheric melts below the Geronimo Volcanic Field, Arizona, USA, *J. Petrol.*, *26*, 663–693.

Miller, J. S., A. F. Glazner, and D. E. Crowe (1996), Muscovite-garnet granites in the Mojave Desert: Relation to crustal structure of the Cretaceous arc, *Geology*, *24*, 335–338, doi:10.1130/0091-7613(1996)024<0335:MGGITM>2.3.CO;2.

Miller, J. S., A. F. Glazner, G. L. Farmer, I. B. Suayah, and L. A. Keith (2000), A Sr, Nd, and Pb isotopic study of mantle domains and crustal structure from Miocene volcanic rocks in the Mojave Desert, California, *Geol. Soc. Am. Bull.*, *112*, 1264–1279, doi:10.1130/0016-7606(2000)112<1264:ASNAPI>2.3.CO;2.

Mukasa, S. B., and H. G. Wilshire (1997), Isotopic and trace element compositions of upper mantle and lower crustal xenoliths, Cima volcanic field, California: Implications for evolution of the subcontinental lithospheric mantle, *J. Geophys. Res.*, *102*, 20,133–20,148, doi:10.1029/97JB01518.

Nielson, J. E., J. R. Budahn, D. M. Unruh, and H. G. Wilshire (1993), Actualistic models of mantle metasomatism documented in a composite xenolith from Dish Hill, California, *Geochim. Cosmochim. Acta*, *57*, 105–121, doi:10.1016/0016-7037(93)90472-9.

Niu, Y. L. (1997), Mantle melting and melt extraction processes beneath ocean ridges: Evidence from abyssal peridotites, *J. Petrol.*, *38*, 1047–1074, doi:10.1093/petrology/38.8.1047.

Niu, Y. L., and R. Hékinian (1997), Basaltic liquids and harzburgitic residues in the Garrett Transform: A case study at fast-spreading ridges, *Earth Planet. Sci. Lett.*, *146*, 243–258, doi:10.1016/S0012-821X(96)00218-X.

O'Neill, H. S. C. (1981), The transition between spinel lherzolite and garnet lherzolite, and its use as a geobarometer, *Contrib. Mineral. Petrol.*, *77*, 185–194, doi:10.1007/BF00636522.

Palme, H. (2003), Cosmochemical estimates of mantle composition, in *Treatise on Geochemistry, vol. 2, Geochemistry of the Mantle and Core*, pp. 1–38, Elsevier, New York.

Parkinson, I. J., and J. A. Pearce (1998), Peridotites from the Izu-Bonin-Mariana forearc (ODP leg 125): Evidence for mantle melting and melt-mantle interaction in a supra-subduction zone setting, *J. Petrol.*, *39*, 1577–1618, doi:10.1093/petrology/39.9.1577.

Parkinson, I. J., R. J. Arculus, and S. M. Eggins (2003), Peridotite xenoliths from Grenada, Lesser Antilles Island Arc, *Contrib. Mineral. Petrol.*, *146*, 241–262, doi:10.1007/s00410-003-0500-z.

Pickett, D. A., and J. B. Saleeby (1993), Thermobarometric constraints on the depth of exposure and conditions of plutonism and metamorphism at deep levels of the Sierra-Nevada Batholith, Tehachapi Mountains, California, *J. Geophys. Res.*, *98*, 609–629, doi:10.1029/92JB01889.

Pike, J. E. N., and E. C. Schwarzman (1977), Classification of textures in ultramafic xenoliths, *J. Geol.*, *85*, 49–61.

Pollack, H. N., and D. S. Chapman (1977), Regional variation of heat-flow, geotherms, and lithospheric thickness, *Tectonophysics*, *38*, 279–296, doi:10.1016/0040-1951(77)90215-3.

Pouchou, J. L., and F. Pichoir (1984), A new model for quantitative X-Ray-microanalysis: 1. Application to the analysis of homogeneous samples, *Rech. Aerosp.*, *3*, 167–192.

Rämö, O. T., and J. P. Calzia (1998), Nd isotopic composition of cratonic rocks in the southern Death Valley region: Evidence for a substantial Archean source component in Mojavia, *Geology*, *26*, 891–894, doi:10.1130/0091-7613(1998)026<0891:NICOCR>2.3.CO;2.

Roy, R. F., D. D. Blackwell, and F. Birch (1968), Heat generation of plutonic rocks and continental heat flow provinces, *Earth Planet. Sci. Lett.*, *5*, 1–12, doi:10.1016/S0012-821X(68)80002-0.

Ruppert, S., M. M. Fliedner, and G. Zandt (1998), Thin crust and active upper mantle beneath the Southern Sierra Nevada in the western United States, *Tectonophysics*, *286*, 237–252, doi:10.1016/S0040-1951(97)00268-0.

Sachtleben, T., and H. A. Seck (1981), Chemical control of Al-solubility in ortho-pyroxene and its implications on pyroxene geothermometry, *Contrib. Mineral. Petrol.*, *78*, 157–165, doi:10.1007/BF00373777.

Saleeby, J. B. (1992), Petrotectonic and paleogeographic settings of U.S. Cordilleran ophiolites, in *The Cordilleran Orogen: Conterminous U.S.*, edited by B. C. Burchfiel et al., pp. 653–682, Geol. Soc. of Am., Boulder, Colo.

Saleeby, J. B. (2003), Segmentation of the Laramide Slab: Evidence from the southern Sierra Nevada region, *Geol. Soc. Am. Bull.*, *115*, 655–668, doi:10.1130/0016-7606(2003)115<0655:SOTLSF>2.0.CO;2.

Saleeby, J. B., and Z. Foster (2004), Topographic response to mantle lithosphere removal in the southern Sierra Nevada region, *Calif. Geol.*, *32*, 245–248.

Saleeby, J. B., M. N. Ducea, and D. Clemens-Knott (2003), Production and loss of high-density batholithic root, southern Sierra Nevada, California, *Tectonics*, *22*(6), 1064, doi:10.1029/2002TC001374.

Salters, V. J. M., and N. Shimizu (1988), World-wide occurrence of HFSE-depleted mantle, *Geochim. Cosmochim. Acta*, *52*, 2177–2182, doi:10.1016/0016-7037(88)90198-6.

Sass, J. H., A. H. Lachenbruch, R. J. Munroe, G. W. Greene, and T. H. Moses (1971), Heat flow in the western United States, *J. Geophys. Res.*, *76*, 6376–6413, doi:10.1029/JB076i026p06376.

Sass, J. H., A. H. Lachenbruch, S. P. Galanis, P. Morgan, S. S. Priest, T. H. Moses, and R. J. Munroe (1994), Thermal regime of the southern Basin and Range province: 1. Heat-flow data from Arizona and the Mojave Desert of California and Nevada, *J. Geophys. Res.*, *99*, 22,093–22,119, doi:10.1029/94JB01891.

Severinghaus, J., and T. Atwater (1990), Cenozoic geometry and thermal state of the subducting slabs beneath western North America, *Mem. Geol. Soc. Am.*, *176*, 1–22.

Seyler, M., and E. Bonatti (1997), Regional-scale melt-rock interaction in lherzolitic mantle in the Romanche Fracture Zone (Atlantic Ocean), *Earth Planet. Sci. Lett.*, *146*, 273–287, doi:10.1016/S0012-821X(96)00220-8.

Smith, D. (1979), Hydrous minerals and carbonates in peridotite inclusions from the Green Knobs and Buell Park kimberlitic diatremes on the Colorado Plateau, in *The Mantle Sample: Inclusions in Kimberlites and Other Volcanics (Proceedings of the Second International Kimberlite Confer-*

ence), edited by F. R. Boyd and H. O. A. Meyer, pp. 345–356, AGU, Washington, D.C.

Smith, D. (1999), Temperatures and pressures of mineral equilibration in peridotite xenoliths: Review, discussion, and implications, in *Mantle Petrology: Field Observations and High-Pressure Experimentation: A Tribute to Francis R. (Joe) Boyd*, edited by Y. Fei et al., *Spec. Publ. Geochem. Soc.*, *6*, 171–188.

Smith, D. (2000), Insights into the evolution of the uppermost continental mantle from xenolith localities on and near the Colorado Plateau and regional comparisons, *J. Geophys. Res.*, *105*, 16,769–16,781, doi:10.1029/2000JB900103.

Smith, D., and B. R. Barron (1991), Pyroxene-garnet equilibration during cooling in the mantle, *Am. Mineral.*, *76*, 1950–1963.

Smith, D., J. C. A. Riter, and S. A. Mertzman (1999), Water-rock interactions, orthopyroxene growth, and Si-enrichment in the mantle: Evidence in xenoliths from the Colorado Plateau, southwestern United States, *Earth Planet. Sci. Lett.*, *165*, 45–54, doi:10.1016/S0012-821X(98)00251-9.

Smith, P. M., and P. D. Asimow (2005), Adiabat_1ph: A new public front-end to the MELTS, pMELTS, and pHMELTS models, *Geochem. Geophys. Geosyst.*, *6*, Q02004, doi:10.1029/2004GC000816.

Spera, F. J. (1984), Carbon-dioxide in petrogenesis: 3. Role of volatiles in the ascent of alkaline magma with special reference to xenolith-bearing mafic lavas, *Contrib. Mineral. Petrol.*, *88*, 217–232, doi:10.1007/BF00380167.

Stock, G. M., R. S. Anderson, and R. C. Finkel (2004), Pace of landscape evolution in the Sierra Nevada, California, revealed by cosmogenic dating of cave sediments, *Geology*, *32*, 193–196, doi:10.1130/G20197.1.

Sun, S. S., and W. F. McDonough (1989), Chemical and isotopic systematics of oceanic basalts: Implications for mantle composition and processes, *Geol. Soc. Spec. Publ.*, *42*, 313–345.

Turcotte, D. L., and G. Schubert (2002), *Geodynamics*, 2nd ed., 456 pp., John Wiley, New York.

Turrin, B. D., J. C. Dohrenwend, S. G. Wells, and L. D. McFadden (1984), Geochronology and eruptive history of the Cima volcanic field, eastern Mojave Desert, California, *Surficial Geology of the Eastern Mojave Desert, California, Annu. Meet. Fieldtrip Guideb.*, vol. 14, edited by J. C. Dohrenwend, pp. 88–100, Geol. Soc. of Am., Boulder, Colo.

van Acken, D., H. Becker, and R. J. Walker (2008), Refertilization of Jurassic oceanic peridotites from the Tethys Ocean: Implications for the Re-Os systematics of the upper mantle, *Earth Planet. Sci. Lett.*, *268*, 171–181, doi:10.1016/j.epsl.2008.01.002.

Walker, J. D. (1988), Permian and Triassic rocks of the Mojave Desert and their implications for the timing and mechanisms of continental truncation, *Tectonics*, *7*, 685–709, doi:10.1029/TC007i003p00685.

Walter, M. J. (1999), Melting residues of fertile peridotite and the origin of cratonic lithosphere, in *Mantle Petrology: Field Observations and High-Pressure Experimentation: A Tribute to Francis R. (Joe) Boyd*, edited by Y. Fei et al., *Spec. Publ. Geochem. Soc.*, *6*, 225–239.

Walter, M. J. (2003), Melt extraction and compositional variability in mantle lithosphere, in *Treatise on Geochemistry, vol. 2, Geochemistry of the Mantle and Core*, edited by D. H. Heinrich and K. T. Karl, pp. 363–394, Elsevier, New York.

Wasserburg, G. J., S. B. Jacobsen, D. J. DePaolo, M. T. McCulloch, and T. Wen (1981), Precise determination of Sm/Nd ratios, Sm and Nd isotopic abundances in standard solutions, *Geochim. Cosmochim. Acta*, *45*, 2311–2323, doi:10.1016/0016-7037(81)90085-5.

Wells, M. L., M. A. Beyene, T. L. Spell, J. L. Kula, D. M. Miller, and K. A. Zanetti (2005), The Pinto shear zone: A Laramide synconvergent extensional shear zone in the Mojave Desert region of the Southwestern United States, *J. Struct. Geol.*, *27*, 1697–1720, doi:10.1016/j.jsg.2005.03.005.

Wells, P. R. A. (1977), Pyroxene thermometry in simple and complex systems, *Contrib. Mineral. Petrol.*, *62*, 129–139, doi:10.1007/BF00372872.

Wilshire, H. G., and S. B. Mukasa (1997), Mineral and whole rock major and trace element compositions of upper mantle and lower crustal xenoliths from the Cima volcanic field, California, *U.S. Geol. Surv. Open File, 97-173*.

Wilshire, H. G., and N. J. Trask (1971), Structural and textural relationships of amphibole and phlogopite in peridotite inclusions, Dish-Hill, California, *Am. Mineral.*, *56*, 240–255.

Wilshire, H. G., J. E. N. Pike, C. E. Meyer, and E. C. Schwarzman (1980), Amphibole-rich veins in lherzolite xenoliths, Dish Hill and Deadman Lake, California, *Am. J. Sci.*, *280*, 576–593.

Wilshire, H. G., C. E. Meyer, J. K. Nakata, L. C. Calk, J. W. Shervais, J. E. Nielson, and E. C. Schwarzman (1988), Mafic and ultramafic xenoliths from volcanic rocks of the Western United States, *U.S. Geol. Surv. Prof., 1443*.

Wilshire, H. G., A. V. McGuire, J. S. Noller, and B. D. Turrin (1991), Petrology of lower crustal and upper mantle xenoliths from the Cima Volcanic Field, California, *J. Petrol.*, *32*, 169–200.

Wilson, D. S., P. A. McCrory, and R. G. Stanley (2005), Implications of volcanism in coastal California for the Neogene deformation history of western North America, *Tectonics*, *24*, TC3008, doi:10.1029/2003TC001621.

Witt-Eickschen, G., and H. S. O'Neill (2005), The effect of temperature on the equilibrium distribution of trace elements between clinopyroxene, orthopyroxene, olivine and spinel in upper mantle peridotite, *Chem. Geol.*, *221*, 65–101, doi:10.1016/j.chemgeo.2005.04.005.

Witt-Eickschen, G., and H. A. Seck (1991), Solubility of Ca and Al in ortho-pyroxene from spinel peridotite: An improved version of an empirical geothermometer, *Contrib. Mineral. Petrol.*, *106*, 431–439, doi:10.1007/BF00321986.

Wood, B. J., and S. Banno (1973), Garnet-orthopyroxene and orthopyroxene-clinopyroxene relationships in simple and complex systems, *Contrib. Mineral. Petrol.*, *42*, 109–124, doi:10.1007/BF00371501.

Wood, D. J., and J. B. Saleeby (1998), Late Cretaceous-Paleocene extensional collapse and disaggregation of the southernmost Sierra Nevada Batholith, *Int. Geol. Rev.*, *39*, 973–1009.

Wooden, J. L., and D. M. Miller (1990), Chronological and isotopic framework for early Proterozoic crustal evolution in the eastern Mojave desert region, SE California, *J. Geophys. Res.*, *95*, 20,133–20,146, doi:10.1029/JB095iB12p20133.

Workman, R. K., and S. R. Hart (2005), Major and trace element composition of the depleted MORB mantle (DMM), *Earth Planet. Sci. Lett.*, *231*, 53–72, doi:10.1016/j.epsl.2004.12.005.

Yan, Z., and R. W. Clayton (2007), Regional mapping of the crustal structure in southern California from receiver functions, *J. Geophys. Res.*, *112*, B05311, doi:10.1029/2006JB004622.

Yan, Z. M., R. W. Clayton, and J. Saleeby (2005), Seismic refraction evidence for steep faults cutting highly attenuated continental basement in the central Transverse ranges, California, *Geophys. J. Int.*, *160*, 651–666, doi:10.1111/j.1365-246X.2005.02506.x.

Yang, Y., and D. W. Forsyth (2006), Rayleigh wave phase velocities, small-scale convection, and azimuthal anisotropy beneath southern California, *J. Geophys. Res.*, *111*, B07306, doi:10.1029/2005JB004180.

Zandt, G., H. Gilbert, T. J. Owens, M. N. Ducea, J. B. Saleeby, and C. H. Jones (2004), Active foundering of a continental arc root beneath the southern Sierra Nevada in California, *Nature*, *431*, 41–46, doi:10.1038/nature02847.

M. N. Ducea, Department of Geosciences, University of Arizona, Tucson, AZ 85721, USA.

C.-T. A. Lee and P. Luffi, Department of Earth Science, Rice University, 6100 Main Street, Houston, TX 77005, USA. (pluffi@rice.edu)

J. B. Saleeby, Division of Geological and Planetary Sciences, California Institute of Technology, Pasadena, CA 91125, USA.